Probing the Electronic Structure of New 3D Dirac Semimetals

Von der Fakultät Mathematik und Physik der Universität Stuttgart zur Erlangung der Würde eines Doktors der Naturwissenschaften (Dr. rer. nat.) genehmigte Abhandlung.

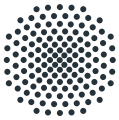

Universität Stuttgart

vorgelegt von

Andreas Topp

aus Stuttgart

Hauptberichter:	Dr. habil. Christian R. Ast
Mitberichter:	Prof. Dr. Jörg Wrachtrup
Mitberichterin:	Asst. Prof. Dr. Leslie M. Schoop
Prüfungsvorsitzende:	Prof. Dr. Maria Daghofer

Tag der mündlichen Prüfung: 11.04.2019

Universität Stuttgart &
Max-Planck Insitut für Festkörperforschung
2019

List of Publications

During the course of this Ph.D., the following publications arose:

[1] Leslie M Schoop, Mazhar N Ali, Carola Straßer, Andreas Topp, Andrei Varykhalov, Dmitry Marchenko, Viola Duppel, Stuart SP Parkin, Bettina V Lotsch, and Christian R Ast. Dirac cone protected by non-symmorphic symmetry and three-dimensional Dirac line node in ZrSiS. *Nature Communications*, 7:11696, 2016

[2] Andreas Topp, Judith M Lippmann, Andrei Varykhalov, Viola Duppel, Bettina V Lotsch, Christian R Ast, and Leslie M Schoop. Non-symmorphic band degeneracy at the Fermi level in ZrSiTe. *New Journal of Physics*, 18(12):125014, 2016

[3] Andreas Topp, Raquel Queiroz, Andreas Grüneis, Lukas Müchler, Andreas W Rost, Andrei Varykhalov, Dmitry Marchenko, Maxim Krivenkov, Fanny Rodolakis, Jessica L McChesney, et al. Surface floating 2D bands in layered nonsymmorphic semimetals: ZrSiS and related compounds. *Physical Review X*, 7(4):041073, 2017

[4] Andreas Topp, Maia G Vergniory, Maxim Krivenkov, Andrei Varykhalov, Fanny Rodolakis, Jessica L McChesney, Bettina V Lotsch, Christian R Ast, and Leslie M Schoop. The effect of spin-orbit coupling on nonsymmorphic square-net compounds. *Journal of Physics and Chemistry of Solids*, 2017

[5] Leslie M Schoop, Andreas Topp, Judith Lippmann, Fabio Orlandi, Lukas Müchler, Maia G Vergniory, Yan Sun, Andreas W Rost, Viola Duppel, Maxim Krivenkov, et al. Tunable Weyl and Dirac states in the nonsymmorphic compound CeSbTe. *Science Advances*, 4(2):eaar2317, 2018

[6] Leslie M Schoop and Andreas Topp. Topological Materials and Solid-State Chemistry - Finding and Characterizing New Topological Materials. In *Topological Matter*, pages 211–243. Springer, 2018

[7] Jessica Frick, Andreas Topp, Sebastian Klemenz, Maxim Krivenkov, Andrei Varykhalov, Christian R Ast, Andrew B Bocarsly, and Leslie M Schoop. Single Crystal Growth and Characterization of the Chalcopyrite Semiconductor $CuInTe_2$ for Photoelectrochemical Solar Fuel Production. *The Journal of Physical Chemistry Letters*, 2018

Abstract

The significance of angle-resolved photoemission spectroscopy (ARPES) as a tool for the characterization of the electronic properties of solids originates from its ability to reproduce the band structure directly, which gives access to properties like the quasiparticle masses and the Fermi velocity. It is furthermore a surface sensitive method, which got reinvigorated in recent years due to the discovery of topological surface states.

In this thesis, ARPES is used to measure the band structure of novel 3D Dirac semimetals, many of which were previously unknown concerning their electronic structure. The main results were obtained characterizing materials of space group (SG) no. 129 and more specifically ZrSiS and related compounds. These square-net materials crystallize in a nonsymmorphic space group, which enforces spin-orbit coupling (SOC) resistant degeneracies at high-symmetry points of the band structure. Resolving these, tuning them to the Fermi level and combining them with magnetic phases was investigated in ZrSiS, ZrSiTe and CeSbTe, respectively. $LaCuSb_2$ was then introduced as a material on the interface of topology and superconductivity, facilitating Majorana physics. The main findings of this thesis are however concerned with the surface electronic structure in the ZrSiS-family of compounds. We could show that the breaking of nonsymmorphic symmetry at the surface can lead to a new kind of surface state named 'floating surface state', which was previously unknown in the literature. Furthermore, we could reveal the nodal line character of these material, which can result in topological 'drumhead surface states' in the projected nodal line overlap in ZrSiTe.

Besides materials of SG 129, we focused on the first antiferromagnetic monolayer material with high mobility, $GdTe_3$. We did not only observe the charge density wave (CDW) formed below 385 K but could also resolve the Fermi surface pockets responsible for de Haas-van Alphen (dHvA) quantum oscillations measured in this material.

As a third project, we were able to use ARPES on the photocathode material $CuInTe_2$. The linearly dispersing bands and high Fermi velocities make this compound an interesting alternative in the field of photoelectrochemistry, although, a conclusive study on its electrochemical properties is still pending at this point.

PACS: 79.60.-i Photoemission and photoelectron spectra
71.20.-b Electron density of states and band structures of crystalline solids
73.20.-r Electron states at surfaces and interfaces
71.70.Ej Spin-orbit coupling
25.40.Dn Elastic neutron scattering

Auszug

Die Bedeutung von winkelaufgelöster Photoemission (ARPES) als Methode zur Charakterisierung der elektronischen Eigenschaften von Festkörpern liegt in ihrer Fähigkeit zur direkten Bestimmung der Bandstruktur, was es erlaubt Eigenschaften wie die Quasi-Teilchen-Masse und die Fermigeschwindigkeit zu erlangen. Da es sich um eine oberflächensensitive Messmethode handelt, wurde sie durch die Entdeckung von topologischen Oberflächenzuständen in den letzten Jahren wiederbelebt.

In dieser Arbeit wurde ARPES verwendet um die Bandstruktur von neuen, dreidimensionalen Dirac-Semimetallen zu untersuchen, von denen viele, in Bezug auf ihre elektronischen Eigenschaften, bisher unbekannt waren. Hauptsächlich wurden dabei Materialien der Raumgruppe (SG) Nr. 129, und spezieller der ZrSiS-Familie, charakterisiert. Diese Materialien besitzen nicht nur Atome, die in einem quadratischen Gitter angeordnet sind, sondern kristallisieren zudem in einer nicht-symmorphen Raumgruppe, die sich durch Bandentartungen an Hochsymmetrie-Punkten auszeichen, welche resistent gegen eine Spin-Bahn induzierte Bandlückenöffnung sind. Diese Entartungen zu charakterisieren, sie ans Fermi Level zu heben und ihre Interaktion mit magnetischen Phasen zu beobachten, wurde jeweils an den Materialien ZrSiS, ZrSiTe und CeSbTe untersucht. $LaCuSb_2$, ebenfalls in SG 129, befindet sich darüber hinaus zwischen den Feldern von Topologie und Supraleitung, was es sehr interessant im Rahmen von Majorana-Physik macht. Nichtsdestotrotz befassen sich die Hauptresultate dieser Arbeit mit den Oberflächenzustände der ZrSiS-Familie. Der Verlust der nichtsymmorphen Symmetrie an der Oberfläche führt in diesen Materialien zu bisher unbekannten Oberflächenzuständen, genannt 'floating surface states'. Außerdem zeigt ZrSiTe überdies topologische 'drumhead surface states', die durch die Knotenlinie in der Bandstruktur hervorgerufen werden und sich im Überlap ihrer Projektionen aufhalten.

Neben Materialien der SG 129 wurde in dieser Thesis auch $GdTe_3$ analysiert, das erste monomolekulare Schichtmaterial das neben antiferromagnetischen Eigenschaften auch eine hohe Mobilität aufweist. ARPES ermöglichte nicht nur die Beobachtung von Ladungsdichtewellen bei Temperaturen unter 385 K, sondern auch die Auflösung der Fermioberflächen-Taschen, die für die de Haas-van Alphen (dHvA) Quantenoszillationen verantwortlich sind.

Als drittes Projekt wurde $CuInTe_2$, ein Photokathodenmaterial, mit ARPES untersucht. Die linear dispergierenden Bänder und die hohen Fermigeschwindigkeiten machen dieses Material sehr interessant im Rahmen der Photoelektrochemie, wobei zu diesem Zeitpunkt noch keine umfassende Studie von dessen elektrochemischen Eigenschaften durchgeführt werden konnte.

Stichwörter: Winkelaufgelöste Photoemission
Elektronen-Zustandsdichte und Bandstrukturen von kristallinen Festkörpern
Elektronenzustände an Oberflächen und Grenzfächen
Spin-Bahn-Kopplung
Elastische Neutronenstreuung

Contents

Abstract (English / German) V

List of Figures XI

List of Tables XIII

1 Introduction 1

2 Theoretical Background 5
- 2.1 Electrons in three and two dimensional systems: From bulk to surface states . . . 5
  - 2.1.1 Density functional theory . . . 7
  - 2.1.2 Tight-binding . . . 10
  - 2.1.3 The effect of a surface - work function . . . 11
  - 2.1.4 Trivial surface states . . . 12
  - 2.1.5 Topological surface states . . . 14
- 2.2 The many features of space group 129 . . . 21
- 2.3 Crystal Growth . . . 24

3 Experimental Setup 25
- 3.1 The photoelectric effect . . . 25
- 3.2 Angle-resolved photoemission spectroscopy . . . 30
  - 3.2.1 Lab 7B15 . . . 34
  - 3.2.2 Synchrotron Bessy II . . . 35
  - 3.2.3 Synchrotron APS . . . 35
- 3.3 Neutron scattering . . . 35

4 ZrSiS - The First Nonsymmorphic Dirac Nodal Line Semimetal 37
- 4.1 Exemplary band structure of space group 129 . . . 38
- 4.2 3D vs 2D nature of bulk bands . . . 45
- 4.3 'Floating' surface states . . . 48
  - 4.3.1 Potassium evaporation . . . 49
  - 4.3.2 Tight-binding model and 'floating' surface state theory . . . 51
  - 4.3.3 Alternative explanations . . . 55

4.3.4 Conclusion 56

5 ZrSiTe - Tuning the Nonsymmorphic Point to the Fermi Level 57
5.1 Chemical strain effect on the electronic structure 58
5.2 Drumhead surface states 62

6 CeSbTe - Magnetic Order and Nonsymmorphic Symmetry 67
6.1 Magnetic order in space group 129 68
6.1.1 Antiferromagnetism and higher order crossings 75
6.1.2 'Ferromagnetism' and Weyl physics 76
6.2 The effect of spin-orbit coupling in space group 129 77

7 $LaCuSb_2$ - Space Group 129 and Superconductivity 81
7.1 Electronic structure determination 82
7.2 Topology and superconductivity 84

8 $GdTe_3$ - Towards Monolayer Antiferromagnetism 87
8.1 Nesting driven charge density wave 88
8.2 Monolayer antiferromagnet 91

9 $CuInTe_2$ - Towards Catalysis Applications 95
9.1 Surface Brillouin zone determination 96
9.2 The indications of a good photocathode in ARPES 97
9.3 Thermodynamical measurements 100

10 Conclusion & Outlook 103
10.1 The many faces of space group 129 103
10.2 $GdTe_3$ and its magnetic structure 104
10.3 $CuInTe_2$ applications in photoelectrochemistry 105

Bibliography 107

Acknowledgments 119

List of Figures

2.1 Schematic explanation for the origin of the work function 12
2.2 Schematic representation of the formation of Shockley surface states in a band inverted region 15
2.3 Helical spin polarization of TI surface states 19
2.4 Band crossings in Dirac, Weyl and nodal line semimetals 20
2.5 Common crystallographic and electronic features of the PbFCl structural family (SG 129) 23

3.1 Universal curve of the inelastic mean-free path 29
3.2 Illustration of the photoemission process in the ARPES setup and electron density 31
3.3 EDC on the example of ZrSiS for a photon energy of $\hbar\omega = 70\,\mathrm{eV}$ 32
3.4 The process of acquiring ARPES data on the example of ZrSiS at $\hbar\omega = 700\,\mathrm{eV}$ 34

4.1 Structural characterization of ZrSiS 39
4.2 DFT calculations of ZrSiS without and with SOC 40
4.3 ARPES measurements of ZrSiS 42
4.4 DFT slab calculations overlaid on ARPES measurements of ZrSiS 44
4.5 Photon energy dependent dispersion in ZrSiS 46
4.6 ARPES measurements and DFT slab calculations of the surface state in ZrSiS without and with K evaporation 50
4.7 Tight-binding model of the surface state in ZrSiS 53
4.8 DFT isosurfaces of ZrSiS at the nonsymmorphically protected X point . . . 54

5.1 Crystal structure characterization of ZrSiTe 58
5.2 Band structure of ZrSiTe 60
5.3 ARPES constant energy cuts of ZrSiTe 61
5.4 Nodal line comparison in ZrSiTe and ZrSiS 63
5.5 Dispersion of the drumhead surface state of ZrSiTe in DFT and ARPES . . 64
5.6 Surface projections of the drumhead surface states in ZrSiTe 65

6.1 Crystal structure of CeSbTe determined by neutron diffraction 69
6.2 Magnetic property measurements of CeSbTe 70
6.3 Refined neutron diffraction data of the two possible AFM phases in CeSbTe 71

6.4 Magnetic phase diagram of CeSbTe 72
6.5 Band structure of CeSbTe 73
6.6 Eight-fold degeneracy in the AFM phase of CeSbTe 75
6.7 DFT calculations for different magnetic phases of CeSbTe 76
6.8 Comparison of the effect of SOC on ZrSiS and CeSbTe 78

7.1 Crystal and electronic structure of $LaCuSb_2$ 83
7.2 SdH oscillation measurements of $LaCuSb_2$ 85

8.1 Structural characterization of $GdTe_3$ 89
8.2 Electronic structure characterization of $GdTe_3$ 90
8.3 2D scalability and carrier mobility of $GdTe_3$ 92

9.1 Unit cell determination of $CuInTe_2$ 97
9.2 ARPES measurements of $CuInTe_2$ 98
9.3 Thermodynamical measurements of $CuInTe_2$ 100

List of Tables

8.1 Fermi velocities of the bands around $\overline{\mathrm{X}}$ in $GdTe_3$ 91

CHAPTER 1

Introduction

The characterization of electronic properties in materials is of immense significance for the present day digital world. In its easiest implementation, it allows us to distinguish between metals, semiconductors and insulators, each having their own unique applications. Historically, one of the most prominent examples is the introduction of the semiconducting element silicon, which replaced germanium in the 1960s [8, 9], and is the basis for computer technology as it exists today. However, this classification only scratches the surface of ways in which the electronic characteristics of materials can be described. For example, not all crystalline solids have the same ballistic transport properties. They vary in their response to electric fields, which is determined by the mobility of their charge carriers, shown in the drift velocity under an applied voltage. The same is true for the charge carrier concentration, which can be vastly different resulting in a higher or lower conductance in the material. Also, the reciprocal value of the conductivity, the resistivity, can differ depending on lattice vibrations or simply lattice defects in the material; this leads to heat dissipation, a byproduct usually aimed to be minimized in electronics. Of course, not all of these quantities are independent. For instance, the earlier mentioned mobility is just the ratio between the effective mass of the charge carriers and the average time between scattering events. Therefore, while a single measurement method might only determine some of these properties, others can be concluded from the results and compared to complementary measurements.

Modifying the electronic properties in known components or finding new materials with better attributes has always been at the forefront of material research and development, since devices are continuously required to be faster and smaller than the previous generation. Sometimes, these material research experiments lead to the discovery of new phenomena in solid state science. For example, it was discovered that some materials, when kept at cold enough temperatures, can reach a state of vanishing resistivity, called superconductivity. More recently, a new class of topologically non-trivial

materials has been discovered that allows for the formation of conductive behavior at the surface of insulating bulk materials. Such new phenomena might not directly improve silicon-based electronics but enable new alternative approaches in the form of quantum computing [10, 11], spintronics [12] and twistronics [13].

One of the strongest tools available for the characterization of the electronic structure of materials is angle-resolved photoemission spectroscopy (ARPES). It not only allows for observing energy levels occupied by the electrons, but also their dispersion in reciprocal space. In combination, these observations result in the band structure, which enables the determination of quasi-particle effective masses, Fermi velocities and the evaluation of recombination processes. The biggest advantage of this technique is its strong surface sensitivity compared to transport measurements, which also measure electronic properties but are mostly bulk limited. Specifically, in the context of topological surface states, the simultaneous observation of bulk and surface states is beneficial, since it is direct proof of the bulk-boundary correspondence expected in these materials.

This thesis aims to determine the electronic properties of new 3D Dirac semimetals and focuses heavily, but not exclusively, on compounds of space group (SG) no. 129. 3D Dirac semimetals are materials containing four-fold degeneracies at specific points in the band structure. Around these Dirac points, cones of linearly dispersing bands are formed. Such materials show exotic physical properties, governed by their nearly massless quasi-particle excitations, which, for example, results in an unusual resistance response to an external magnetic field. Chapter 2 describes the theoretical background of such materials, starting from the general movement of electrons in a crystalline solid to motivate the principle of band structure in reciprocal space. The tools for simulating the band structure by means of density functional theory (DFT) and tight-binding calculations will be introduced, while distinguishing between bulk and surface contributions. Chapter 3 will then present the experimental techniques utilized in this thesis. The methods of ARPES and neutron scattering explained here were the main tools for collecting the data shown in the following chapters. Low energy electron diffraction (LEED) and X-ray photoemission spectroscopy (XPS) were regularly performed as preliminary measurements, but are not crucial for the presented results. Furthermore, all additional results shown in the following chapters that are not concerned with the experimental ARPES or neutron scattering data, like DFT, tight-binding calculations or structural determination measurements, were performed by collaborators. They show important information inaccessible by ARPES or neutron diffraction and are usually presented next to the experimental data. The accountable person can be found in the author contribution of the respective papers or the acknowledgments chapter of this thesis.

ZrSiS, the first material revealing the potential of SG 129, is presented in chapter 4. The square-net arrangement of atoms in this space group allows for the realization of

the aforementioned Dirac semimetallic nature in this material; even though the band crossing here is extended along a closed line, making ZrSiS and related compounds Dirac nodal line semimetals. This occurs in parallel with the nonsymmorphic symmetry elements present in this space group, which results in degenerate points in the band structure resistant against a gapping by spin-orbit coupling (SOC). Since these features could be combined in an earth-abundant, non-toxic and air/water-resistant material, ZrSiS has template character for the following chapters. One of the main findings of this thesis is further related to the surface band structure in this family of compounds, which was observed in ZrSiS for the first time. Due to the broken nonsymmorphic symmetry and hence the reduced symmetry at the surface, the bands are no longer forced to meet at the nonsymmorphically protected high-symmetry points. This results in 'floating surface states', a type of surface state, which has, to our knowledge, not been discussed in the literature so far. In many ways, this chapter, therefore, serves as a proof of principle concerning the inherent properties that can be realized in this space group.

Chapter 5 focuses on the influence of the nonsymmorphic symmetry on the band structure of ZrSiTe. This is accomplished by linking a structural parameter of the crystal structure with the position of the nonsymmorphically protected points and realizing that in ZrSiTe, this degeneracy is located at the Fermi level. Like ZrSiS, ZrSiTe shows a rich surface band structure, which can not entirely be related to the 'floating surface states' theory. Some of these surface states are rather due to the Dirac line nodes present in these materials. This chapter will, therefore, discuss the occurrence of topological 'drumhead surface states' in ZrSiTe and explain their absence in ZrSiS.

A third compound of similar structure type, CeSbTe, is discussed in chapter 6 and focuses on the influence, the introduction of atoms with magnetic moments has on the band structure. In this case, the lanthanide cerium is responsible for the magnetic order, which is combined them with the attributes of SG 129 in CeSbTe. Thereby, it undergoes several magnetic phase transitions, of which the antiferromagnetic order of the ground state was analyzed by means of neutron diffraction. For higher magnetic fields, this material reaches a fully polarized state with all magnetic moments ordered in parallel. ARPES measurements could only be performed on the paramagnetic phase, since the Néel temperature of $T_N = 2.7\,K$ is very low and stray magnetic fields make ARPES measurements impossible. However, the good agreement between ARPES and DFT in the paramagnetic phase gives credence to the theoretical calculations of the other magnetic phases, which reveal the potential for Weyl physics and crossings of higher order [14]. Lastly, the integration of heavier magnetic elements inadvertently increases the strength of SOC in CeSbTe. This effect on the surrounding band structure of the nonsymmorphically protected crossings will be discussed by comparing it with the lighter analog ZrSiS.

The structure type of ZrSiS is not the only configuration available in SG 129. By changing the structure type and retaining the symmetries of the space group, new properties can be introduced in the material, while keeping the square-net configuration responsible for the linear dispersions. Chapter 7 focuses on $LaCuSb_2$, a material reported to become superconducting for temperatures below $T_c = 0.9\,K$ [15, 16]. It shows the familiar diamond-shaped Fermi surface, proving the influence of the square-net motif on the electronic structure. The combination of superconductivity with the topological nature of this material makes $LaCuSb_2$ highly interesting in the context of Majorana physics.

There are, however, limitations to SG 129 that can not be overcome by replacing elements or changing the structure type. For example, the field of spintronics and twistronics requires 2D scalability of a material coupled with magnetic order [12, 13]. Chapter 8, therefore, focuses on the rare-earth tritelluride $GdTe_3$, a material crystallizing in SG 63, which nonetheless retains the square-net structure. While we were not the first ones analyzing this family of compounds, it was during a collaboration in this Ph.D. work that the potential of $GdTe_3$ as a monolayer antiferromagnet with high mobility was discovered. ARPES was used to confirm the occurrence of a charge density wave (CDW), gapping the pockets around the Fermi level except at one high-symmetry point. There, the size of these pockets could be related to quantum oscillations observed in this material.

Lastly, the electronic structure of a material is also of interest in the context of its photoelectrochemical properties. Usually, these attributes are not accessible by means of ARPES, since the band gaps of these materials are too high in order to efficiently harvest sunlight. Chapter 9 presents ARPES data on $CuInTe_2$, a material with its Fermi level located very close to the valence band maximum. This allows for the characterization of its band structure, since charging effects are not as pronounced as in other semiconducting materials. While being the only material discussed in this thesis, not featuring the square-net motif, it is still an excellent example for the potential ARPES has in the field of photoelectrocatalytic materials.

In conclusion, chapter 10 summarizes the obtained results during this Ph.D. work and illustrates possible directions for future research projects.

CHAPTER 2

Theoretical Background

The majority of results obtained in this thesis were collected by means of ARPES to map out the electronic bulk and surface structure of the analyzed single crystals. While a more in depth view on the experimental setup will be given in Chapter 3, it seems prudent to first give an overview over the interesting features of the used compounds and answer the question, why a surface sensitive technique like ARPES is a well suited tool for their investigation.

To this end, this chapter aims to introduce, in Section 2.1, the basic concepts of electrons in periodic crystal structures, focusing strongly on the emergent surface phenomena, where a reduced symmetry allows for additional solutions to the Schrödinger equation. In recent years, the concept of topology, furthermore, allowed for the prediction of topologically distinct surface states on the surface of e.g. topological insulators. The second part of this chapter focuses on the electronic properties of space group 129 in particular (Section 2.2). While not being the only space group analyzed during this Ph.D. work, space group 129 and its most prominent member ZrSiS, is responsible for some of the main findings of this thesis. Section 2.3 will then present a theoretical overview over the crystal growth techniques to realize the previously introduced symmetries in a sufficiently large single crystal for ARPES measurements.

2.1 Electrons in three and two dimensional systems: From bulk to surface states

To understand the features known as surface states that arise at the surface of crystals, one has to start by describing the behavior of electrons in a seemingly infinite crystal (namely the situation in the bulk of a single crystal).

The equation, describing the motion of an electron in a solid, is the time-independent Schrödinger equation

$$\hat{\mathcal{H}}\psi(\mathbf{r}) = E\psi(\mathbf{r})$$
$$\left[-\frac{\hbar^2}{2m}\nabla^2 + V(\mathbf{r})\right]\psi(\mathbf{r}) = E\psi(\mathbf{r}), \tag{2.1}$$

where $\hat{\mathcal{H}}$ is the Hamiltonian, with E being the energy, V the time-independent potential and ψ being the electronic wave function for an electron at the position described by the vector $\mathbf{r}$. For the sake of completeness, the wave functions and energies should have an additional index labeling the band index quantum number. We omit it here to not unnecessarily complicate the description and since our argumentation holds true for each value of the band index.

In a periodic and infinite 3D crystal structure, the potential energy is a periodic function:

$$V(\mathbf{r}) = V(\mathbf{r} + \mathbf{a}_\mathrm{n}), \tag{2.2}$$

with $\mathbf{a}_\mathrm{n} = n_1\mathbf{a}_1 + n_2\mathbf{a}_2 + n_3\mathbf{a}_3$ consisting of the primitive vectors of the lattice $\mathbf{a}_1$, $\mathbf{a}_2$ and $\mathbf{a}_3$ and n_1, n_2, $n_3 \in \mathbb{Z}$.

Bloch theorem Such a periodic potential allows for the separation of the periodic part $u_\mathbf{k}$ of the wave function according to Bloch's Theorem:

$$\psi(\mathbf{r}) = \psi_\mathbf{k}(\mathbf{r}) = u_\mathbf{k}(\mathbf{r})\mathrm{e}^{\mathbf{i}\mathbf{k}\cdot\mathbf{r}} \tag{2.3}$$
$$u_\mathbf{k}(\mathbf{r} + \mathbf{a}_\mathrm{n}) = u_\mathbf{k}(\mathbf{r}) \tag{2.4}$$

The proof of this theorem involves showing that the translation operator of the crystal structure commutes with the Hamiltonian and they therefore have common eigenfunctions. For a detailed description, follow Ref. [17], which this section roughly follows.

When multiplied by $\hbar$, the here introduced *wave vector*, $\mathbf{k}$, is equivalent to the crystal momentum of the electrons (which is not to be confused with the electron momentum, $\mathbf{p}$, of the free electron gas). In this context, the $\mathbf{k}$ vector is the quantum number of the translational symmetry of the lattice, analogous to the momentum $\mathbf{p}$, which is the quantum number of the translational symmetry of free space. ARPES experiments, as described in Sec. 3.2, almost directly map the crystal momentum of the electrons and allows us to contemplate the real space crystal structure in the geometric construction of k space (reciprocal space).

Reciprocal space The reciprocal lattice is geometrically constructed by the reciprocal basic vectors $\mathbf{b}_1$, $\mathbf{b}_2$ and $\mathbf{b}_3$ which satisfy:

$$\mathbf{b}_i \cdot \mathbf{a}_j = 2\pi\delta_{ij}, \quad i,j = 1,2,3 \tag{2.5}$$

and can therefore be constructed from the primitive unit cell vectors as:

$$\begin{aligned}
\mathbf{b}_1 &= 2\pi \frac{\mathbf{a}_2 \times \mathbf{a}_3}{\mathbf{a}_1 \cdot (\mathbf{a}_2 \times \mathbf{a}_3)} \\
\mathbf{b}_2 &= 2\pi \frac{\mathbf{a}_3 \times \mathbf{a}_1}{\mathbf{a}_2 \cdot (\mathbf{a}_3 \times \mathbf{a}_1)} \\
\mathbf{b}_3 &= 2\pi \frac{\mathbf{a}_1 \times \mathbf{a}_2}{\mathbf{a}_3 \cdot (\mathbf{a}_1 \times \mathbf{a}_2)}
\end{aligned} \tag{2.6}$$

This assumption of a real $\mathbf{k}$ vector that is furthermore limited to the lattice spanned by the reciprocal basic vectors is a direct consequence of the boundary conditions of the wave function chosen in Bloch's Theorem (the Born-von Karman periodic boundary condition). Note that the wave vector $\mathbf{k}$, and therefore $u_{\mathbf{k}}$, are not uniquely determined, since any addition of a reciprocal lattice vector (a linear combination of the reciprocal basis vectors) leaves the Hamiltonian unaffected. It is, therefore, in many cases possible to restrict $\mathbf{k}$ to one cell of the reciprocal lattice. The Wigner-Seitz construction of such a cell is called the first Brillouin zone (BZ) and it is the goal of many experimental and theoretical techniques to determine the energy dispersion $\mathrm{E}(\mathbf{k})$ there, since it contains all the necessary information about the movement of the electrons in the crystal.

To predict computationally this energy dispersion $\mathrm{E}(\mathbf{k})$ in the first BZ, namely the band structure, one has to apply some approximations to the Hamiltonian, which will lead to an iterative approach to calculate the states in solids.

2.1.1 Density functional theory

This section does not aim to give a complete picture of DFT and its refinement, but loosely follows Ref. [18] to which the interested reader is referred. DFT is a very important theoretical tool for the interpretation of ARPES measurements, not only because its *ab initio* calculations facilitate orientation in k space during a photoemission experiment, but more importantly, because a typical crystal is rarely perfect and phenomena like step edges and differently aligned multi-domains can produce additional bands that are not physical but merely a sign for a band beam spot (more in Sec. 3.2).

To derive the computationally accessible Kohn-Sham equation, one starts from the most general many body Hamiltonian of nuclei, sitting at the atomic sites, and N electrons filling the space between the cores. In an 'all electron' DFT calculation, this would

contain the nuclei and all electrons, but it is usually sufficient to perform pseudopotential DFT calculations with ionic cores and only the valence electrons in between, if the band structure around the Fermi level is of interest. The first approximation usually used in DFT is the Born-Oppenheimer approximation (adiabatic approximation) that considers the electronic and nuclear motions to be separable, since their different masses lead to changes on very different time scales. This allows us to write the Schrödinger equation for the electrons independently of the movement of the nuclei.

The Hamiltonian for the many-body problem of N electrons with spin $\sigma = \uparrow, \downarrow$ can then be written as:

$$\hat{\mathcal{H}}\psi_\alpha(\mathbf{r}_1\sigma_1,...,\mathbf{r}_N\sigma_N) = \left[\underbrace{-\frac{1}{2}\sum_{i=1}^{N}\nabla_i^2}_{T} + \underbrace{\sum_{i=1}^{N} v(\mathbf{r_i})}_{V_{\text{ext}}} + \underbrace{\frac{1}{2}\sum_i\sum_{j\neq i}\frac{1}{|\mathbf{r}_i-\mathbf{r}_j|}}_{V_{\text{ee}}}\right]\psi_\alpha = E_\alpha\psi_\alpha. \tag{2.7}$$

α is a complete set of many-electron quantum numbers. T is the kinetic energy of the electrons, followed by the interaction energy with an external field (e.g. the nuclei) V_{ext}. The last term, V_{ee}, is the electron-electron interaction energy. In a classical picture, if taken over all indices, this would be the classical Coulomb energy, while the sum over all $i = j$, which has to be subtracted to reproduce Eq. 2.7, is the self interaction energy. V_{ee} is also responsible for the fact that a product of atomic orbitals (e.g. a linear combination of Slater determinants) is no longer a solution of the Hamiltonian and instead correlated wave functions need to be found. Note that atomic units were chosen here with $\hbar = e^2 = m = 1$.

In density functional theory, the main way of computationally solving the band structure in this thesis, one expresses Eq. 2.7 dependent on the electron spin density $n_\sigma(\mathbf{r})$:

$$n_\sigma(\mathbf{r}) = N\sum_{\sigma_2...\sigma_N}\int \mathrm{d}^3r_2\cdots\int \mathrm{d}^3r_N\ \left|\psi(\mathbf{r}\sigma,\mathbf{r}_2\sigma_2,...,\mathbf{r}_N\sigma_N)\right|^2 \tag{2.8}$$

This definition of the electron spin density was chosen to ensure that N electrons with spin σ are found in the volume d^3r at $\mathbf{r}$:

$$\sum_\sigma\int \mathrm{d}^3r\, n_\sigma(\mathbf{r}) = N \tag{2.9}$$

A change away from the wave function to describe the physical system is not obvious. Hohenberg and Kohn [19] proved though that:
Theorem 1: The ground state energy is a unique functional of the electron density.
Theorem 2: The electron density that minimizes the energy of the overall functional is the true ground state electron density.

The expectation value of the Hamiltonian of Eq. 2.7 can then be expressed as:

$$E = T[n_\uparrow, n_\downarrow] + V[n] + U[n] + E_{\mathrm{xc}}[n_\uparrow, n_\downarrow] \tag{2.10}$$

with $T[n_\uparrow, n_\downarrow]$ being the expectation value for the kinetic energy and the functionals:

$$V[n] = \int \mathrm{d}^3 r\, n(\mathbf{r})\, v(\mathbf{r}) \tag{2.11}$$

$$U[n] = \frac{1}{2} \int \mathrm{d}^3 r \int \mathrm{d}^3 r'\, \frac{n(\mathbf{r})\, n(\mathbf{r}')}{|\mathbf{r} - \mathbf{r}'|} \tag{2.12}$$

$$n(\mathbf{r}) = n_\uparrow(\mathbf{r}) + n_\downarrow(\mathbf{r}) \tag{2.13}$$

The exchange-correlation energy functional $E_{\mathrm{xc}}[n_\uparrow, n_\downarrow]$ contains again, in analogy to the interaction energy, all terms that are not part of the first three. In practice, its correct form must be approximated and is done so in the form of local density approximation (LDA), generalized gradient approximation (GGA) or hybrid functionals, to name just a few.

In LDA, the exchange-correlation energy depends only on the density and the exchange-correlation energy per particle $e_{\mathrm{xc}}(n_\uparrow, n_\downarrow)$:

$$E_{\mathrm{xc}}^{\mathrm{LDA}}[n_\uparrow, n_\downarrow] = \int \mathrm{d}^3\; n(\mathbf{r}) e_{\mathrm{xc}}(n_\uparrow, n_\downarrow), \tag{2.14}$$

for which the exchange part E_{x} can even be written analytically in the picture of a homogeneous electron gas as:

$$E_{\mathrm{x}}^{\mathrm{LDA}}[n] = -\frac{3}{4}\left(\frac{3}{\pi}\right)^{1/3} \int \mathrm{d}^3 r\; n(\mathbf{r})^{4/3} \tag{2.15}$$

GGA is only slightly more complicated and depends not only on the density but also its derivative:

$$E_{\mathrm{xc}}^{\mathrm{GGA}}[n_\uparrow, n_\downarrow] = \int \mathrm{d}^3 r\; f(n_\uparrow, n_\downarrow, \nabla n_\uparrow, \nabla n_\downarrow) \tag{2.16}$$

Hybrid functionals finally solve the exchange part exactly, while building the rest of the exchange-correlation up from other sources, like LDA or GGA. In the order from LDA, GGA to hybrid functionals, they usually increase in accuracy, while getting more expensive in computational power.

To solve the presented system of Eq. 2.7 now, one can employ the density variational principle [19, 20, 21]. One starts with the Kohn-Sham system for non-interacting fermions and solves it for a given $n(\mathbf{r})$:

$$[T + V_{\mathrm{ext}}(\mathbf{r}) + V_{\mathrm{H}}(\mathbf{r}) + V_{\mathrm{xc}}(\mathbf{r})]\, \Phi_i(\mathbf{r}, \sigma) = \epsilon_{i,\sigma} \Phi_i(\mathbf{r}, \sigma) \tag{2.17}$$

This one-electron-approximation considers each individual electron to move in a potential given by the fixed nuclei $V_{\text{ext}}(\mathbf{r})$ and the average, constant field of all other electrons in the system $V_{\text{H}}(\mathbf{r})$, allowing us to obtain single-electron wave functions for $\Phi_i(\mathbf{r},\sigma)$ again. The DFT code used has influence on the basis functions available for the wave functions. For example, a sum of plane waves in a Fourier series could be a reasonable choice, since the electrons can move relatively free in between the periodic potential of the cores. Note that, since the involved functionals in Eq. 2.17 depend on $n(\mathbf{r})$, we guess its initial form in the beginning.

We can then recalculate the electron density and repeat the process until it converges and we, self-consistently, calculated the ground state.

2.1.2 Tight-binding

An alternative approach to get a theoretical idea about the band structure is to perform a tight-binding calculation. While DFT usually expresses the wave function in the basis of plane waves (at least for distances far enough away from the cores), tight-binding follows the opposite approach. A crystal lattice is build up by atoms, where the electrons are distributed around the core in linear combinations of atomic orbitals [22]. When the different atoms come close enough together, the electrons can at some point feel the influence of neighboring (or next-nearest neighboring and so on) atoms. For this reason, the tight-binding Hamiltonian is build up by putting atomic-like orbitals at the lattice sites, while allowing for a hopping of the electrons between them by means of 'hopping integrals'. The two center approximation does thereby allow only for an interference of up to two orbitals at a time, while three or more center terms are neglected.

In reality this Hamiltonian is build up by means of a look-up table (e.g. Ref. [23]). A minimal atomic orbital basis set for the different elements is chosen, depending on the valence band structure (lower orbitals are much more localized and therefore unlikely to deform from their atomic orbital starting point). These tables already do the necessary math that allows us to go from integrals over spherical harmonics to the relevant terms depending on the three $\mathbf{k}$ directions. The hopping matrix elements are then linear combinations of two different atomic orbitals (or of the same one, if there are bonds between the same atoms expected). This leads to σ, π or δ orbitals, depending on the bond angle geometry, that can be looked up as well. Their exact value is a fit parameter, but their dependence on the bond length can be modeled (e.g. Ref. [24]). Lastly, a pair potential needs to be chosen to describe the interaction, which adds more parameters. The fitting is then done by adjusting the parameters to the crystal structure, by comparing with DFT calculations or other empirical characteristics, like the band gap size.

One important thing to note here is the fact that the tight-binding model can be derived from DFT as a rigorous approximation [25, 26]. This is important in the context of a common criticism of tight-binding, namely its empirical way of finding and fitting parameters. Anthony T. Paxton expressed some advised thoughts to this topic (*NIC Series*, 42:157, 2009 [27]):

My own view is that if the tight binding approximation contains enough of the physics of the system we are studying then any reasonably chosen set of parameters will provide us with a useful model. From this point of view we would also demand that only a very small number of parameters is actually employed in the model. Furthermore it should be possible to choose these by intelligent guesswork and refinement starting from some well established set of rules.

– ANTHONY T. PAXTON

This reveals one of the big advantages the tight-binding model offers compared to DFT calculations, in its ability to catch the qualitative picture with relatively few parameters. Therefore, it allows one to find the responsible physical concept behind e.g. a certain band. If DFT tells one, that the measured band is real because it fits quantitatively, tight-binding tells one, where this band comes from and how it can be explained. Note, that this is of course not saying, that the opposite is necessarily true. DFT is very well able to explain the origin of bands by modifying the initial structure (be it to include defects, or introduce a periodic vacuum gap in the crystal structure to model the surface) and tight-binding calculations with more parameters can allow for quantitative agreement with experiments.

An example for the here shortly presented process will be given in Sec. 4.3, where we used a tight-binding model to describe the effect of a surface on the nonsymmorphic symmetries of the ZrSiS band structure.

2.1.3 The effect of a surface - work function

So far, we were mainly concerned with the electronic structure of the bulk crystal. As convenient as it might be for DFT calculations to consider only periodic boundary conditions, a real crystal is limited by its interface with the vacuum (and indeed this is where ARPES and other surface sensitive measurements collect most of the electronic properties). The atoms of any solid feel a different bonding environment at the surface than they do in the bulk, simply because some of their nearest neighbors are missing. The exact postition of atoms can therefore be slightly off from their Bravais lattice position, which can also lead to a surface reconstruction. Furthermore, the charge density

distribution does not have the same symmetry restrictions as in the bulk and this distortion can extend beyond the exact crystal boundary. This change in potential is decaying relatively fast on the order of some few lattice constants, but it is strong enough at the surface to introduce an electric field against which the electrons have to perform work [22]. Fig. 2.1 shows the charge density, as well as, the electronic energy along the surface normal direction. The work function Φ is the energy an electron needs at least to leave the crystal:

$$\Phi = \Phi_{\text{bulk}} + E_{\text{surface}} \tag{2.18}$$

It consists of the bulk work function $\Phi_{\text{bulk}} = E^{\infty}_{\text{vac}} - E_{\text{F}}$, defined as the difference in energy of a free electron and the energy of an electron at the Fermi level, and a surface contribution E_{surface}. The last part is due to the protruding charge carriers introducing a dipole moment at the surface.

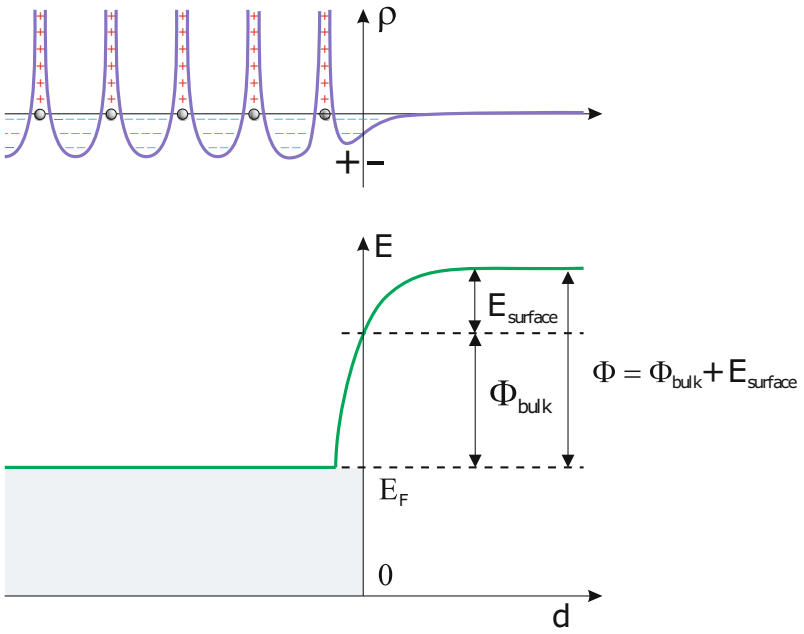

Figure 2.1: Charge density and electronic energy as a function of distance d from the 1D crystal surface. The energy needed for an electron to pass through the surface is determined by the difference between Fermi level of the bulk and the energy of a free electron and modified by the surface dipole layer. Adapted with permission from Ref. [28]. Copyright 2015, Springer-Verlag Berlin Heidelberg.

2.1.4 Trivial surface states

In the same way the charge density at the surface can vary from the bulk equilibrium, the surface potential will deviate from the perfectly periodic case introduced in Sec. 2.1. The bulk solutions of the Schrödinger equation are still Bloch waves, but they are exponentially dampened into the vacuum. Furthermore, additional solutions of

the Schrödinger equation in the form of surface states are allowed in this case, which decay exponentially into the vacuum as well as into the bulk. In solid state physics, one distinguishes these surface states depending on their origin and a short compilation will be given in the following. One thing they all have in common though, is their confined living environment in real space and consequential, a 2D electronic character without k_z dispersion.

The states presented in the following need to be distinguished from states due to surface resonances, which result from long-ranged image potentials at metal surfaces. These resonances do only decay exponentially into the bulk, but are far less localized in vacuum [29]. Furthermore, the most commonly found example for surface states, the Shockley type surface state, will not be discussed here, but below in the topological surface states paragraph.

Dangling bond surface states Electrons in semiconductors are much more localized in between the atoms than it is the case in metals. A surface can cut these connections by removing the out-of-plane atoms. The electrons belonging to the severed bonds of the surface layer atoms are called dangling bonds and are usually responsible for some kind of surface reconstruction to find a more favorable configuration. In the electronic structure of semiconductors, the energies associated with these dangling bond bands appear in the gap of the projected bulk bands as it is the case in Si(001) [30].

Surface states due to surface alloying When the first atomic surface layer of a metal is regularly alloyed by another element, the resulting order at the surface will result in additional states in addition to the bulk bands from lower layers. An example is the $(\sqrt{3} \times \sqrt{3})R30°$ Pb/Ag(111) alloy, where a third of a silver monolayer is replaced by lead and the resulting surface bands have mixed Pb-Ag character [31]. Should the alloy element be very heavy (e.g. Bi/Ag(111)), the increase in SOC can lead to a giant spin split of the observed bands [32].

Quantum well surface states Quantum wells are examples of quantum confinement, where electrons are confined in one direction by a potential well that only allows for discrete energy levels in between. To observe this effect, the de Broglie wave length of the charge carriers needs to be comparable to the quantum well thickness. In analogy, quantum well surface states can be observed on the surface of a solid, if up to a few monolayers of a different material is evaporated on top of the bulk. This confines the surface electrons in this 2D layer which gives rise to a varying amount of surface states depending on the thickness of the layer. Examples of this effect can be seen in up to 10 monolayers of Au on Pd(111), where states due to image potentials couple into Au and form quantum well states, before exponentially decaying into the Pd bulk [33].

Dimensional confinement can also be achieved by band bending on the surface, e.g. water vapor exposure on the surface of Bi_2Se_3. The resulting H_2Se gas produces positively charged vacancies, effectively binding the electrons more strongly in the surface layer, resulting in a band bending. Depending on the amount of water vapor, a varying amount of quantum well states can be observed that are further spin split due to the Rashba effect [34].

2.1.5 Topological surface states

So far, the considered surface states have in common that their appearance depends a lot on the details of the surface structure. In recent years, increased interest has been shown to a different kind of surface states. States on the surface of topologically non-trivial (or short 'topological') materials are predicted to appear, just by calculations that are purely concerned with the bulk properties. This is called the bulk-boundary correspondence, which states that at the interface of topological and trivial materials (trivial materials include vacuum), there need to be surface states just to satisfy the transition into a different Hilbert space topology.

The exact classification of an observed surface state can at times be difficult, and although there were helpful mathematical formalisms developed (presented below), some states have already been classified in the context of other surface state theories. That the difference can be very small can be seen in the context of Shockley states, where the influence of SOC can change the topology of a material drastically.

Shockley surface states In the context of tight-binding, when atoms are far apart, their level system is made up by s and p states and so on. If we consider main group elements for now, the s-states are usually the energetically lowest lying orbitals. When the interatomic space is reduced until interactions between them are allowed, the discrete states form bands. This behavior is schematically presented in Fig. 2.2. For a fixed lattice parameter a, a band consists of closely spaced orbitals that lie in a certain energy range with energy gaps between different bands. In Fig. 2.2 each band is represented by six energy levels, but in reality only two electrons with opposite spin can occupy one level (Pauli exclusion principle) and a macroscopic crystal contains a very large number of electrons, which makes the levels numerous and closely spaced in energy. If the s-band is always lower than the p-band for a certain interatomic spacing, than the gap is called 'direct', since it follows the energy behavior of the individual atoms. But if the interaction between different atoms becomes strong enough, hence the lattice parameter small enough, the gap can close and even open up again. Since in this latter case the s-band can be energetically higher than the p-band, we speak about an 'inverted' gap. It is in this region, the inverted band gap area, in which no bulk bands should be allowed, where Shockley surface states are found as an additional solution

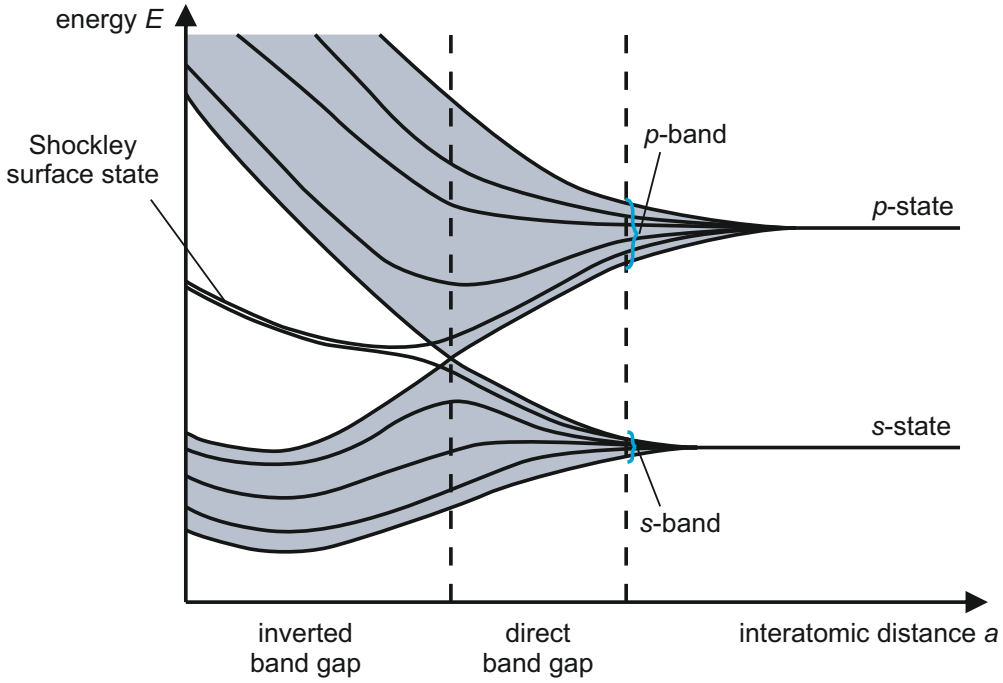

Figure 2.2: Evolution of the band energy range and gap region depending on the interatomic distance a. The projected bulk band structure is shown in grey. As soon as an inverted band gap is formed, Shockley surface states are available in the bulk band forbidden region as additional solutions to the tight-binding Hamiltonian.

to the Hamiltonian [35]. Outside of the inverted, projected bulk band gap, they merge with bulk bands again.

Note that Tamm surface states are very similar in nature but are derived in a different mathematical frame work [36]. Their existence is related to a perturbation of the surface potential and are more relevant when d-bands are considered. For practical reasons, Shockley states will be sufficient to considerate here.

One more interesting consequence of the consideration above is that not only a change in the interatomic distance can change the system from a direct into an inverted gap state. Other coupling effects can have a similar effect and therefore lead to the appearance of surface states. SOC is especially interesting in this context, since the original Shockley state does not consider SOC at all and is therefore spin degenerate. Should SOC reopen the band gap, two spin split surface states are expected that could be described as topologically derived surface states (in case of a non-trivial $\mathbb{Z}_2$-type invariant as it has been shown for gold [37]). This demonstrates the importance of reevaluation of surface states, since many of the historically earlier discovered surface states might actually be described in the frame work of topological surface states, on which Sec. 2.1.5 will hold forth about.

Topological insulators One of the first topological states were discovered in topological insulators (TIs), where the topology is a characteristic of the band gap and can, therefore, only change when the gap is somehow closed at the surface. Hence, TIs are materials that are insulating in the bulk, but show spin split surface states that bridge the gap at the surface in 3D and at the edge in 2D. These materials have become an interesting research topic, since in the absence of bulk bands in the gap, the spin polarized surface states prevent back-scattering and TIs are, therefore, very interesting, among other things, for spintronics and high carrier mobility transport measurements.

The following argumentation follows closely the derivation for the Berry phase given in Ref. [38]. First the Berry phase will be derived, followed by the definition of the $\mathbb{Z}_2$ invariant and how it can be derived from the time-reversal invariant momenta (TRIMs). Lastly, it is shown how the invariant is connected to the surface states observed in ARPES.

In principle, Berry phases always appear in a system with a Hamiltonian depending on an external parameter $\mathbf{R}$. Here, $\mathbf{R}(t)$ is a time-dependent parameter, which results in the following Schrödinger equation:

$$\hat{H}[\mathbf{R}(t)]\,|n,\mathbf{R}(t)\rangle = E_n[\mathbf{R}(t)]\,|n,\mathbf{R}(t)\rangle \tag{2.19}$$

The n-th eigenstate $|n,\mathbf{R}(t)\rangle$ as well as the energy $E_n[\mathbf{R}(t)]$ both then also depend on this external parameter. In the adiabatic evolution/approximation, we consider $\mathbf{R}$ to develop from $\mathbf{R}_0$ at $t = 0$ slow enough. The time evolution is then given by

$$\hat{H}[\mathbf{R}(t)]\,|n,t\rangle = \mathrm{i}\hbar\frac{\partial}{\partial t}\,|n,t\rangle, \tag{2.20}$$

with

$$|n,t\rangle = \exp\left(\frac{\mathrm{i}}{\hbar}\int_0^t \mathrm{d}t'\,L_n[\mathbf{R}(t')]\right)|n,\mathbf{R}(t)\rangle \tag{2.21}$$

$$L_n[\mathbf{R}(t)] = \mathrm{i}\hbar\dot{\mathbf{R}}(t)\cdot\langle n,\mathbf{R}(t)|\nabla_R|n,\mathbf{R}(t)\rangle - E_n[\mathbf{R}(t)] \tag{2.22}$$

Rewriting Eq. 2.21 reveals:

$$|n,t\rangle = \exp\left(-\int_0^t \mathrm{d}t'\,\dot{\mathbf{R}}(t')\cdot\langle n,\mathbf{R}(t')|\nabla_R|n,\mathbf{R}(t)\right)|n,t\rangle\;\cdot\;\exp\left(\frac{\mathrm{i}}{\hbar}\int_0^t \mathrm{d}t'\,E_n[\mathbf{R}(t')]\right) \tag{2.23}$$

The second exponent is the dynamic term, while the first one is directly related to the quantum mechanical phase accumulated. The Berry phase $\gamma_n[C]$ is defined on a closed loop C from $t = 0$ to $t = T$ (note that closed loop means equivalent points not necessarily the same one, since utilizing the periodicity of the BZ is a common tech-

nique):

$$\gamma_n[C] := \int_0^T \mathrm{d}t\, \dot{\mathbf{R}}(t) \cdot \mathrm{i}\langle n, \mathbf{R}(t)|\nabla_R|n, \mathbf{R}(t)\rangle \tag{2.24}$$

$$= \oint_C \mathrm{d}\mathbf{R} \cdot \mathrm{i}\langle n, \mathbf{R}|\nabla_R|n, \mathbf{R}\rangle \tag{2.25}$$

$$:= \oint_C \mathrm{d}\mathbf{R} \cdot \mathbf{A}_n(\mathbf{R}) \tag{2.26}$$

$$= -\int_S \mathrm{d}\mathbf{S} \cdot \mathbf{B}_n(\mathbf{R}) \tag{2.27}$$

Note that the Berry phase is only defined modulus 2π. The Berry connection $\mathbf{A}_n(\mathbf{R})$ of Eq. 2.26, in analogy to the vector potential in electromagnetic fields, corresponds to the gauge field freedom. To reach the Berry curvature $\mathbf{B}_n(\mathbf{R})$ of Eq. 2.27, Stokes' theorem was used with:

$$\mathbf{B}_n(\mathbf{R}) = \nabla_R \times \mathbf{A}_n(\mathbf{R}) \tag{2.28}$$

These are the mathematical tools from which general rules for the topological nature of a material can be derived. For example, in a 3D time-reversal symmetric systems, it is in practice helpful to calculate the four $\mathbb{Z}_2$ invariants to classify a material. To classify a material as a (weak) topological insulator, it is sufficient to consider the TRIMs Λ_i only, and a square BZ has eight of them, noting the middle of the BZ $\Lambda_{0,0,0}$ and spanning all corner points in the first quadrant (other quadrants are equivalent due to the symmetry of the system) $\Lambda_{\pi,0,0}$, $\Lambda_{0,\pi,0}$, $\Lambda_{0,0,\pi}$, $\Lambda_{\pi,0,\pi}$, $\Lambda_{0,\pi,\pi}$, $\Lambda_{\pi,\pi,0}$ and $\Lambda_{\pi,\pi,\pi}$. Calculation of a $\mathbb{Z}_2$ invariant happens in a plane spanning four TRIMs each, which would result in six different invariants. But even these six are not completely independent, since products of opposite sites are redundant. A system is therefore defined by four $\mathbb{Z}_2$ invariants only $\nu_0, \nu_1, \nu_2, \nu_3$:

$$w_{\alpha\beta}(\mathbf{k}) = \langle u_{\alpha,-\mathbf{k}}|\Theta|u_{\beta,\mathbf{k}}\rangle \tag{2.29}$$

$$\delta(\Lambda_i) := \frac{\mathrm{Pf}[w(\Lambda_i)]}{\sqrt{\det[w(\Lambda_i)]}} \overset{\mathrm{IS}}{=} \prod_{n=1}^{N} \xi_{2n}(\Lambda_i) \tag{2.30}$$

$$(-1)^{\nu_0} = \prod_{n_j=0,\pi} \delta(\Lambda_{n_1,n_2,n_3}) \tag{2.31}$$

$$(-1)^{\nu_i} = \prod_{\substack{n_{j\neq i}=0,\pi \\ n_i=\pi}} \delta(\Lambda_{n_1,n_2,n_3}), \quad (i = 1,2,3) \tag{2.32}$$

$|u_{n\mathbf{k}}\rangle$ are the eigenstates of the Bloch Hamiltonian in k space from Eq. 2.4. $w_{\alpha\beta}(\mathbf{k})$ is then the matrix representation of the time-reversal operator Θ. It is important to note that in the case of time-reversal and spacial inversion symmetry, Eq. 2.30 can be writ-

ten as a product of the parity eigenvalues ξ_{2n} of occupied levels at the TRIMs instead of having to calculate the Pfaffian and determinant of the w matrix [39]. Thereby, $\xi_\alpha(\Lambda_i) = \pm 1$ for band α and only the valence electrons need to be considered in this product, since filled shells always contribute in pairs with the same eigenvalues and square to +1. Typical DFT calculations of the band structure can directly calculate these parity eigenvalues and the only difficulty then comprises in counting the number of -1 eigenvalues, of each band crossing a TRIM, from the starting of the valence bands till the Fermi level.

The strong topological invariant ν_0 is obtained by considering all TRIMs, as shown in Eq. 2.31. Finally, the $\mathbb{Z}_2$ invariants ν_1, ν_2, ν_3 are constructed considering only the four TRIMs lying in one of the three planes that do not contain $\Lambda_{0,0,0}$, according to Eq. 2.32. TIs are classified by stating their four invariants (ν_0; ν_1 ν_2 ν_3), where ν_0 is describing the global character of the system and for $\nu_0 = 1$, a 3D TI is called 'strong' TI. The other three invariants ν_1, ν_2, ν_3 can be interpreted as Miller indices and denote the behavior in the three spacial directions. For $\nu_0 = 0$ and at least one of the $\nu_i = 1$ ($i = 1,2,3$), a TI is called 'weak' TI. Should all invariants be 0, the system is called (topologically) trivial. A strong TI will have surface states bridging the band gap on all surfaces, while a weak TI will only show them on the surfaces perpendicular to the normal (ν_1 ν_2 ν_3). The surface in direction of the normal is sometimes called 'dark'. If there are topologically protected surface states in the gap, however, the Fermi level must be cut by an odd number of them, which is a result of connectivity constructions between the TRIMs [39].

Finally, the topological protection that was mentioned at the beginning and that makes these surface states particularly interesting, will be discussed in more detail. The odd number of surface states crossing the Fermi level in TIs is enough to ensure that, regardless of the exact chemical potential, the surface states will never gap out or be influenced by non-magnetic perturbations [40]. This shows the strength of topological surface states, since they are resistant to the exact surface nature. Importantly in this context is the non-magnetic perturbation, since a breaking of time-reversal symmetry can very well change our previous arguments. Besides this resilient nature, the energy dispersion along the surface parallel momenta of topological surface states forms cones connecting the valence and conduction band. The schematic situation in 2D and 3D is depicted in Fig. 2.3(a) and (b), respectively. The crossing point is necessarily located at a TRIM and the dispersion in its close vicinity is of linear nature, giving rise to relativistic Dirac fermions as the surface state low energy excitation quasi-particles. A gapping of the cone to form parabolic dispersions is not allowed, without changing the topological nature of the material into a trivial insulator (topological protection against gap opening). Furthermore, the surface states show a helical spin polarization, meaning the spin structure is locked to the momentum $\mathbf{k}_\parallel$. Where usually impurities at the surface reduce the mobility because electrons are backscattered, reversing their momentum $\mathbf{k}_\parallel$, TI surface states are topologically protected against backscatter-

ing, since a change from $\mathbf{k}_\parallel$ to $-\mathbf{k}_\parallel$ is forbidden, because it would require an additional spin flip.

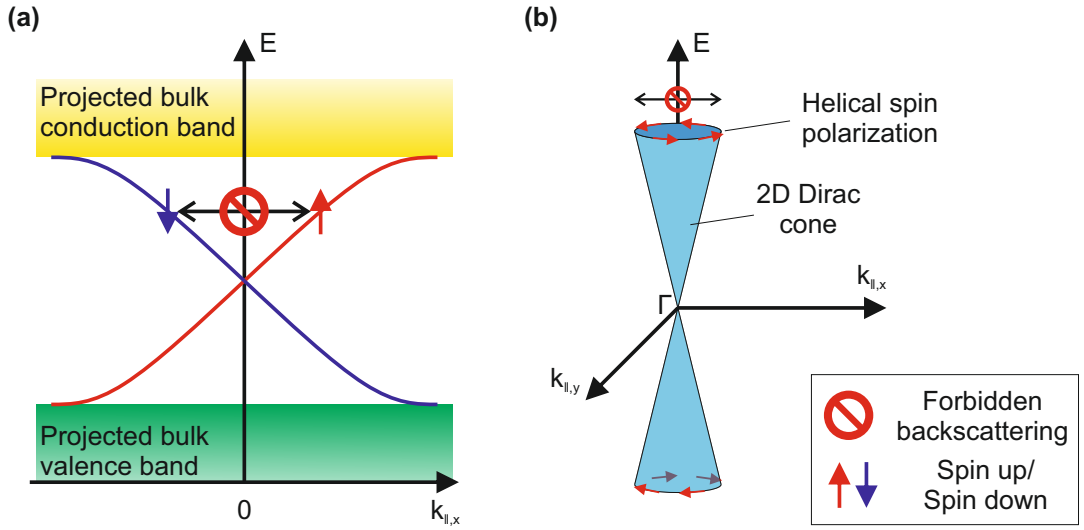

Figure 2.3: Helical spin polarization of TI surface states shown in (a) 2D and (b) 3D. The surface states form linearly dispersing bands crossing at the Dirac point at a TRIM. A gap opening as well as a backscattering from $\mathbf{k}_\parallel$ to $-\mathbf{k}_\parallel$ is forbidden, due to the topological protection and spin texture of the surface states.

Dirac and Weyl semimetals with Fermi arcs Another surface feature that is derived from the bulk topology are Fermi arcs arriving in Weyl semimetals. Again, we start with the bulk properties and derive the surface properties subsequently. Since this thesis is not mainly concerned with Weyl semimetals, the interested reader is referred to Ref. [41, 42].

Where TIs exhibit a global band gap in the projected bulk band structure and the surface states show Dirac physics, in Dirac and Weyl semimetals already the bulk valence and conduction band touch at specific points and the band structure forms 3D cones in k space around these points (3D since these features do not only exist at the surface, but the dispersion in all three k space directions is linear in energy). Fig. 2.4 shows the different possibilities for band touchings with linear dispersion. While all of these show physics analogous to relativistic Dirac physics, only a four-fold crossing of bands (two spin degenerate bands crossing) is called a Dirac crossing. Should it furthermore appear at an isolated point only, one speaks of a Dirac cone. In this context, graphene with its neglegible SOC and its six crossing points in the BZ is a 2D analog of a 3D Dirac semimetal. It is important to note here that such crossings need to be protected by crystal symmetries to not gap out. One of the requisite symmetries for spin degeneracy, which is necessary for Dirac crossings, is the combination of time-reversal and spacial inversion symmetry. Therefore, in the presence of SOC, the crystal symmetry needs to exhibit a C_3, C_4 or C_6 rotation axis to preserve the crossing [43]. Note

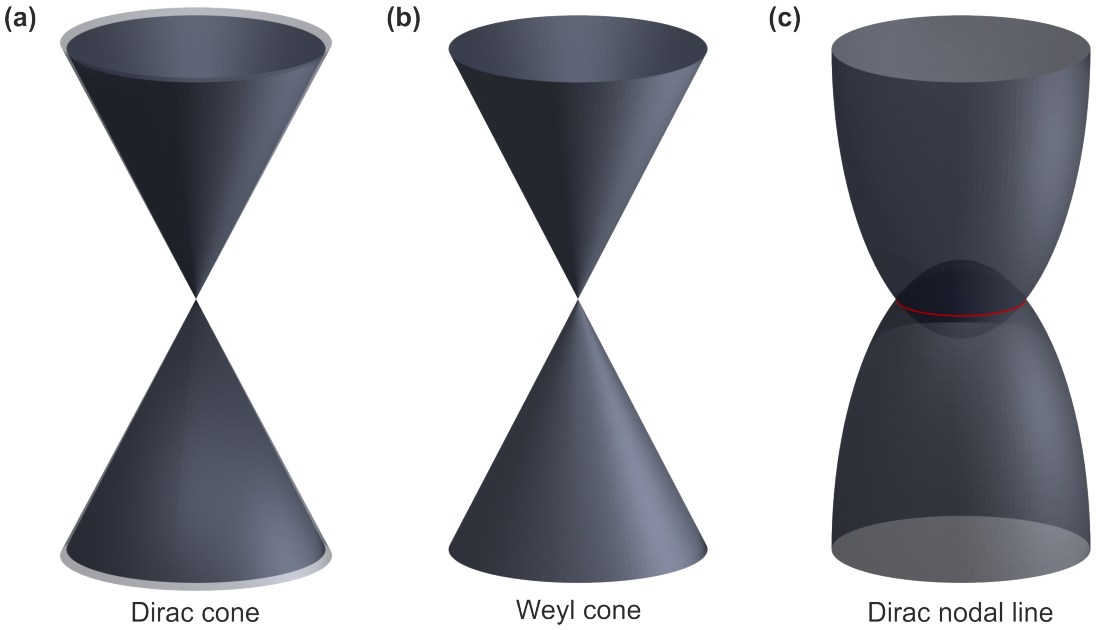

Figure 2.4: Band crossings in (a) Dirac, (b) Weyl and (c) nodal line semimetals. The nodal line is show in red. The degenerate point is four-fold at the Dirac point and line node and two-fold at the Weyl point. Weyl points always occur in pairs, of which only one is shown here.

that Dirac semimetals are not necessarily topologically non-trivial nor result in surface states.

Should one of the time-reversal or spacial inversion symmetries be broken in a material, either because it is non-centrosymmetric or exhibits a magnetic field, all the bands are spin split and the crossings become two-fold. In this case, one speaks of Weyl semimetals. These Weyl nodes are of topological nature and can be seen as (anti-)-monopole charges of the Berry curvature [44]. They have to come in pairs of opposite chirality but are usually hard to localize in the band structure. Since they have so little symmetry requirements, they can be off the high-symmetry points or lines. It is therefore sometimes easier to measure their topological surface states, called 'Fermi arcs', instead. Fermi arcs run in the surface BZ and unlike surface states considered so far, they have defined starting and end points in k space. They always connect the surface projection of two Weyl points with opposite chirality. This also shows the stability of Weyl cones, since they are topologically intertwined with each other, they can not gap out individually, but instead need to combine with another Weyl cone first, forming Dirac cones again.

Nodal lines and drumhead surface states As seen above, already Dirac cones can only exist if certain symmetries prevent the cone from gapping when considering SOC. Should the bands not only touch at a point but instead overlap, the intersection could extend the crossings along a whole line in k space, called a line node. To extend the

degeneracy of accidental band crossings along a complete nodal line, further symmetries need to be incorporated, which makes them a feature of materials crystallizing in highly symmetric space groups or incorporate only very light elements to make SOC negligible.

Typically a mirror or glide symmetry is able to support nodal lines, if the valence and conduction band have different mirror/glide eigenvalues. Much more interesting for this thesis is however the case, where a π Berry phase shift is stabilizing the nodal line. In these systems, any closed loop to determine the Berry phase, according to Eq. 2.26, will give a phase of π, while all loops not containing the nodal line will give 0. The nodal line is in this case topologically stabilized, since there is no continuous deformation of the nodal line that would nullify its Berry phase, without opening the gap. This local evaluation of the Berry phase is of course much more involved than the global evaluation of a material, e.g. in the form of the $\mathbb{Z}_2$ invariant. It is nevertheless important, since systems with topologically protected nodal lines show characteristic surface states, called 'drumhead surface states', which will become important for Sec. 5.2.

Drumhead surface states exist only inside of the surface projection of the nodal line, where the Berry phase is π. Like a 2D drumhead, these surface states span the encircled band gap area and have been theoretically predicted in a number of compounds [45, 46, 47].

2.2 The many features of space group 129

All of the topics of the aforementioned sections have been realized, or at least theoretically predicted, in various compounds. It is the possibility to realize all the trivial to exotic physical phenomena in one family of compounds that makes the presented concepts here so interesting. Since the main part of the experimental findings of this thesis in the Chapters 4, 5, 6 and 7 is dedicated to these effects, this section aims to give a basic understanding of the properties of SG 129 ($P4/nmm$). This will allow us to understand the common features of all these compounds and how each of the chapters focuses on one or two of these properties. The reader is advised to keep in mind that, while this section discusses the properties of a square-net material in SG 129, this argumentation is actually limited to a certain structure type, namely the PbFCl structural family here.

The following paragraph follows closely the argumentation given in Ref. [48], which is heavily inspired by the work of Ref. [49]. As an easy example, ZrSiS is a material crystallizing in SG 129, although the following argumentation can be extended to isostructural and even some non-isostructural compounds as well. The crystal structure of ZrSiS is

shown in Fig. 2.5(a) and (b). The main building block is the Si square net that sandwiches the rocksalt-type layers of Zr and S. Since SG 129 is a nonsymmorphic space group, between the two sulfur layers, there exists a glide plane that combines a mirror operation in z with a translation of half a unit cell in $x+y$ direction, to coincide the top and bottom part of the unit cell. The exact symmetry operations will be discussed in detail in Chap. 4 since it is important for the tight-binding calculations of the surface state origin. For now, we consider only chemically intuitive arguments to develop the general band structure.

Since ZrSiS is a layered material, we will neglect the k_z dispersion for now and focus on the square net exclusively. If we consider only s and p orbitals (as expected for Si) in a square-net arrangement of atoms, we can evaluate their phases for the high-symmetry points of the tetragonal BZ. As can be seen in Fig. 2.5(c), the phases are all aligned at Γ, which is only a favorable bonding constellation for the s and p_z orbitals leading to a band minimum for the bands formed from these orbitals. Since s bands, with their σ bonds, are energetically lower lying than the π bonding in p bands, we can construct a starting position for the bands at Γ, with arbitrary energies $E_s < E_{p_z} < E_{p_x} = E_{p_y}$. The bands will continuously evolve from there towards the high-symmetry point X. The phases of the orbitals are switched along k_x at this point, which results in a slightly less favorable setting for s and p_z since they only remain in phase along k_y. p_x and p_y behave completely opposite here, since the X point represents the band minimum for p_x, while it is the energetically most unfavorable position for the p_y band. The M point finally switches phases along k_x as well as k_y, which leads to a band degeneracy for p_x and p_y again that is preserved along the complete high-symmetry line M-Γ. s and p_z bands have their band maximum at the M point. The complete schematic picture of the square-net band structure is given in Fig. 2.5(d).

From this 2D starting point, we can consider the effect of the nonsymmorphic glide plane. As the small schematic in Fig. 2.5(b) shows, the so far considered square-net unit cell is doubled in size and rotated by 45 ° because of the translational part of the glide symmetry. Or in other words, the Zr and S square nets are less dense and require a, twice as big, unit cell when extending our model to the 3D crystal structure. Such a doubling of the unit cell leads to a back-folding of the BZ in k space, which is depicted in Fig. 2.5(d). The derived band structure is folded along the perpendicular bisector of the Γ-M line, resulting in a superposition of Γ and M. The 45 ° rotation makes this overlay the new Γ-X line. The same holds true for the square-net X-M line, which will be folded and become the new Γ-M high-symmetry line in the nonsymmorphic BZ.

This results in some features all materials in this structure type have in common. All bands are forced to be degenerate at the X and M point and this degeneracy is even extended along the X-M line if we do not consider SOC, as we did in this derivation. In the following this behavior is called 'nonsymmorphical protection', since without the non-

symmorphic symmetry this crossing would be lifted (more on this topic in Sec. 4.3). Furthermore, should the exact energetic position of the p_z band allow for a crossing with the p_x and p_y bands (as implicitly assumed above), a Dirac line node exists in the BZ. The line node energy will vary throughout the BZ, but it is a direct consequence of the square net, since it already exists without the nonsymmorphic symmetry considerations. Should the Fermi level be located within this energy window, the material can be classified as a Dirac line node semimetal.

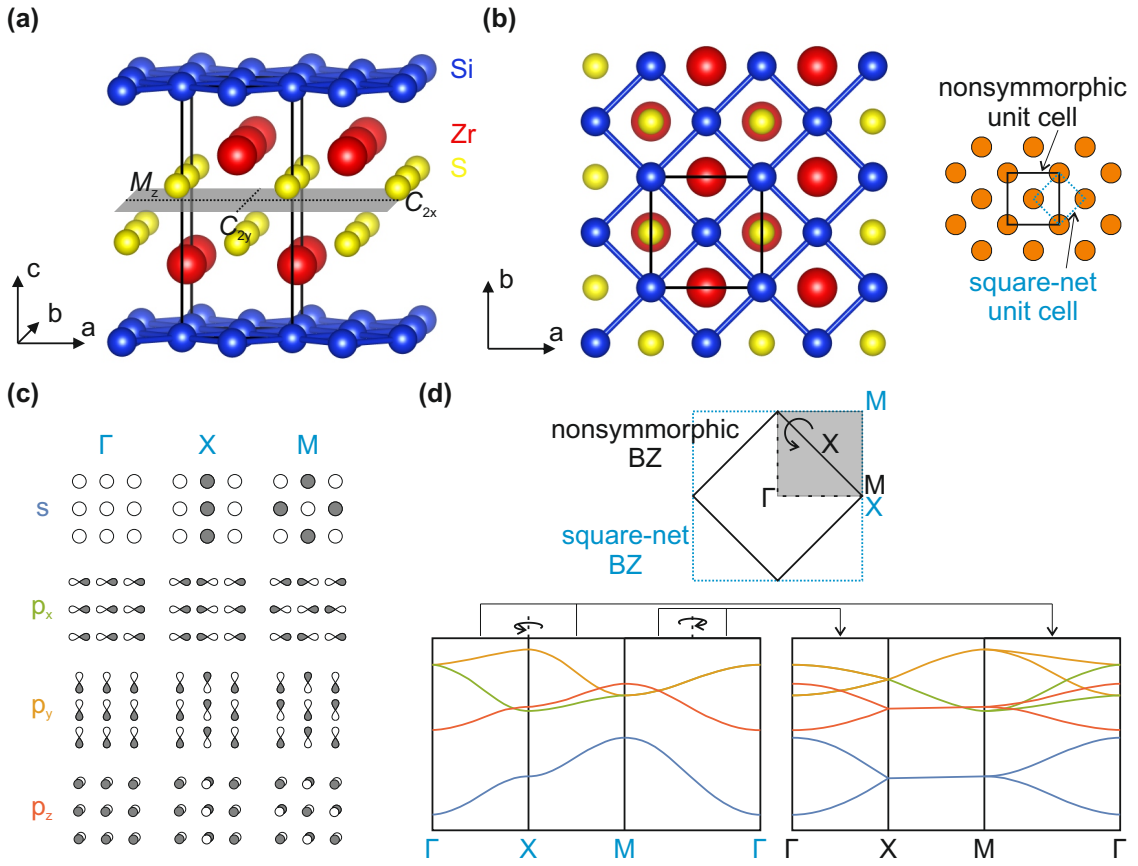

Figure 2.5: Common crystallographic and electronic features of the PbFCl structural family, crystallizing in SG 129. (a) Side view of the crystal structure of ZrSiS. The unit cell is shown in black. The Si atoms form a square net, while the nonsymmorphic symmetry elements effectively double the unit cell. (b) Top view of (a). The schematic shows the doubling and 45 ° rotation from the square-net (blue) to the nonsymmorphic (black) unit cell. (c) Phases of *s* and *p* orbitals at the high-symmetry points of the square-net BZ. White and grey colors correspond to positive and negative signs of the wavefunction, respectively. Matching phases leads to σ and π bonding, resulting in the energy dispersion of the bands. (d) BZ bisection due to the unit cell doubling and resulting back-folding of the bands in the band structure. This figure is heavily influenced by Ref. [48].

2.3 Crystal Growth

As a last preparatory step to the electronic characterization of the materials measured in this thesis, a few words about the crystal growth seem appropriate. In principle, there are several synthesis methods available to reach the required size of a few mm for the ARPES measurements described in Sec. 3.2. The growth method has a direct influence on the electronic structure however, since doping and surface defects alter the clean band structure of the conducted DFT calculations. Since this thesis is mainly concerned with the electronic property measurements though, the interested reader is referred to the Section 'Cycle of Material Development' in the book chapter of Ref. [6], which arose from the work leading to this thesis. This section will only summarize the most crucial points of the vapor transport synthesis, since it was used for most of the materials of SG 129.

Vapor transport is arguably one of the easiest ways to obtain sizable crystals. The reactants are sealed in a quartz tube together with a transport agent, which is or becomes gaseous at the required temperatures (mostly elemental halides), and heated in a furnace. A temperature gradient along the tube is used to form volatile halide transition metal intermediate products that decompose on the cold side and form the crystal. The transport agent, going from less reactive (I_2 and Br_2) to more hazardous (Cl_2 or NH_4Cl), and the temperature settings have to be chosen accordingly and are the major tuning parameters. The exact growth conditions for the materials analyzed in this thesis can be found in the published papers. For more information on the vapor transport in particular, see also Ref. [50, 51].

CHAPTER 3

Experimental Setup

The phenomena introduced in Chapter 2 are especially of relevance for experimental techniques that combine a sensitivity for bulk, as well as, surface related properties. The main tool to realize this duality used in this thesis is ARPES. This technique is based on the photoelectric effect introduced in Section 3.1 that not only allows for the measurement of the electronic (surface) structure of a material, but also the interaction of these electrons with phonons or other electrons. Besides being a powerful measurement technique, the required experimental setup is relatively easy to realize in its minimalist form (elaborated in Section 3.2). For these reasons, in recent years, ARPES has become more and more of a service tool to map out the electronic structure of new materials to confirm theoretical predictions. Nevertheless, the following chapters, especially Section 4.3, will hopefully convey the idea that ARPES measurements are still a powerful tool to make new experimental discoveries, which in turn motivates new theoretical models and theories.

The last part of this chapter, Section 3.3, will give a short overview over a neutron scattering experiment. Complementary to ARPES, neutron scattering was used to not only determine the electronic, but also the magnetic structure of a material. In this thesis, neutron scattering was mostly of interest for the magnetic members of SG 129 (see CeSbTe in Chapter 6).

3.1 The photoelectric effect

The photoelectric effect describes the behavior of a material to emit electrons if illuminated by light and was first described by Heinrich Hertz in 1887 [52]. As Albert Einstein could successfully explain, and was awarded the Nobel prize for in 1921, photons

are able to transfer their energy to the electrons in the solid and if their energy exceeds the work function of the material, these electrons can leave the material into the vacuum [53]. The intensity of the photon beam is thereby irrelevant for their ability to remove electrons, only their energy (related to the frequency as $E = \hbar\omega$) is of importance. In photoemission spectroscopy, described in the following section, we are interested in these electrons that were removed from the solid. Before one can understand the technicality of a photoemission experiment however, it seems prudent to first derive the mathematical basis for this process. To this end, the following paragraph closely follows Ref. [54], starting from Fermi's Golden Rule to motivate the introduction of the spectral function and followed by the practical application of it in the Green's function formalism. This theory is then extended by recognizing the shortcomings of the presented derivation, which is relevant for the experimental implementation.

One of the most successful approximations in the context of photoemission is the sudden approximation that assumes one electron is removed from the N electron system in the solid immediately without interacting with the remaining $N-1$ electron system. The change in potential due to the removal of the electron is stored in the remaining electrons only, which move to compensate for the loss. According to Fermi's Golden Rule, the distribution of the photoexcited electrons is given by:

$$I(\mathbf{k},\hbar\omega) \propto \sum_{s}^{\text{occupied}} \left|\langle N-1,s;\mathbf{k}|\hat{H}_{\mathrm{I}}|N,0\rangle\right|^2 \delta(E_{N,s}-E_{N,0}-\hbar\omega), \tag{3.1}$$

where $|i\rangle = |N,0\rangle$ is the N-electron ground state with energy $E_{N,0}$, $|f\rangle = |N-1,s,\mathbf{k}\rangle$ is the excited state s of the remaining $N-1$ electrons with energy $E_{N,s}$ and one free electron with wave vector $\mathbf{k}$ and energy $\varepsilon_{\mathbf{k}}$. Note that $\varepsilon_{\mathbf{k}}$ is not yet the quasi-particle energy E($\mathbf{k}$) that will be introduced in the Green's formalism later and which we are actually interested in, in an ARPES experiment. The transition operator $\hat{H}_{\mathrm{I}}$ describing the interacting part of the Hamiltonian can be expressed as:

$$\hat{H}_{\mathrm{I}} = -\frac{e}{mc}[\mathbf{A}(\mathbf{r})\cdot\mathbf{p}] + \frac{e^2}{2mc^2}|\mathbf{A}(\mathbf{r})|^2 \tag{3.2}$$

This equation results from a non-relativistic charged particle picture in an electromagnetic field in the Coulomb gauge (this takes care of the $\nabla\cdot$A term in the interaction Hamiltonian here, but needs to be treated carefully in the context of surfaces). For low enough incident photon fluxes, terms of the order $|A|^2$ can be neglected, although we have to be aware of the limitations we imply on the system. For example, we disregard two-photon processes in the following.

In the dipole approximation, we can further express the periodic, external electromag-

netic vector potential as:

$$\mathbf{A}(\mathbf{r}) = \mathbf{A}_0\, e^{i\mathbf{kr}} \overset{\text{Taylor}}{=} \mathbf{A}_0\, (1 + i\mathbf{kr} + ...) \overset{\text{Dipole}}{=} \mathbf{A}_0 \tag{3.3}$$

This approximation is valid for low enough photon energies (up to a few keV), since the resulting photo-electron velocities are relatively small compared to the speed of light and the wavelength of the light source is much larger than the size of orbitals the electrons occupy [55].

Due to the sudden approximation, we can write the final state $|f\rangle$ as:

$$|f\rangle = |N-1, s, \mathbf{k}\rangle = c_{\mathbf{k}}^{\dagger}|N-1, s\rangle, \tag{3.4}$$

with $c_{\mathbf{k}}^{\dagger}$ being the creation operator of a photo-electron. Since this also allows for the decoupling of energies, Eq. 3.1 can be written as:

$$I(\mathbf{k}, \hbar\omega) \propto \sum_s \left|\langle N-1, s|c_{\mathbf{k}}\hat{H}_{\mathrm{I}}|N, 0\rangle\right|^2 \delta(E_{N-1,s} + \varepsilon_{\mathbf{k}} - E_{N,0} - \hbar\omega) \tag{3.5}$$

We can write the transition operator in its electronic matrix representation with creation and annihilation operators:

$$I(\mathbf{k}, \hbar\omega) \propto \sum_s \left|\langle N-1, s|\; c_{\mathbf{k}} \sum_{ij} \langle i|\hat{H}_{\mathrm{I}}|j\rangle c_i^{\dagger} c_j\; |N, 0\rangle\right|^2 \delta(E_{N-1,s} + \varepsilon_{\mathbf{k}} - E_{N,0} - \hbar\omega) \tag{3.6}$$

If the photo-electron decouples immediately before any relaxation takes place (again part of the suddden approximation), then $c_{\mathbf{k}}^{\dagger} \approx c_i^{\dagger}$ and:

$$\begin{aligned} I(\mathbf{k}, \hbar\omega) &\propto \sum_s \left|\sum_j \langle \mathbf{k}|\hat{H}_{\mathrm{I}}|j\rangle \langle N-1, s|c_j|N, 0\rangle\right|^2 \delta(E_{N-1,s} + \varepsilon_{\mathbf{k}} - E_{N,0} - \hbar\omega) \\ &\propto \sum_{ij} \langle \mathbf{k}|\hat{H}_{\mathrm{I}}|j\rangle\; A_{ij}(\varepsilon_{\mathbf{k}} - \hbar\omega)\; \langle j|\hat{H}_{\mathrm{I}}|\mathbf{k}\rangle \\ &\propto \sum_{ij} \underbrace{\left|\langle \mathbf{k}|\hat{H}_{\mathrm{I}}|j\rangle\right|^2}_{\text{overlap matrix elements}} A_{ij}(\varepsilon_{\mathbf{k}} - \hbar\omega), \end{aligned} \tag{3.7}$$

where we introduce the one-electron spectral function:

$$A_{ij}(E) = \sum_s \langle N-1, s|c_i|N\rangle\; \delta(E - \varepsilon_s)\; \langle N|c_j^{\dagger}|N-1, s\rangle, \tag{3.8}$$

with $\varepsilon_s = E_{N,0} - E_{N-1,s}$ being the final energy of the solid. A physical interpretation of the spectral function we introduced here, is the probability of removing (or adding) and electron of energy E and momentum $\mathbf{k}$ to the system.

After introducing the spectral function as a concept, we now need a working form of it

for our data analysis. In Green's function formalism, on which this thesis aims to give just a short overview, the spectral function can be expressed depending on the single-particle Green's function:

$$A(\mathbf{k},E) = -\frac{1}{\pi}\,\mathrm{Im}\,\underbrace{G(\mathbf{k},E)}_{\text{Green's function}} \tag{3.9}$$

Lastly, the Green's function can be expressed depending on the interaction considered. In the easiest case, we consider non-interacting electrons, resulting in:

$$\begin{aligned} G_0(\mathbf{k},E) &= \frac{1}{E - E(\mathbf{k}) - i\eta}, \quad \eta \to 0 \\ \Rightarrow A(\mathbf{k},E) &= -\frac{1}{\pi}\delta(E - E(\mathbf{k})) \\ \Rightarrow I(\mathbf{k},\hbar\omega) &\propto \sum_j \left|\langle \mathbf{k}|\hat{H}_1|j\rangle\right|^2 \delta(\varepsilon_{\mathbf{k}} - \hbar\omega - E(\mathbf{k})) \end{aligned} \tag{3.10}$$

If we consider interacting effects like electron-phonon or electron-electron coupling, the Green's function changes accordingly:

$$\begin{aligned} G(\mathbf{k},E) &= \frac{1}{E - E(\mathbf{k}) - \Sigma(\mathbf{k},E)} \\ \Rightarrow A(\mathbf{k},E) &= \frac{1}{\pi}\frac{\mathrm{Im}\,\Sigma(\mathbf{k},E)}{(E - E(\mathbf{k}) - \underbrace{\mathrm{Re}\,\Sigma(\mathbf{k},E)}_{\substack{\text{energy}\\ \text{renormalization}}})^2 + (\underbrace{\mathrm{Im}\,\Sigma(\mathbf{k},E)}_{\substack{\text{life time}\\ \text{broadening}}})^2} \qquad (3.11) \\ &= \frac{1}{\pi}\frac{\Gamma}{(E - E(\mathbf{k}))^2 + \Gamma^2} \qquad (3.12) \end{aligned}$$

The last step holds true for $\Sigma(\mathbf{k},E) = i\Gamma$ purely imaginary and constant. The spectral function has then the shape of a Lorentzian with Γ determining the width of the peak. It is therefore possible to determine the life time of the analyzed electronic states by means of line profile analysis. The self-energy Σ therein contains all the information concerning the interaction with other electrons and the lattice. For now, let's only consider the first picture of non-interacting electrons as it is mostly sufficient in the context of this thesis and motivates well the initial state properties investigated in this work.

Before continuing with the experimental details relevant for an ARPES experiment, there is one more important detail when it comes to the photoemission process. So far, we did not consider the path the electron has to take from the bulk of the solid to the surface and into the vacuum. Historically, there are two models describing this process [56]. The 'three-step model' is historically older and more intuitive. The photocurrent depends on three independent factors, the excitation probability in the bulk, the scat-

tering probability of the excited electron on its path to the surface and the transmission probability of said electron through the surface of the solid and into the vacuum. These steps are treated independently and can not interfere. Depending on the process one is interested in, e.g. valence band spectroscopy or core level spectroscopy, one or some of these probabilities can be set to unity to simplify the calculation. In contrast, the 'one-step model' treats these steps together and always considers interference between these effects [57]. It is, therefore, intrinsically more accurate, at the prize of clarity, since it condenses all scattering processes into the coherent final state of the matrix element from Eq. 3.7. This theory is usually used nowadays since the true final state is required for the accepting of the photoelectron later at the detector. Nevertheless, it should be mentioned that there are considerable shortcuts to this model, if one knows about the system and what one is interested in to learn about it.

In the sudden approximation of the derivation above, we did not pay attention to any of these models and neglected the (in)elastic scattering events that take place. One of the most obvious consequences of inelastic scattering is the energy loss an electron perceives on its way to the surface. While the photons can penetrate deep into the bulk, most electrons have lost their kinetic energy or changed their direction via scattering after a few nm, which means that deeper electrons can not leave the crystal anymore and photoemission experiments usually only probe the first few atomic layers. The inelastic mean-free path (IMFP) proved to be a valuable tool for calculating this escape depth and as it turns out, it is mostly independent of the material considered. Fig. 3.1 shows the IMFP determined from a phenomenological equation by Seah and Dench

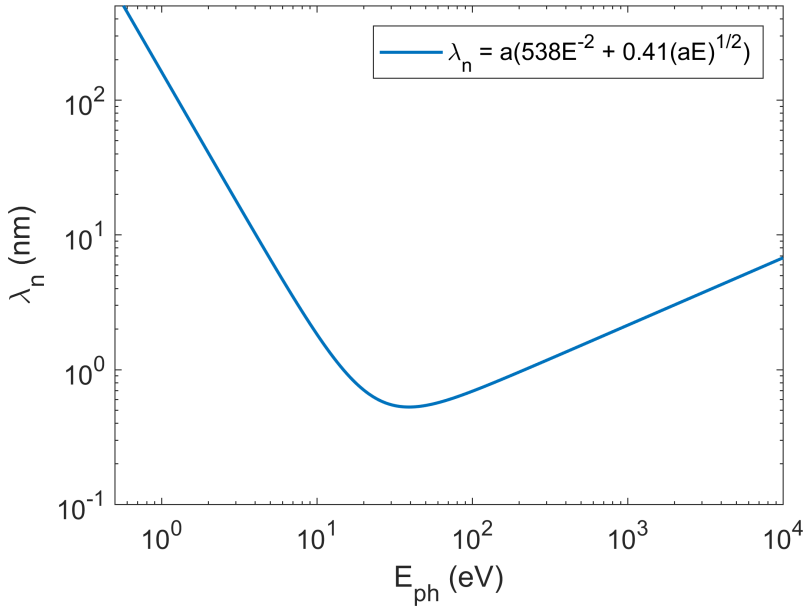

Figure 3.1: Universal curve of the inelastic mean-free path. Equation from Ref. [58] with monolayer thickness a.

[58]. The ARPES experiments carried out in this thesis vary between 20 and 700 eV. The minimum in this range limits the depth to several Å only. This does not have to be a major disadvantage though, since it allows photoemission to be relatively surface sensitive even for high photon energies and a modification of the top-most layer is usually not obscured by a too high intensity of bulk bands. Since our derivation was only concerned with elastic scattering so far, the exact way, in which the inelastic background is taken care of, will be presented in the following section.

3.2 Angle-resolved photoemission spectroscopy

The goal of this section is to give the working understanding of an ARPES experiment. Many of the theoretical concepts developed in Sec. 3.1 are important for the ideas presented here, but in its practical application, we do not tend to think, for example, about the sum over all occupied states, but instead multiply our fit spectra with a Fermi-Dirac distribution to also take care of the temperature effects in our sample. In this spirit, the following section will not give a one-to-one relation from the theoretical derivations, but show their functional form and only hint at their origin form the previous section. For a more thorough derivation, the reader is referred to Ref. [6, 59].

Figure 3.2(a) shows a typical ARPES setup. Monochromatic light with a specific energy $\hbar\omega$ enters the sample and transfers its energy to an electron, which, if close enough to the surface (above the order of the IMFP), will leave the sample and be collected by a hemispherical analyzer, which has a specific angle θ to normal emission. The analyzer can then determine the number of counts in a kinetic energy region defined by the applied voltage. Should this, so called 'fixed mode' energy window not suffice, several overlapping spectra can be obtained while slowly changing the energy region ('swept mode'). This basic buildup is identical in most ARPES experiments. What distinguishes the measurements in the lab from beamtime results is mainly the light source, which will be elaborated in the following sections.

During the photoemission process, energy and momentum need to be conserved if we consider only elastically scattered electrons, which leads to two fundamental equations. Let us first consider energy conservation, which results from the δ function in Eq. 3.10. Fig. 3.2(b) presents the situation of a core level or valence band electron that is excited above the work function of the sample Φ_S, introduced in Sec. 2.1.3, to escape into the vacuum. On the analyzer site, this free electron is distinguished by its kinetic energy. From this picture it is relatively easy to see that we have to consider the work function of the analyzer Φ_A in the energy conservation, since the analyzer spectrum is

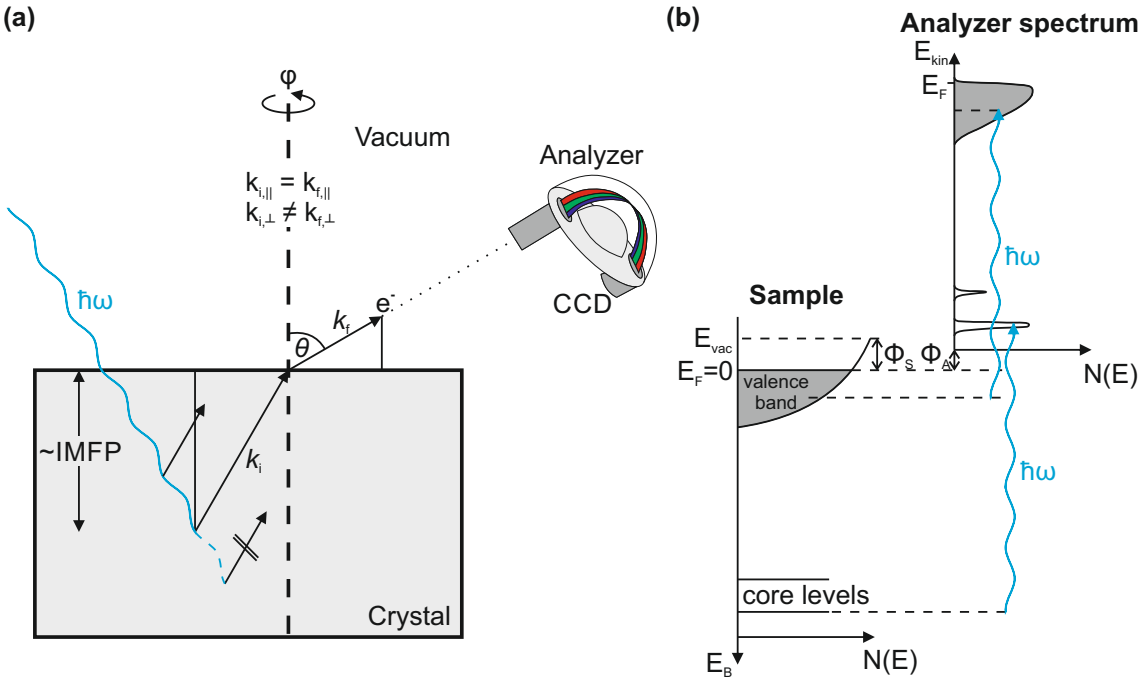

Figure 3.2: (a) Illustration of the photoemission process in the ARPES setup. Mainly electrons above the IMFP contribute elastically to the spectrum. When scattering at the surface, only the parallel component of the wave vector is conserved. Note that k and real space are shown in the same picture. Picture from Ref. [6]. (b) Illustration of the photoemission process in the electron density of sample and analyzer. Note that the work function Φ of sample and analyzer do not need to be identical, but only Φ_A enters the energy conversion law. Analyzer and sample spectrum after Ref. [59].

what gives us the kinetic energy of the electrons:

$$\begin{aligned} E_{\text{kin}} &= \hbar\omega - \Phi_{\text{S}} - E_{\text{B}} \quad \text{, or} \\ E_{\text{i}} &= E_{\text{kin}} - \hbar\omega + \Phi_{\text{S}} \\ &= E_{\text{kin}} - E_{\text{kin}}(E_{\text{F}}), \end{aligned} \tag{3.13}$$

Here, E_{i} is the initial state energy (which is the negative binding energy) and E_{F} is the energy of the Fermi level.

Momentum conservation on the other hand will allow us to assign the collected $N(E_{\text{kin}})$ signal to a specific $\mathbf{k}$ direction. The number of electrons collected will be identical to the intensity $I(E_{\text{kin}})$ in the following. Fig. 3.2(a) does not only contain the real space geometry of the setup but also sketches the movement of the electrons at the surface. The refraction process at the surface does only preserve the in-plane component of the momentum vector $\mathbf{k}_\parallel$ and hence, we obtain for negligible photon momentum:

$$k_{\text{i},\parallel} = k_{\text{f},\parallel} = \frac{\sqrt{2m}}{\hbar}\sqrt{E_{\text{kin}}}\,\sin\theta. \tag{3.14}$$

Knowledge of the kinetic energy of the electrons and their escape angle to the sample normal is therefore sufficient to measure a line profile for one k point called the energy distribution curve (EDC). Such an EDC, taken at a photon energy of $\hbar\omega = 70\,\text{eV}$, is shown in Fig. 3.3.

Above the Fermi level at 65.6 eV, the intensity is reduced to zero (apart from random noise), since there are no occupied states available for the photoemission process. As mentioned in the beginning of this section, this behavior, as well as the temperature broadening of the Fermi level is modeled by a Fermi-Dirac distribution, located at $\hbar\omega - \Phi \approx 70\,\text{eV} - 4.4\,\text{eV}$. The peaks, each representing a band crossing or touching this k point, have Lorentzian shape and are superimposed by the Shirley background. The first term of the iterative Shirley/Sherwood method can be expressed as [60]:

$$I_{\text{Shirley}}(E) = c \int_{E}^{\infty} \mathrm{d}E'\; I(E') \tag{3.15}$$

Originally a phenomenological way of modeling the contribution of inelastically scattered electrons, it has been shown that the Shirley background results from a specific

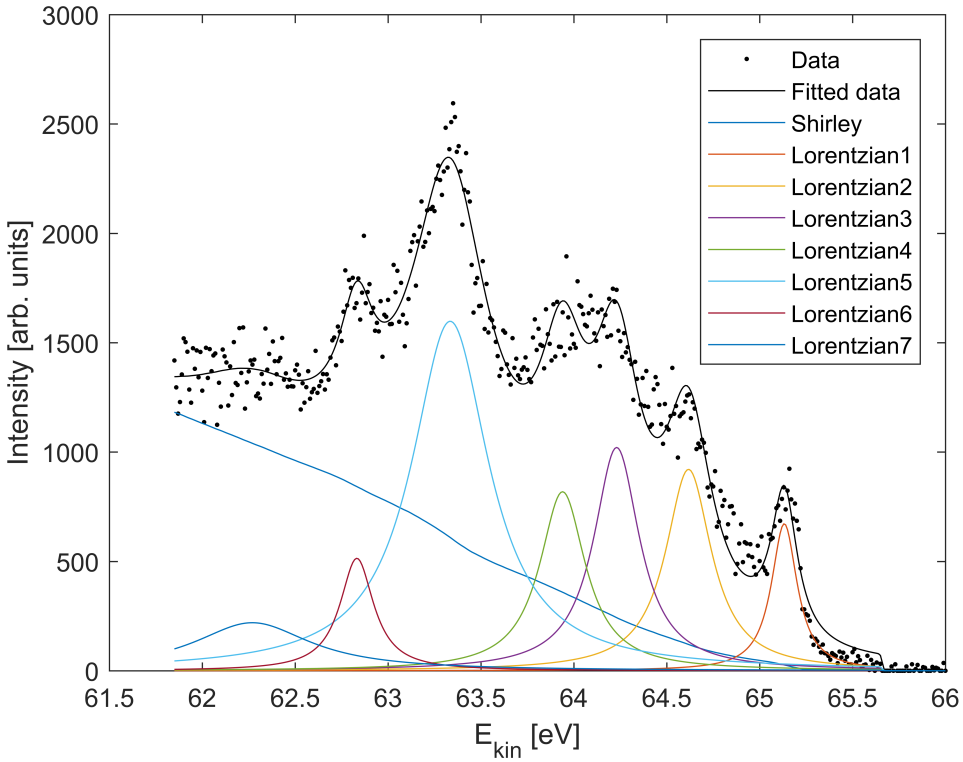

Figure 3.3: ARPES EDC for a photon energy of $\hbar\omega = 70\,\text{eV}$. The black fit curve is obtained by subtracting the Shirley background and fitting the spectrum to several Lorentzian peaks multiplied by the Fermi-Dirac distribution around the Fermi level. Picture from Ref. [6].

form of the inelastic energy-loss cross section [60].

Modern analyzers determine the kinetic energy not only at one point at a time, but along a slit angle α on a CCD chip. The result is a 2D intensity picture consisting of several EDC lines, shown in Fig. 3.4. During an ARPES experiment, θ is then changed in small steps to obtain the dispersion relation along a specific direction, resulting in a data cube $I(E_{\mathrm{kin}},\theta,\alpha)$. From a constant E_{kin} cut through this cube, it is apparent that the Γ point of the first BZ is not located at $(\alpha,\theta) = (0,0)$, which is a result of the glueing process of the single crystal making perfect horizontal alignment very difficult. Since it is only a linear offset however, a simple subtraction of the cube data takes care of this in most cases where the first BZ is easily identified. In practice a tilt angle in many manipulators allows for the correction of the α offset and θ can just be chosen accordingly. After this offset correction, the transformation into k space is taken care of by Eqs. 3.13 and 3.14 in addition to a transformation along the slit angle, which results from simple geometric considerations:

$$\begin{aligned} E_{\mathrm{i}} &= E_{\mathrm{kin}} - E_{\mathrm{kin}}(E_{\mathrm{F}}) \\ k_x &= \frac{\sqrt{2m}}{\hbar}\sqrt{E_{\mathrm{kin}}}\sin\alpha\cos\theta \\ k_y &= \underbrace{\frac{\sqrt{2m}}{\hbar}}_{\approx 0.512\,\text{Å}^{-1}/\sqrt{\text{eV}}}\sqrt{E_{\mathrm{kin}}}\sin\theta \end{aligned} \tag{3.16}$$

It would be preferable to identify $k_x = 0$ and $k_y = 0$ with high-symmetry lines in the BZ, which is not automatically given with a random glueing of the crystal in the in-plane direction. Before the cube is recorded in the experiment, this can be accounted for through the φ angle of Fig. 3.2(a). Otherwise, during data analysis, this can be corrected by multiplying the data cube with a rotation matrix:

$$\begin{pmatrix} k_x \\ k_y \end{pmatrix} = \begin{pmatrix} \cos\varphi & -\sin\varphi \\ \sin\varphi & \cos\varphi \end{pmatrix}\begin{pmatrix} k_x \\ k_y \end{pmatrix} \tag{3.17}$$

After discussing the parallel components of the k vector, let us now consider the perpendicular direction $k_\perp = k_z$, which is not preserved at the surface. k_z is usually obtained by tuning the photon energy, while remaining at a constant (k_x, k_y) position. The first Γ point is ideally suited for such a measurement, since it also remains constant in angle space when changing the photon energy. For a free-electron-like final state approximation, $k_{\mathrm{i},\perp} = k_z$ can be obtained by

$$k_z = \frac{\sqrt{2m}}{\hbar}\sqrt{E_{\mathrm{kin}}\cos^2\theta + V_0}, \tag{3.18}$$

where V_0 is determined by fitting to a periodic behavior of the initial state energy of the

bands $E_i(\hbar\omega)$.

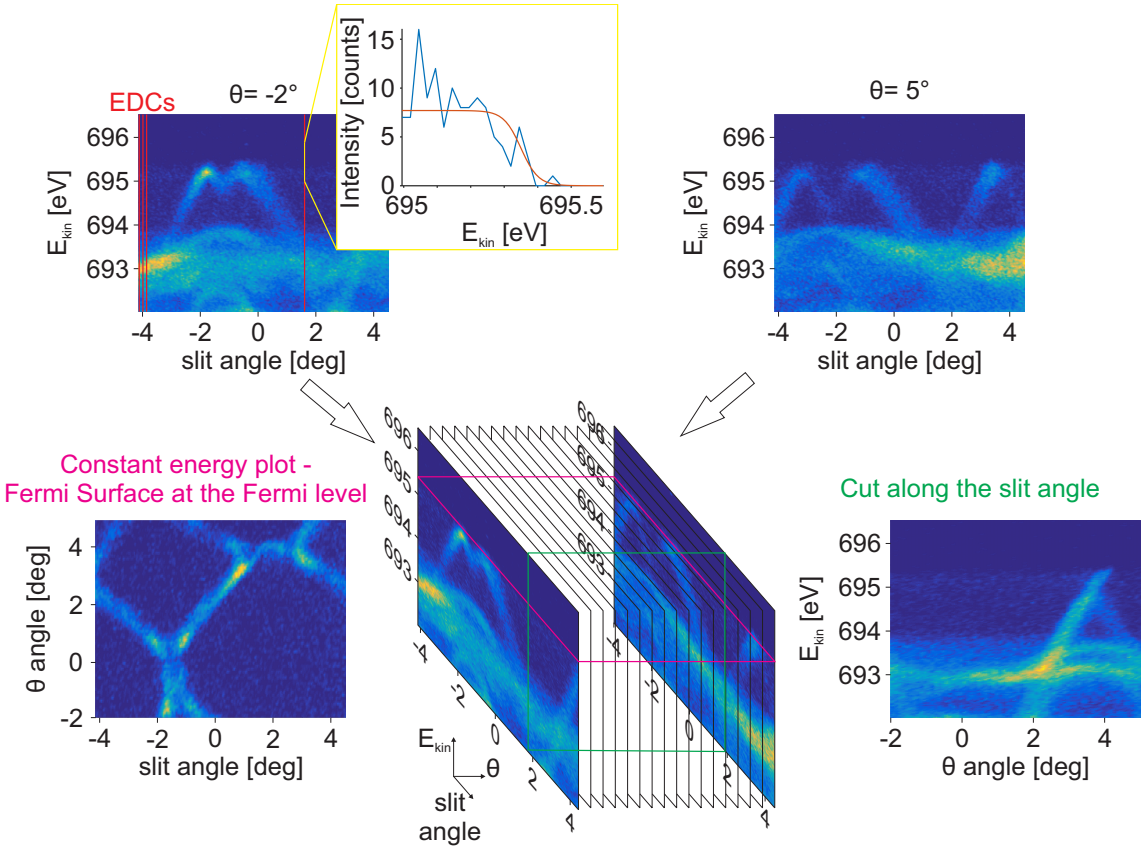

Figure 3.4: The process of acquiring ARPES data on the example of ZrSiS at $\hbar\omega = 700$ eV. For several θ angles, 2D intensity pictures consisting of individual EDCs are collected. The Fermi level can be determined by fitting to a Fermi-Dirac distribution. A stacking of all recorded θ angles results in a data cube, which can be cut to obtain the Fermi surface. Picture from Ref. [6].

It should be noted here that not all measurements are necessarily angle-resolved, just because the experiment allows for it. The core levels for example disperse only very little, so it is far more practical to integrate over the complete slit angle α. Since high photon energies are required to lift the core levels above the Fermi level and into the vacuum, core level spectroscopy is often also called X-ray photoemission spectroscopy (XPS). XPS was regularly performed during this work, since it allows the characterization of the elemental composition. Furthermore, the exact position of the f level in the lanthanides of Chap. 6 and 8 was necessary to fix the U parameter in the respective DFT+U calculations [61].

3.2.1 Lab 7B15

Experiments performed at the Max Planck Institute for Solid State Research (MPI FKF) in Stuttgart used a monochromatic He lamp with photon energies of $\hbar\omega = 21.2$ eV (He

I) and $\hbar\omega = 40.8\,\text{eV}$ (He II). The hemispherical SPECS PHOIBOS 150 electron analyzer has an energy and angular resolution of about 15 meV and 0.5 °, respectively. All measurements were conducted on crystals cleaved *in situ* at room temperature in the low 10^{-10} mbar pressure range. Since the resolution and variability of photon energy allowed for better results at synchrotrons, only the presented initial measurements on ZrSiS of Chap. 4 were performed with this setup.

3.2.2 Synchrotron Bessy II

Instead of using a gas lamp with a fixed photon energy, one can use synchrotron radiation (radiation produced by electrons in a particle accelerator) that has a wide spectrum, and a monochromatized beam of an undulator-based beamline can provide high-intensity in combination with variable energy and light polarization. Most measurements with a photon energy between 20 and 120 eV were performed at the 1^2-ARPES experiment installed at the UE112-PGM-2a beam line at Bessy-II in Berlin. The analyzer has an energy resolution of down to 1 meV for photon energies below 100 eV and an angular resolution of 0.1 °. Measurements can be performed with LHe down to 40 K.

3.2.3 Synchrotron APS

All soft x-ray ARPES measurements (photon energies between 248 and 1000 eV) were performed at the 29ID-IEX beam line at the Advanced Photon Source (APS) at the Argonne National Laboratory in Chicago. The hemispherical Scienta R4000 electron analyzer has an energy and angular resolution of 220 meV and 0.1 °, respectively. Measurements can be performed with LN_2 and LHe at variable temperatures down to 8 K.

3.3 Neutron scattering

During the course of the magnetic structure determination of CeSbTe, presented in Chap. 6, a neutron diffraction beamtime was conducted. Since the principle of elastic neutron scattering is not the main focus of this thesis, we will refrain from giving a derivation of the Bragg peak structure of the scattering rate starting from Fermi's Golden Rule, but provide the working knowledge to understand the data collected at the beamtime.

Neutron diffraction is, like electron diffraction, a tool to resolve the atomic structure of a material. These methods are therefore complementary to the electronic characterization we discussed above. Like in photoemission experiments, the electron scattering experiment is thereby limited to a few atomic layers (surface-sensitive), while

neutron scattering does not experience the strong Coulomb interaction and is therefore a bulk probe. Furthermore, neutrons with the necessary wave length to detect interatomic distances ($\lambda \approx 2\,\text{Å}$) have only energies of tens of meV, while electrons are in the order of eV already. This makes them in principle susceptible to different kinds of excitations in an inelastic scattering experiment, which we will not go into detail here. The attenuation of the coherent scattering due to neutron adsorption is furthermore a factor to be considered before designing an experiment with e.g. boron or gadolinium.

For an elastic neutron diffraction experiment, a neutron source supplies the incoming, beforehand monochromatized, neutrons with initial momentum $\mathbf{k}_\text{i}$ and spin projection σ_i, which will be collected by an analyzer after the scattering took place. Here, the differential cross-section, the number of neutrons scattered into a solid angle element per time, is measured. This happens for various angles around the sample and the spectrum can then be plotted against this angle. If the Bragg reflection condition is fulfilled, one observes coherent interference resulting in a Bragg peak under this angle and collecting all these peaks in a powder diffraction experiment allows one to determine the lattice structure. These peaks are furthermore dampened by a form factor, taking care of interference effects similar to the form factor in x-ray scattering.

One of the biggest advantages when it comes to neutron scattering is the additional spin a neutron carries, compared to x-ray diffraction. The magnetic neutron scattering will result in its own magnetic Bragg peaks (which can be identical in case of a ferromagnet) with a magnetic form factor, reducing the Bragg reflections with large reciprocal magnetic lattice vectors. Additional peaks appearing in the diffraction pattern for temperatures below the magnetic phase transition temperature can therefore be used to determine the magnetic structure reliably.

For all practical purposes, a software package allows to refine the diffraction pattern, which results in the nuclear or magnetic structure, given the elements are known.

The powder neutron diffraction data were collected on the WISH instrument at ISIS, Harwell Oxford [62], between 1.5 and 5 K to gather data above and below the T_N of CeSbTe. The diffraction patterns were refined by the Jana2006 software [63].

CHAPTER 4

ZrSiS - The First Nonsymmorphic Dirac Nodal Line Semimetal[1]

Understanding is a three-edged sword. Your side, their side, and the truth.

– OLD VORLON PROVERB

The discovery of Graphene ignited a new field of research and was later even awarded with the Nobel prize 2010 [64]. One exciting aspect of graphene lies in its electronic structure, which features linearly dispersing bands over a wide energy range and a four-fold crossing point at the Fermi level. This results in massless Dirac fermions as low-energy quasi-particle excitations. Real-world applications, however, uncover several difficulties when working with a 2D material in a 3D environment. For example, while suspended graphene shows ultra-high mobilities in the order of 10^5 cm^2/Vs, substrate-induced scattering will reduce this number considerable when using graphene in field effect devices [65, 66]. It is for this reason that the research focus shifted towards 3D Dirac and Weyl semimetals that have similar electronic properties and exhibit exotic transport properties such as ultra-high mobility and large, linear and negative magnetoresistances, but are intrinsically already 3D removing the necessity of a substrate [67, 68, 69, 70]. Many of the known semimetals struggle though in their usefulness in applications, since they contain toxic elements and their band crossings are not close enough to the Fermi level, or rather the crossing is convoluted by additional bands [43].

Already in 1986, Tremel and Hoffmann [49] published their ideas on 'Square Nets of Main Group Elements in Solid-State Materials', of which ZrSiS was one example. They showed its interesting electronic properties, but focused on the effect of distortions

[1] This chapter is based on the publications [1, 3]

and complicated superstructures. As it turns out, the square net in ZrSiS does not distort and many of the attributes of SG 129, which were introduced in Sec. 2.2, can already be observed here. ZrSiS is, therefore, the first Dirac nodal line semimetal that also comprises nonsymmorphic crossings. Since it is further a non-toxic and earth-abundant material, ZrSiS had template character for the materials to come in Chapters 5, 6 and 7.

Section 4.1 will introduce the design concept behind ZrSiS and show the theoretically expected and experimentally determined band structure. The discrepancy in theory and experiment allows for the identification of a rich surface band structure. The quasi-two dimensional nature of the bands close to the Fermi level in ZrSiS make it, however, difficult to distinguish between bulk and surface bands in the photon energy dependent measurements presented in Section 4.2. It is here that the unusual properties of the surface states play a role for the first time, since they are clearly resolved up to a photon energy of 700 eV. The properties of these surface states will then be discussed further in Sec. 4.3. Since they do not fit any of the surface state categories of Sec. 2.1.4 or 2.1.5, this section will also develop the theoretical concept of a symmetry reduction at the surface and show how a broken nonsymmorphic symmetry can lead to the observed 'floating' surface states.

4.1 Exemplary band structure of space group 129

It has been shown in Sec. 2.2 that, depending on the position of the Fermi level, a material of the PbFCl structure type can be regarded as a Dirac semimetal. Therefore, it seems to be prudent to evaluate the electron count in ZrSiS once, as an example for the materials in the following chapters.

A simple electron counting and electronegativity approach for ZrSiS results in an oxidation state of +4 and -2 for Zr and S, respectively. This leaves an oxidation state of -2 for Si in the square net. On one hand, this is beneficial, since this does not allow for a completely filled p-band, which would otherwise result in a trivial insulator. On the other hand, a system consisting of only s- and partially filled p-bands is unstable in the square-net structure and undergoes the aforementioned distortions [49]. In ZrSiS, however, the overlap of the strongly bonding Si p- and Zr d-bands stabilizes the antibonding Si-Si bond. In this configuration, each Si atom forms two lone pairs and has two electrons available for four bonds, which results in a delocalized bonding network in the square net [48, 49, 71].

As mentioned above, ZrSiS was the first compound of an isostructural family of materials crystallizing in SG 129. For this reason, the atomic structure has been mapped

out carefully with scanning electron microscopy (SEM), low-energy electron diffraction (LEED), high-resolution transmission electron diffraction (HRTEM) and precession electron diffraction (PED), which all confirm the expected square-net structure. The results of the mentioned measurements are presented in Fig. 4.1. Most importantly for the following ARPES measurements, the LEED pattern shows the Γ points ordered in a square structure without any surface reconstruction.

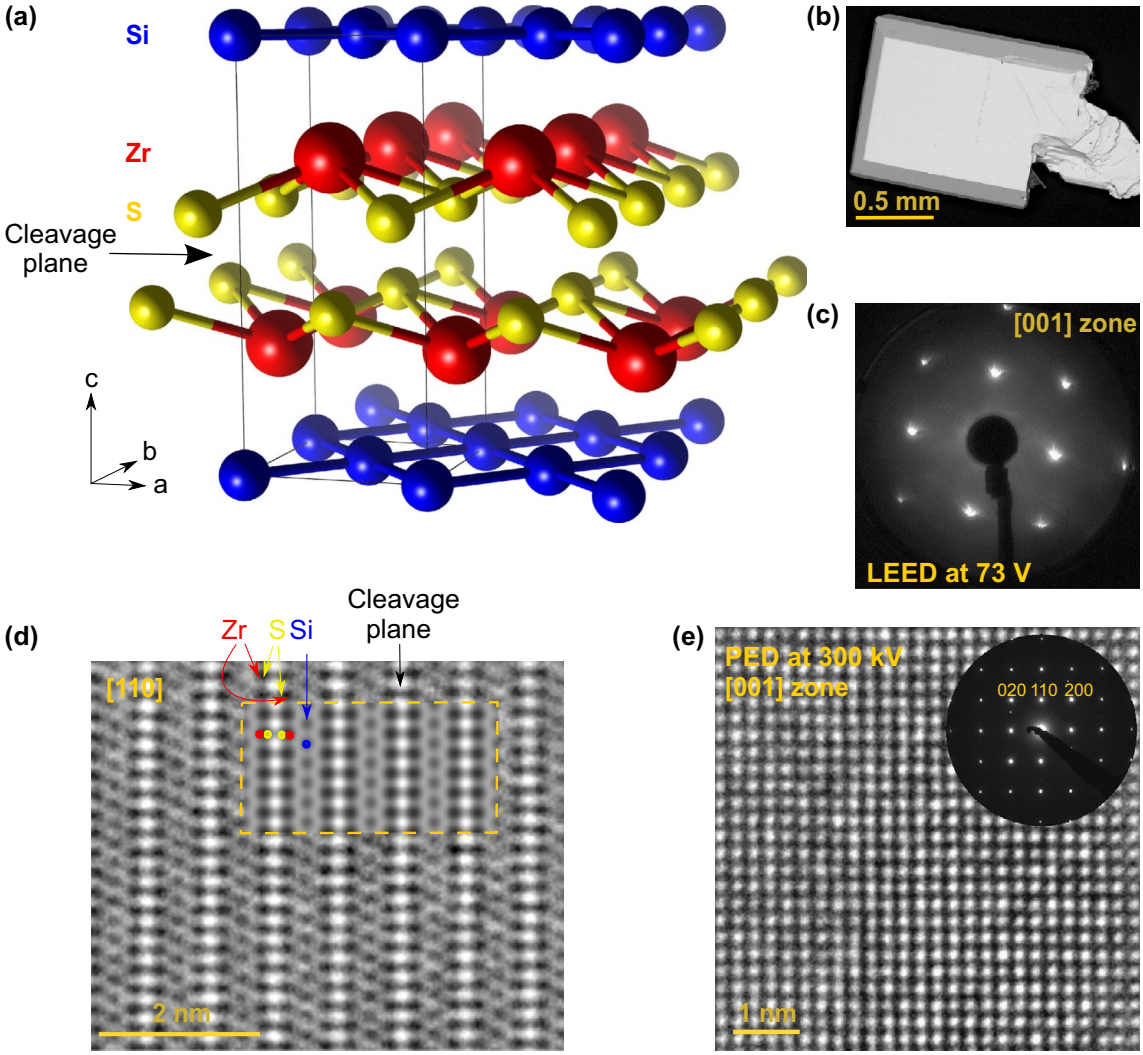

Figure 4.1: Structural characterization measurements of ZrSiS. (a) Crystal structure with the unit cell shown in black. (b) SEM image of a ZrSiS crystal. The crystals grow in the *ab* plane. (c) LEED pattern of a cleaved crystal taken at 73 eV. (d) HRTEM image of the [110] orientation with a focus plane of $\Delta f = -50\,\text{nm}$. Atoms appear in black. The inset shows the simulated pattern. (e) HRTEM and PED pattern of the [001] surface. The square-net structure is clearly resolved and shows no distortions. Picture adapted from Ref. [1].

Based on this crystal structure, DFT calculations without SOC were performed and are shown in Fig. 4.2(a) and (b). Since ZrSiS is a centrosymmetric material and no magnetic

field is applied, all bands are two-fold spin degenerate. The dispersion is shown along a path through the 3D BZ, which is shown in Fig. 4.2(c). For completeness and since it is important for the comparison with the ARPES data in the following, the surface BZ is presented here as well and shows the surface projection of the bulk BZ points. The colors in (a) and (b) represent different irreducible representations (irreps) of the bands, and since only bands of different irreps can cross in the band structure, certain bands already show a gapping further away from the Fermi level. However, at E_F, the

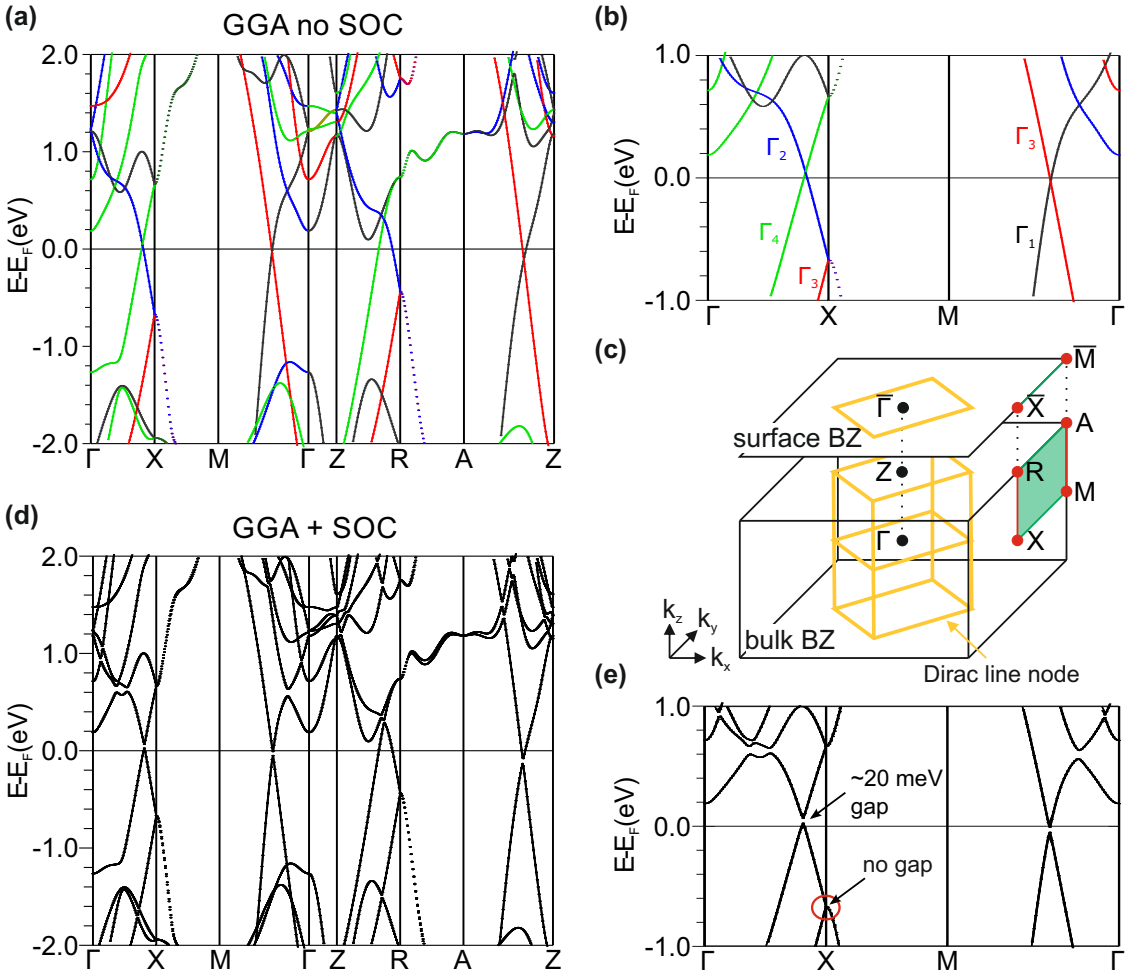

Figure 4.2: DFT calculations of ZrSiS, (a) and (b) without SOC. The colors represent different irreducible representations. The bands form a Dirac line node that has a cage like structure around Γ and are degenerate in the $k_x = \pi$ and $k_y = \pi$ plane due to the nonsymmorphic symmetry. (c) 3D BZ with surface projection along [001]. The Dirac line is indicated in yellow and the nonsymmorphic symmetry projection in green (without SOC) and red (with SOC). (e) and (f) Band structure along the same path in (a) and (b). The Dirac line node gaps slightly due to the low atomic mass and subsequent small SOC strength, but the nonsymmorphically protected X and M points (R and A, respectively) stay degenerate, indicated by the red circle. Picture adapted from Ref. [1].

only bands crossing the Fermi level all form linearly dispersing Dirac crossings and, as hinted towards in Sec. 2.2, indeed form a Dirac line node that has a diamond shape around the Γ and Z point. The line node is schematically shown in yellow in (c). The diamond-like shapes of the line node in the $k_z = 0$ and $k_z = \pi$ plane connect along k_z and form a cage in the 3D BZ, while still projecting as a diamond in the surface BZ. The exact energy of the line node is not fixed to the Fermi level and it varies slightly along its path in the 3D BZ. A tight-binding approach on this line node with a colored energy representation is given in Sec. 5.2, since the nodal line is important for understanding the drumhead surface state in ZrSiTe. For now it is sufficient to assume the nodal line in the $k_z = 0$ and $k_z = \pi$ plane fall on top of each other in the projection and the nodal line is close enough to the Fermi level to dictate most of its transport properties. Independently of the Dirac line node, the nonsymmorphic symmetry in SG 129 enforces the expected degeneracies at X and M (R and A, respectively) that are, in the absence of SOC, extended along the complete high-symmetry line and plane X-M-A-R, marked in red and green in Fig. 4.2(c).

Fig. 4.2(d) and (e) consider the same path through the 3D BZ as (a) and (b), but including SOC as a second variational process. Since SOC reduces the number of irreps, the nodal line is no longer protected and gaps as indicated in Fig. 4.2(e). The gap was optically determined to be below 30 meV [72], which is relatively small due to the low atomic mass of the incorporated elements. A similar gapping can be observed along the X-M and R-A direction, although it is too small to be resolved in any ARPES measurement. A comparison with a heavier member of SG 129 will be given in Sec. 6.2. With SOC, only the X-R and M-A high-symmetry lines are nonsymmorphically protected (shown in red in Fig. 4.2(c)), which results in a crossing at the $\overline{\text{X}}$ and $\overline{\text{M}}$ point in the surface BZ that does not gap independently of the strength of the SOC. It would be desirable to have this nonsymmorphic crossing closer to the Fermi level, to have it contribute more to the transport properties, which motivated the characterization of ZrSiTe in the following chapter 5.

We can now compare these theoretical expectations with the experimental data collected with ARPES, shown in Fig. 4.3. This will lead to the discovery of a surface state that is not part of the bulk band calculations, which will be derived in the following Sec. 4.3.

When we look at the $\overline{\Gamma}$-$\overline{\text{X}}$-$\overline{\text{M}}$ line collected at $\hbar\omega = 21.2$ eV, it is relatively straightforward to identify the lower part of the Dirac line node, marked in purple in Fig. 4.3(a). The linearly dispersing bands do not cross exactly at the Fermi level, which can be explained by a slight doping of the analyzed crystals. Surprisingly, an additional state appears, seemingly crossing the bulk bands (marked as 'Surface State' in (a)). Since this additional state does not match the DFT bulk band calculations, this leaves two potential explanations for its appearance in the experimental spectra. Either the DFT calculations are not correct, which we exclude due to its perfect reproduction of the other bulk

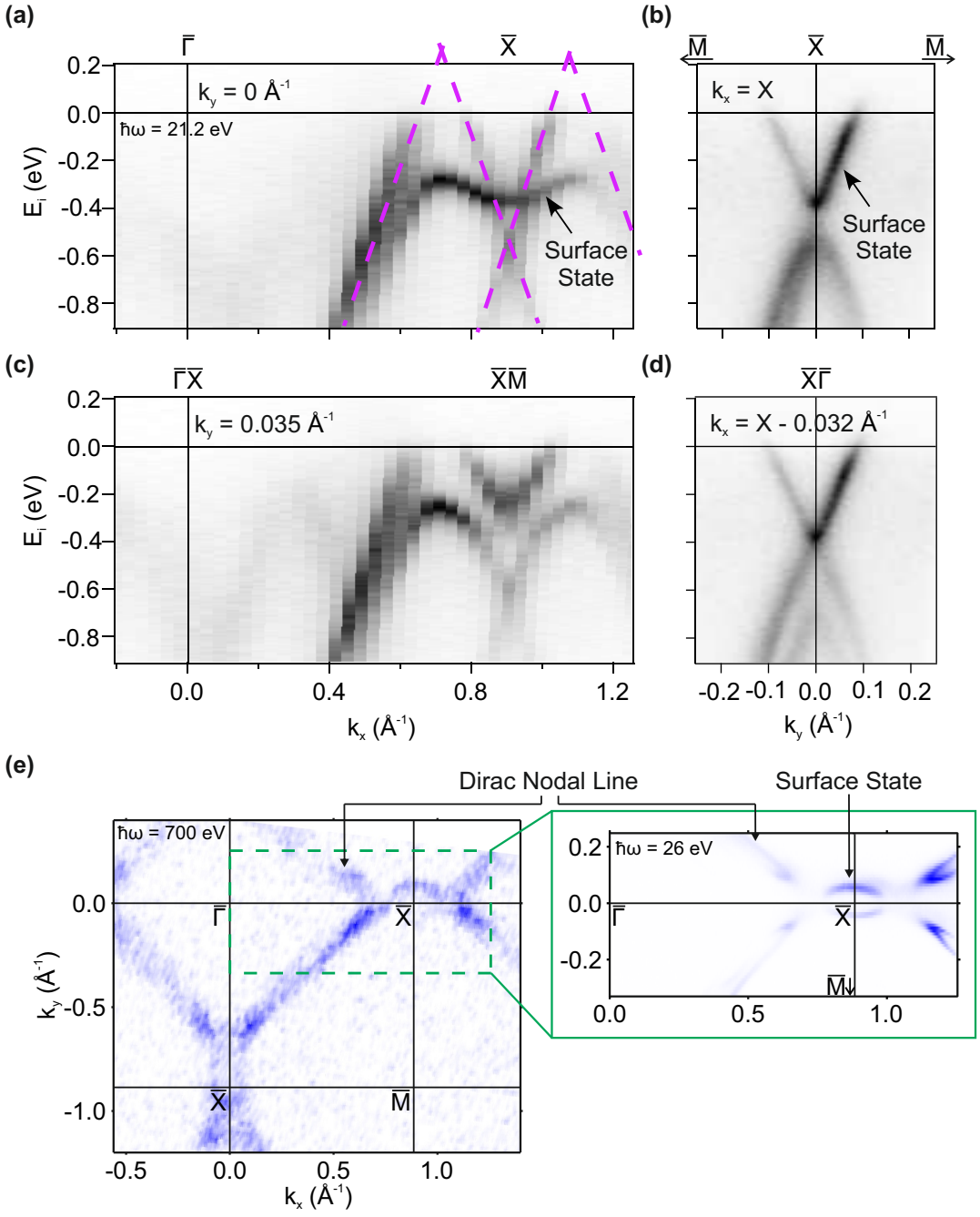

Figure 4.3: ARPES measurements of ZrSiS. (a) Dispersion along $\overline{\Gamma}$-$\overline{X}$-$\overline{\Gamma}$. Bands forming the Dirac line node are superimposed by purple lines. Additional states, which are not part of the DFT bulk band calculations are labeled surface states. (b) Dispersion along $\overline{M}$-$\overline{X}$-$\overline{M}$ showing the surface state dispersion upwards above the Fermi level. (c) Dispersion parallel to (a). (d) Dispersion parallel to (b). Surface bands consist of several parts running in parallel to the bulk bands. Subfigures (a) - (d) were collected at a photon energy of $\hbar\omega = 21.2\,\text{eV}$ and are adapted from Ref. [1]. Subfigure (e) was measured at $\hbar\omega = 700$ and 26 eV and is adapted from Ref. [3].

bands, or the additional state is surface-derived. ARPES, as a surface-sensitive measurement would naturally measure a combination of bulk and surface bands, while the bulk DFT would only catch the bulk bands. As it turns out, this is indeed the case in ZrSiS and related compounds, hence the name-giving of the observed state in (a). However, before we talk about the origin of this surface state, it is reasonable to analyze its progression in reciprocal space first. In Fig. 4.3(b), a cut orthogonal to (a), $\overline{\text{M}}$-$\overline{\text{X}}$-$\overline{\text{M}}$, is shown where the surface state runs from -0.4 eV initial state energy up to the Fermi level. Again, in Fig. 4.2(b), along X-M there are no bulk bands expected to cross the Fermi level, which allowed us to identify the course of the surface state. Moving away from the high-symmetry lines in Fig. 4.3(c), it becomes evident that the surface state is not really crossing the bulk bands in (a), but consists of several parts that mostly run in parallel to the bulk bands and are only distinguishable where they do not. This is a common feature of surface states in SG 129, which will be more apparent in the surface bands of CeSbTe and will be discussed further in Sec. 6.2. The same holds along a parallel dispersion path of (b), presented in Fig. 4.3(d), which is shifted just enough to reach the crossing point of bulk and surface bands in (a), slightly away from the $\overline{\text{X}}$ point. The upper surface band seemingly flows into the lower bulk band, without a hint to the character of these bands, if it were not for the DFT bulk band calculations.

At the Fermi surface, presented in Fig. 4.3(e), the Dirac line node proceeds as expected in a diamond-like fashion around the $\overline{\Gamma}$ point. The inset of the $\hbar\omega = 700$ eV Fermi surface was taken with a bigger tilt angle at $\hbar\omega = 26$ eV, which explains the difference in detail of the two Fermi surfaces. The surface state is clearly visible around the $\overline{\text{X}}$ point as a ring-like feature.

To confirm the surface derivation of the observed states, it is possible to simulate the effect of a surface in DFT by performing slab calculations. A supercell is defined along the c axis containing a slab of five ZrSiS unit cells intermittent by a 5.3 Å vacuum gap (see Fig. 4.4(a)). The termination layer of the slab was chosen between the sulfur atoms, in accordance with the HRTEM data in Fig. 4.1(d). To compare the calculations with the Fermi surface in Fig. 4.3(e), the DFT bands crossing the Fermi level were projected to the surface independent of their k_z value. Fig. 4.4(b) shows the resulting theoretical Fermi surface for the ZrSiS unit cell (bulk) and the newly defined supercell (slab). Since the energy of the line node is not fixed to the Fermi level, the diamond-shape around the $\overline{\Gamma}$ point is slightly extended in both figures. This is in agreement with the line node observed in experiment. Especially at 26 eV in Fig. 4.3(e), the line node is clearly resolved to consist of two bands crossing slightly above the Fermi level. The biggest difference between the bulk and slab DFT calculation is marked in orange, showing an additional contribution to the Fermi surface in the form of a ring-like shape around the $\overline{\text{X}}$ point, which is in perfect agreement with the surface state observed in experiment. The agreement between DFT slab calculation and ARPES experiment becomes even more apparent, when we superimpose the high-symmetry line dispersions

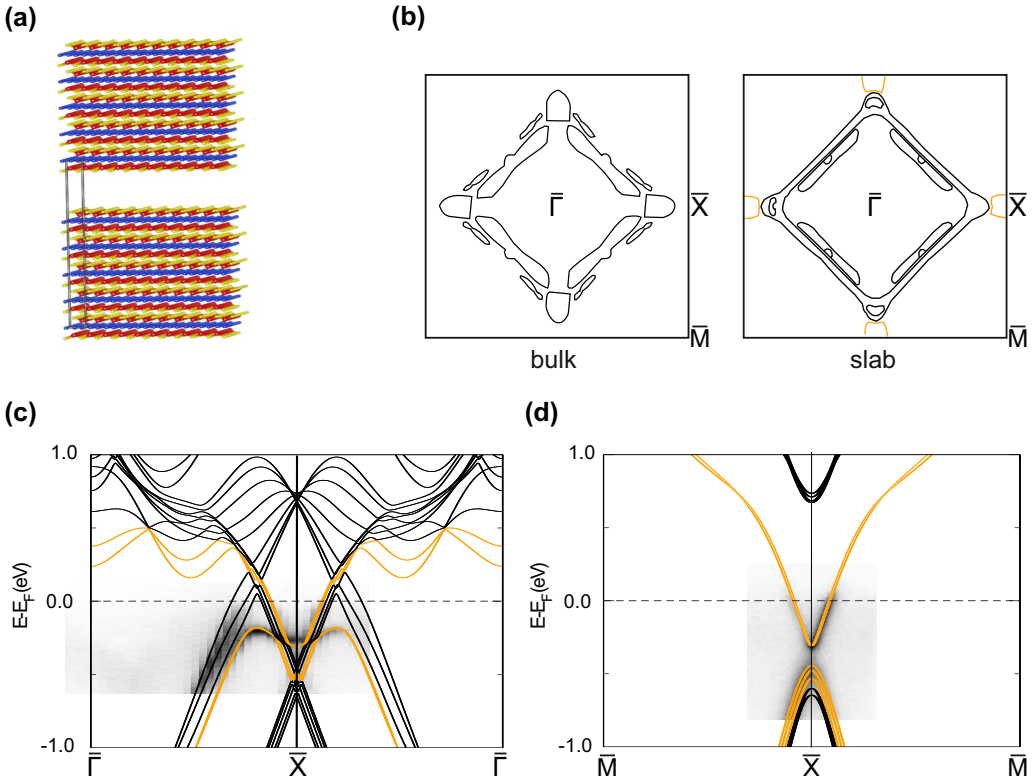

Figure 4.4: DFT slab calculations of ZrSiS. (a) Supercell used for the DFT slab calculation consisting of 5 unit cells intermitted by a 5.3 Å vacuum gap. (b) DFT Fermi surface comparing the bulk and slab calculations. The surface states appear as a ring-like structure around the $\overline{\text{X}}$ point consistent with the experimental observation. (c) ARPES dispersion along the $\overline{\Gamma}$-$\overline{\text{X}}$-$\overline{\Gamma}$ direction superimposed by the DFT slab calculation. (d) The same along the $\overline{\text{M}}$-$\overline{\text{X}}$-$\overline{\text{M}}$ direction. The surface bands consist of several parts resulting in a seeming crossing of bulk and surface states. Subfigures (b) - (d) adapted from Ref. [1].

in Fig. 4.4(c) and (d). It is quite common for DFT calculations to require a stretching factor along the energy axis to fit to the experimental data. In ZrSiS however, the band dispersion fits perfectly, at least down to $E_\text{i} = -1\,\text{eV}$. The surface-derived bands (again shown in yellow) were identified by comparison with the bulk DFT calculations of Fig. 4.2. From their course, our assessment of the different parts of the surface state is confirmed and an additional surface band could even be identified following the bulk bands at $E_\text{i} = -0.45\,\text{eV}$ to lower initial state energies along $\overline{\text{X}}$-$\overline{\text{M}}$ in Fig. 4.4(d).

Despite the surface states crossing the Fermi level, the transport properties of a conductive material are mostly dominated by its bulk properties. ZrSiS shows exotic physical properties like an extremely large and nonsaturating, butterfly-shaped anisotropic magnetoresistance and nearly massless Dirac fermions with a strong Zeeman splitting in de Haas-van Alphen oscillations [73, 74, 75, 76], as well as, an effective mass enhancement for high magnetic fields [77], which are a clear indicator of the influence of

the Dirac line node.

4.2 3D vs 2D nature of bulk bands

To identify surface states in ARPES measurements, it is common to compare the k_z dispersion of the states in question. Since surface states are restricted to the surface, they should in principle show no k_z dispersion at all, while bulk states occupy different initial energies depending on the k_z plane measured. In ARPES, the photon energy is changing k_z according to Eq. 3.18. This allows to distinguish between bulk and surface states, by plotting the inital state energy versus photon energy and observe an oscillatory behavior in the bulk states (since $k_z = \pi$ equals $k_z = -\pi$), and a constant in the surface states. Figure 4.5(a) shows the dispersion along the $\overline{\Gamma}$-$\overline{\mathrm{X}}$-$\overline{\Gamma}$ direction around $\overline{\mathrm{X}}$ for different photon energies between $\hbar\omega$ = 20 and 40 eV. Since the matrix elements vary with photon energy and especially between different Brillouin zones, the branches of the bands around $\overline{\mathrm{X}}$ change in intensity depending on the photon energy. By following the energy of the maxima (blue and green) of the surface state slightly off and the minimum (violet) of the surface state at the $\overline{\mathrm{X}}$ point and comparing them to the energy of the nonsymmorphically protected bulk band crossing at the $\overline{\mathrm{X}}$ point (red), the dispersion shown in Fig. 4.5(b) can be obtained. While the photon energy independent behavior of the potentially surface-derived states (green, blue and violet), at first glance, strengthens the theory of emergent surface states, the bulk state crossing in red shows no dispersion as well. This is mostly due to the layered composition of the ZrSiS structure, which results in a weakly dispersing bulk behavior in this energy range as well. Already in the slab calculations of Fig. 4.4(c), the black bulk bands below the Fermi level lie almost on top of each other, although they result from different k_z planes. Comparing these results with Fig. 4 of Ref. [1], a small deviation in the variation from the mean value can be noticed, which is mostly due to a photon energy arrangement error in the published data. Because we observe a straight line though, this error leads to the same conclusion in the end, namely that neither the bulk nor the surface states show any dispersion. This even holds true, when we consider far higher photon energies in Fig. 4.5(c), although the broadening of the bands make it exceedingly difficult to determine the exact position of the bands in this case.

On the note of unusual behavior, it has to be mention that the surface states appear to be unaffected by the high photon energies, which was taken for granted in Fig. 4.3(e) and Fig. 4.5(c). This is however not at all trivial and will be discussed here. As has been noted in Sec. 3.1, Fig. 3.1, the IMFP increases with increasing photon energy. In the case of ZrSiS, this implies an increase of the IMFP from 0.49 nm for 26 eV to 1.43 nm for 700 eV [58]. Since no optical measurements of the IMFP exist for ZrSiS yet, it is not possible to obtain the IMFP directly from such data. Therefore, the increase of

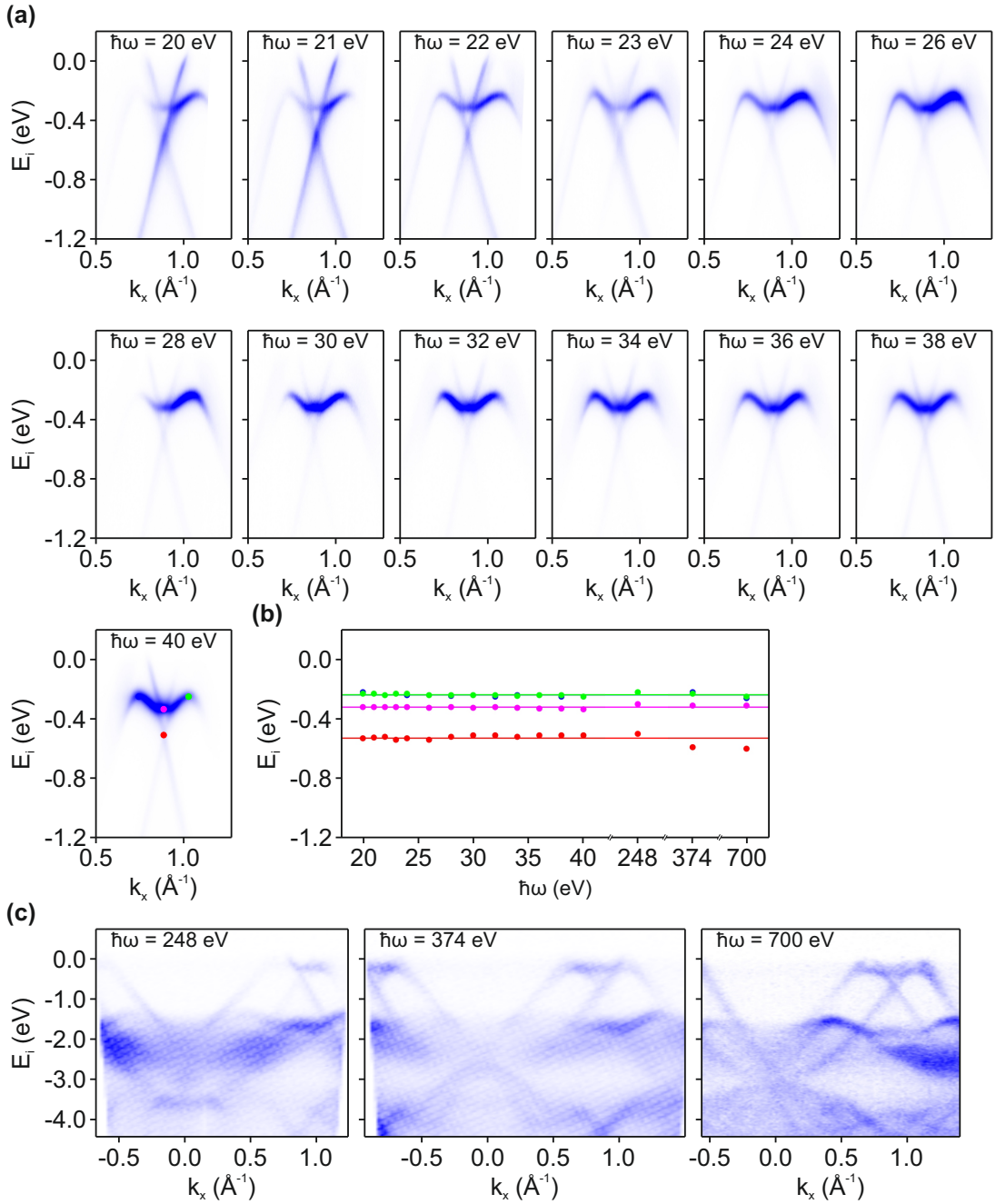

Figure 4.5: Dispersion along $\overline{\Gamma}$-$\overline{X}$-$\overline{\Gamma}$ around $\overline{X}$ for different photon energies between (a) 20 and 40 eV and (c) 248, 374 and 700 eV. (b) Photon energy dependency of the surface state maxima (blue and green), surface state minimum (violet) and bulk band crossing (red). None of the states show a noteworthy or oscillatory k_z dispersion, which is due to the 2D nature of the surface states and the quasi-2D nature of the bulk bands in a layered material like ZrSiS. Subfigures (a) and (b) adapted from Ref. [1]. 700 eV dispersion of subfigure (c) from Ref. [3].

a factor of ≈ 3 is only a rough estimation. Regardless, an increase in the relative intensity between bulk and surface states is only expected if the increase of the IMFP outweighs the increase in created and annihilated phonons. Otherwise, the increase in phonon-assisted non-direct transitions would smear out the initial states with increasing photon energy. A good way to quantify this behavior is the Debye-Waller factor

$$W(T) = \exp\left[-\frac{1}{3}\,\Delta k^2(\hbar\omega)\,\langle u^2(T)\rangle\right], \tag{4.1}$$

where $\Delta k(\hbar\omega) = k_\mathrm{f} - k_{\hbar\omega} - k_\mathrm{i}$ and $\langle u^2(T)\rangle$ is the 3D mean-square vibrational displacement [78]. A Debye-Waller factor $W > 50\,\%$ allows to resolve the bands individually, but for ARPES a $W > 90\,\%$ is usually aimed for. For $W < 10\,\%$, only the density of states is visible and the bands are smeared out over the complete Brillouin zone [79]. Due to the high Debye temperature of ZrSiS (≈ 493 K [80]), we were able to obtain nicely resolved ARPES spectra even at room temperature. The Debye temperature is a rough estimation at which temperature the vibrational displacement $\langle u^2(T)\rangle$ starts to play a significant role in the negative exponent of the Debye-Waller factor (exact formula in Ref. [78]). A high Debye temperature, therefore, allows for a high Debye-Waller factor over a larger temperature range. As delineated by Hofmann et al. [81], the effect of a higher photon energy can also be modeled by increasing the temperature. Going to higher photon energies, while decreasing the temperature allows us, therefore, to retain our high Debye-Waller factor. Just from this argument, we would expect an increase in bulk band intensity compared to the surface band intensity, since the increase in the IMFP increases the bulk band probing depth.

However, the increase in photon energy also influences the surface states directly, which led to the calculation of individual Debye-Waller factors for surface and bulk states in the literature [82]. Depending on the system, the thermal motion (again, the lower wavelength for higher photon energies allows for an equivalent behavior of temperature and photon energy in this argument [81]) can be higher at the surface, since the bonding environment is reduced [82], effectively reducing the Debye temperature for the surface initial states. On the other hand, the reduced dimensionality at the surface facilitates coherent emission, which can in special cases lead to a high surface sensitivity at high photon energies [81]. Without an extended temperature study, which is beyond the scope of this thesis, this question cannot be answered sufficiently.

For this reason, we will argue here, that the continuing, but slightly less intense appearance of the surface states for high photon energies is due to the increase in IMFP. The perseverance against phonon-induced nondirect transmissions, however, hints towards a strong localization of the surface states at the surface [81], which is in accordance with the 'floating' surface states theory, presented in the following.

4.3 'Floating' surface states

Despite the surface states not interfering too strongly with the electronic properties of the bulk bands, it is still worthwhile to investigate their origin. Exploring the common origins of surface states, cf. Secs. 2.1.4 and 2.1.5, the list becomes quickly exhausted, without providing insight to the source of surface states in ZrSiS. For example, the weak SOC might be sufficient to gap the Fermi level, which would result in topological surface states, should the gap be non-trivial [83]. However, ZrSiS belongs to the same class as ZrSiO, when it comes to its topological properties, which was found to be a weak topological insulator with a $\mathbb{Z}_2$ topological invariant of (0; 001) [84]. This result is in agreement with our own parity analysis based on Eq. 2.30 of the previously presented DFT data. Therefore, ZrSiS is a weak topological insulator, but notably with the dark surface being the (001) surface, which is where the unknown surface states appear. This excludes a topological explanation on the basis of TI surface states. ZrSiS also shows no detectable surface reconstruction ruling out dangling bonds, which were already unlikely because of the semimetallic nature of ZrSiS, but will be discussed in more detail at the end of this section. Its clean surface without alloying or band bending also gives no incentive for a dimensional confinement of the electrons, which could result in quantum well states. And lastly, the surface states appear in an area that is not governed by an inverted band gap, which excludes Shockley states. For a more in-depth analysis on the mentioned exclusion criteria, see Ref. [3].

Before describing the 'floating' surface state theory developed during this Ph.D. work to explain this new type of surface state in nonsymmorphic materials, let us first evaluate the properties of these states that hints towards this origin and motivates this explanation. Fig. 4.6(a) and (b) show the dispersion along $\overline{\Gamma}$-$\overline{\mathrm{X}}$-$\overline{\mathrm{M}}$ measured by ARPES with a photon energy of $\hbar\omega = 26\,\mathrm{eV}$ and calculated by a DFT slab without SOC, respectively. Here, a slab size of seven unit cells was chosen, which yields the same information as the previous calculation based on five unit cells. The surface band (SS) appears again as a very intense feature in the spectrum in (a). Furthermore, a second surface state at $E_\mathrm{i} \approx -1.7\,\mathrm{eV}$ (SS') crosses the $\overline{\mathrm{X}}$ point. Both are reproduced by the DFT slab calculation and can be identified by their strong Zr orbital character (indicated by the radius of the red cycles). Using VASP, the band character can be determined by calculating the absolute value of the overlap between the respective state and the spherical harmonics, representing the orbital character [85]. We can understand the orbital character choice of Zr for identifying the surface bands, when we look at the isosurfaces of the surface band for different k points. For now, let us focus on the upper surface state that was first discovered in the original paper [1], although the same argument holds for the lower surface state SS' as well. Fig. 4.6(d) shows constant electronic density isosurfaces of the surface unit cell in real space (indicated in Fig. 4.6(c) where cleaving removed half of the bulk unit cell). The electronic density producing the surface band shows mostly Zr

d_{z^2} and S p character at the $\overline{\text{X}}$ point, while it shifts to Zr d_{z^2}, d_{xz} and d_{yz} orbital character for the dispersion towards $\overline{\Gamma}$ and $\overline{\text{M}}$. The Si p band seems to have no influence on the surface state character.

4.3.1 Potassium evaporation

One of the first extraordinary properties the surface state (SS) showed during its characterization was its modification, but not annihilation, by potassium evaporation at 40 K. Fig. 4.6(e) and (f) show the ARPES spectrum and DFT slab calculation along $\overline{\Gamma}$-$\overline{\text{X}}$-$\overline{\text{M}}$ for a surface covered with 1 monolayer of potassium. In the DFT calculations this was achieved by covering the surface with a regular array of one K atom per unit cell and allowing them to relax, resulting in a distance of 2.74 Å from the surface. In the direct comparison with the bare surface of the panels (a) and (b), the bulk bands seem to change very little, except for a slight doping effect. The surface band SS, in contrast, splits into two branches, one connecting below the Fermi level (SS1) and one following the bulk bands from above the Fermi level along $\overline{\Gamma}$-$\overline{\text{X}}$ and dispersing back above E_{F} along $\overline{\text{X}}$-$\overline{\text{M}}$ (SS2). The DFT calculation shows exactly the same behavior, if we ignore states that arise from the regular K lattice (green squares), which are necessary for the calculation but not present in reality. The gapping of surface states that appears around the $\overline{\text{X}}$ point and reveals the different branches of the surface state is nothing new, remembering the effect of SOC in the DFT slab calculations of Fig. 4.4(c). We can therefore conclude that the surface modification results in a mixing of the orbital characters, as would an artificially increased SOC, which in turn is responsible for the observed avoided crossings. Since the strength of SOC is very weak in ZrSiS, this effect is not intrinsically observable, but is enhanced by the surface potential variation by the potassium monolayer.

While qualitatively agreeing with the ARPES data, the gap size between the different surface state branches is much bigger in the DFT calculations. There are several reasons for the overestimation of the surface state gap size in DFT. Most obviously, the distance of the K layer to the surface plays an integral part in the gap size, since in the limit of very large distances, the orbital mixing is not present anymore, resulting in the ungapped and single surface state without potassium. This might imply that the relaxed potassium distance determined by DFT is slightly off. Furthermore, the chosen coverage of one K atom per unit cell is definitely not accurate, since experimentally, an error of 10 % is not uncommon in metal evaporators. A partial monolayer, or partial bilayer might very well result in a different relaxed distance and can explain the observed difference to the ARPES data.

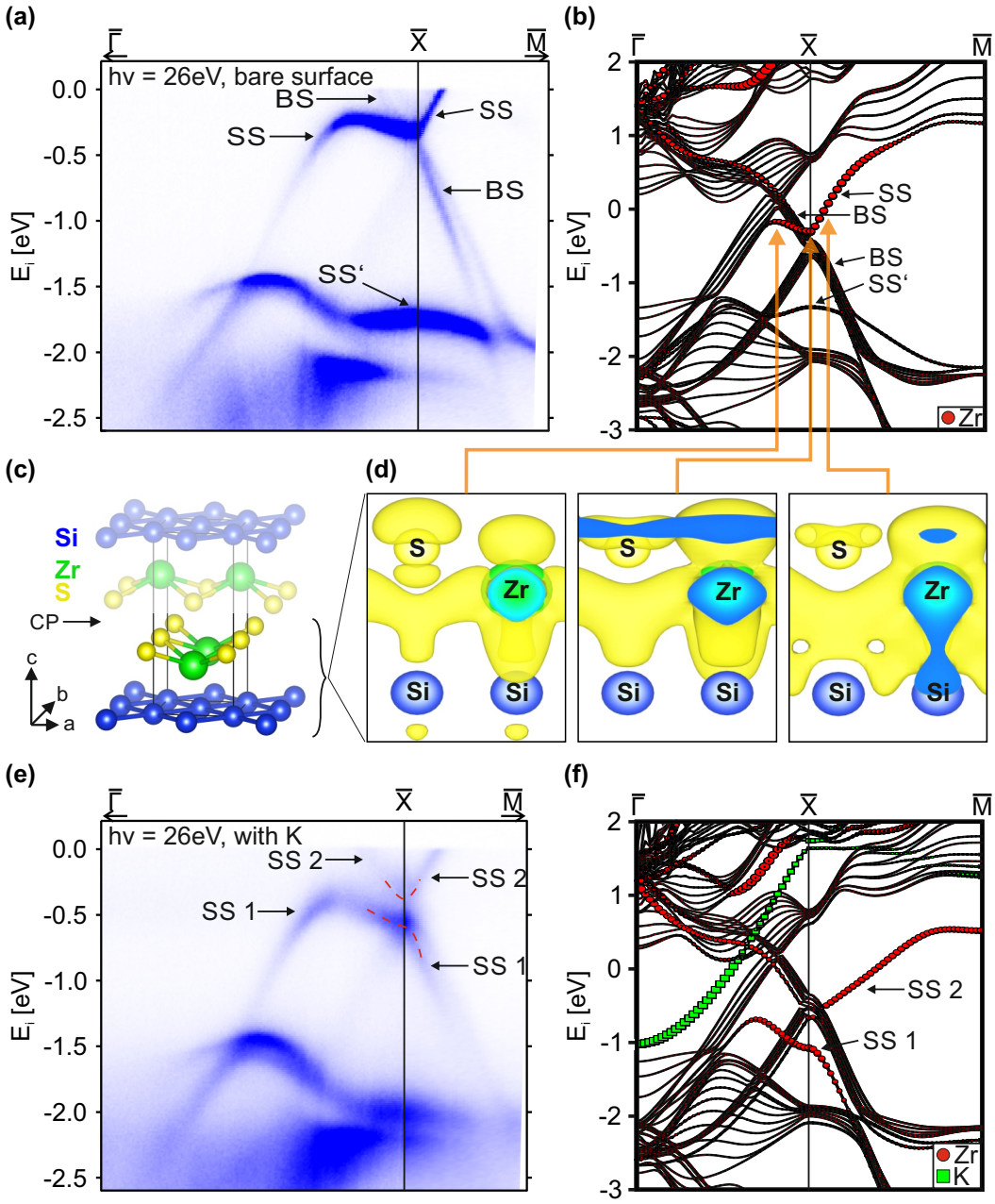

Figure 4.6: (a) ARPES data on ZrSiS taken at $\hbar\omega = 26\,\text{eV}$ along $\overline{\Gamma}$-$\overline{\text{X}}$-$\overline{\text{M}}$. The spectrum consists of intense surface states crossing the bulk bands forming the nodal line. (b) DFT slab calculations without SOC of the dispersion path in (a). The surface state character is highlighted by showing the strength of Zr *d* orbital character of the bands as the radius of red circles. (c) Surface unit cell after cleaving. (d) Isosurfaces of the surface band for different k points around $\overline{\text{X}}$. The electronic density is shown around the last surface atoms of (c). The extended blue area stems from the inner side of the isosurface, where it cuts the pictured cell. (e) and (f) ARPES data and DFT slab calculations without SOC for a monolayer of K evaporated at 40 K. The surface state SS splits up into two branches SS1 and SS2. The states due to the regular K array in (f) is shown in green squares and is expectedly not matched by the experimental data. Figure adapted from Ref. [3].

4.3.2 Tight-binding model and 'floating' surface state theory

Surfaces have the, sometimes unenviable, property to break the periodicity of the crystal structure, which is defined by its atomic basis and the symmetries of the space group. A semi-infinite crystal is then expressed by a reduced symmetry group at the surface. In a crystal with inversion and time-reversal symmetry, for example, all bands are forced to be spin-degenerate. Nevertheless, the bands can be spin-split by SOC at the surface, since inversion symmetry is no longer preserved there. This is commonly known as the Rashba effect [86], although inversion symmetry is only one of the many symmetries that is broken by the surface.

In ZrSiS for example, the cleavage along the (001) plane additionally breaks all of the nonsymmorphic symmetries. Since the nonsymmorphic symmetry is responsible for the degeneracy at the $\overline{\mathrm{X}}$ and $\overline{\mathrm{M}}$ points in the bulk, this crossing point of the bands is no longer enforced in the reduced space group of the surface. The theory of 'floating' surface states assumes the states to proceed, depending on the surface potential, in an area usually not accessible to the bulk bands, since they are no longer constrained by their crossing at the high-symmetry points. Since the surface breaks inversion symmetry, these surface bands should be furthermore spin-split by SOC, although this will not be resolvable in ZrSiS with the low atomic masses of the incorporated elements. SOC should therefore not be the driving mechanism responsible for these surface states and it should be possible to explain them in a spinless model.

To validate this theory, DFT calculations are not the method of choice, since it models all of the surface contributions in parallel, which will predict the surface states, but not allow us to retrace their source. For this reason, a tight-binding model was developed during the course of this thesis. As explained in Sec. 2.1.2, it would be desirable to explain the occurrence of these states qualitatively with relatively few parameters (here an effective four-band model in Fig. 4.7(b)) and catch the states quantitatively with more parameters fitted to the DFT calculations (shown in Fig. 4.7(c) in a 26-band model).

To develop the model Hamiltonian, let us first consider the symmetries of the ZrSiS bulk, the tetragonal SG 129. The, for our theory relevant symmetries, are the nonsymmorphic glide plane $\bar{M}_z = \{M_z|\frac{1}{2}\frac{1}{2}0\}$, which expresses a mirror along $\hat{z}$ and a half unit cell translation along $\hat{x}+\hat{y}$, two screw axes $\bar{C}_{2x} = \{C_{2x}|\frac{1}{2}00\}$ and $\bar{C}_{2y} = \{C_{2y}|0\frac{1}{2}0\}$, a mirror M_{xy} and lastly the combination of time-reversal symmetry $\mathcal{T}$ and inversion symmetry $\mathcal{I}$. Further, we consider a spinless model, which results in the schematic symmetry situation shown in Fig. 4.7(a). Due to the combination of $\mathcal{TI}$, all bands are two-fold degenerate. The combination of time-reversal symmetry and the nonsymmorphic symmetries enforces four-fold crossings at TRIMs (solid colors), while the symmetries $\bar{M}_z$, M_{xy} and the combinations $\bar{C}_{2x}\mathcal{I}$ and $\bar{C}_{2y}\mathcal{I}$ allow for accidental four-fold crossings of

different symmetry eigenvalues throughout the BZ (dashed lines). The former is responsible for the nonsymmorphically protected points, while the latter results in the forming of the nodal ring in ZrSiS.

In a spinless model Hamiltonian, we catch this situation by defining two nonsymmorphic sublattices A and B (eigenvalues of the Pauli matrix τ_z), related by their half unit cell translation along $\hat{x}+\hat{y}$. We further define two orbitals (eigenvalues of σ_z), which can be even or odd with respect to $\bar{M}_z$. The band Hamiltonian $\mathcal{H} = \sum_{\mathbf{k}} \Phi^\dagger_{\mathbf{k}} H_{\mathbf{k}} \Phi_{\mathbf{k}}$ is then acting on the basis $\Phi_{\mathbf{k}} = |c_{A,+}, c_{A,-}, c_{B,+}, c_{B,-}\rangle_{\mathbf{k}}$. The $c_{a,i}$ are creating an electron in the sublattice $a = A, B$ with an orbital $i = +, -$, even or odd under $\bar{M}_z$. If we consider time-reversal and the spacial symmetries, this results in the symmorphic part of the hopping Hamiltonian $H^{\mathrm{s}}_{\mathbf{k}}$, which preserves the sublattices:

$$H^{\mathrm{s}}_{\mathbf{k}} = \mu + m\sigma_z + t^{\pm}_{xy}(\cos k_x + \cos k_y)\sigma_{\pm} + t^{\pm}_z \cos k_z \sigma_{\pm}, \tag{4.2}$$

with $\sigma_{\pm} = 1 \pm \sigma_z$ being the projector into the even or odd orbital sectors.

Coupling the sublattices A and B is the nonsymmorphic part of the hopping Hamiltonian

$$H^{\mathrm{ns}}_{\mathbf{k}} = t[1 + \cos k_x + \cos k_y + \cos(k_x + k_y)]\tau_x + t[\sin k_x + \sin k_y + \sin(k_x + k_y)]\tau_y, \tag{4.3}$$

with the hopping coefficients of the sublattices being fixed relatively to each other [87] and the overall hopping Hamiltonian being the addition:

$$H_{\mathbf{k}} = H^{\mathrm{s}}_{\mathbf{k}} + H^{\mathrm{ns}}_{\mathbf{k}} \tag{4.4}$$

With some initially guessed parameters, the bulk band structure of a four-band model, shown in white dashed lines in Fig. 4.7(b), is obtained. We used $\mu = -0.1$, $m = 0.5$, $t^-_{xy} = -t^+_{xy} = 0.5$, $t^+_z = 0.05$, $t^-_z = 0.02$ and $t = 0.5$, which results in a qualitative concordance with the observed band structure of Fig. 4.6(a). Expanding the model to the DFT-fitted 26-band tight-binding model, we obtain Fig. 4.7(c), which also quantitatively resembles the ZrSiS bulk band structure.

If we now consider the cleaving along the (001) plane and introduce a surface to the situation described above, an asymmetry in the nonsymmorphic sublattices is introduced due to the displacement along the $\hat{z}$ axis that all nonsymmorphic symmetries have in common in ZrSiS. Since the nonsymmorphic symmetries are broken at the surface, the space group reduces to the spare wallpaper group $P4mm$ (SG 99). In this situation, only the crossings along $\overline{\Gamma}$-$\overline{\mathrm{X}}$ and $\overline{\Gamma}$-$\overline{\mathrm{M}}$ remain protected (green, yellow and blue dots in the surface BZ in Fig. 4.7(a)). The bulk Dirac ring reduces to surface Dirac points as $\bar{M}_z$ is broken. The surface mass term responsible for the gapping of the formerly degenerate bands can shift the surface bands into a region usually not occupied by the bulk bands, which will be identified as the floating surface bands.

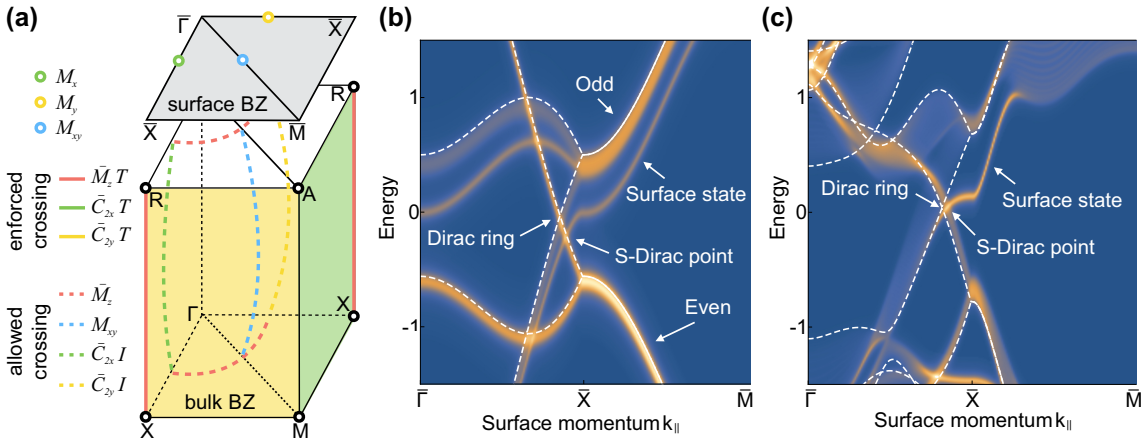

Figure 4.7: (a) Schemtic representation of the symmetries responsible for enforced or allowed crossings througout the BZ in space group *P4/nmm*. The nonsymmorphic symmetry, which is broken at the surface is enforcing all crossings at the border of the BZ. (b) Four-band tight-binding model showing the bulk (dashed white lines) and surface (color code) band structure along $\overline{\Gamma}$-$\overline{\mathrm{X}}$-$\overline{\mathrm{M}}$. The surface state is split off from the upper nonsymmorphically protected point at $\overline{\mathrm{X}}$. (c) The same with a DFT-fitted 26-band thight-binding model catching the ZrSiS band structure quantitively. Figure adapted from Ref. [3].

In the tight-binding model, this is achieved by including a surface potential at the top and bottom layer:

$$H^{\mathrm{surf}} = -0.1(\tau_0 + \tau_x)\sigma_+ \tag{4.5}$$

This term implicitly breaks the nonsymmorphic symmetry, which requires intraband hopping to be equal in the two sublattices. This imbalance between the local chemical potentials and hopping amplitudes between the two sublattices is expected from the modification in the crystal field at the surface. In our choice, we left the even orbital unaffected. The surface band structure is calculated according to Ref. [88], with a slab thickness of 20 unit cells, and presented as the color code in the Figs. 4.7(b) and (c). The bulk band degeneracy along $\overline{\mathrm{X}}$-$\overline{\mathrm{M}}$ corresponding to the odd orbitals is lifted, shifting one of the branches to lower initial state energies, which results in the appearance of the surface state.

If we consider the odd and even bands in Fig. 4.7(b) again and realize how one of them is no longer degenerate at the surface and responsible for the surface state, we could ask ourselves how this asymmetry is physically motivated. Since we can observe the same behavior in the DFT calculations of Fig. 4.6(b), where only the upper nonsymmorphically protected $\overline{\mathrm{X}}$ point at $E_{\mathrm{i}} \approx 0.75\,\mathrm{eV}$ is the origin of the surface state SS, we can conclude that it is not an artifact of our model but has physical meaning. The origin of the surface state in the upper degenerate point is even more obvious, if one follows SS away from the high-symmetry point and notices it merging with the bulk bands forming the nonsymmorphically protected crossing, while the lower degenerate point

at $E_i \approx -0.4\,\text{eV}$ remains completely unaffected by the surface. Even the surface state SS' is, if anything, originating from the even lower degeneracy at $E_i \approx -2\,\text{eV}$, which gives us all the more reason to solve this question.

To explain the selected sensibility of the nonsymmorphically protected points towards the introduction of a surface, let us consider the bulk bands in the DFT calculation again, presented in Fig. 4.8(a). So far, we were mainly focused on the orbital character of the surface states. But looking at the real space charge density of the bulk degenerate points at $\overline{\text{X}}$ in Fig. 4.8(b), the occupancy of the sulfur-p_z orbital is only relevant in the upper point. On the other hand, the lower degenerate point shows mainly sulfur-s character. The introduction of a surface (cleavage plane is shown as a dashed line in the middle of the unit cell) does not affect the lower crossing, since its electrons do not spacially extend into the surface area, which allows this Dirac point to retain its bulk symmetry. The p_z electrons occupying the upper nonsymmorphically protected point however feel the surface potential change, which explicitly breaks the symmetry protecting the degeneracy, leading to the floating, unpinned surface band.

After developing the theory explaining the surface states appearing in ZrSiS, we can now consider the effects disregarded so far. While SOC only plays a minor role in

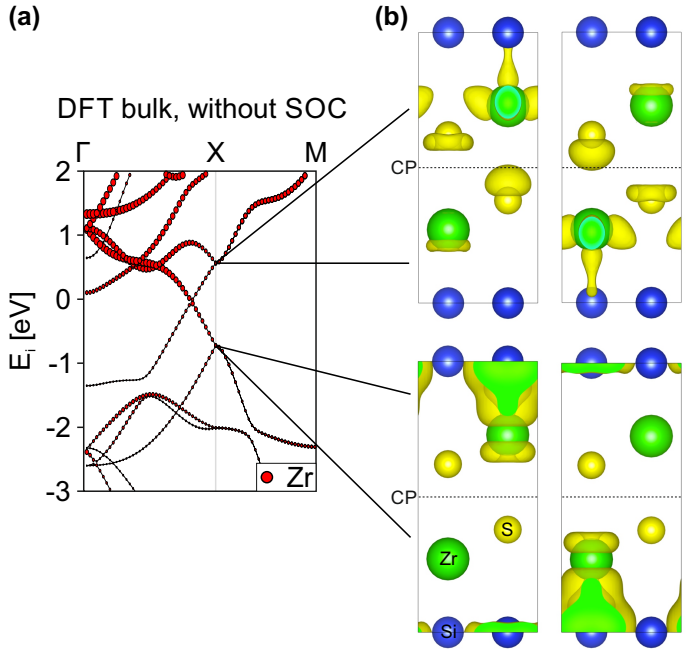

Figure 4.8: (a) DFT bulk band calculations of the band structure in ZrSiS. The size of the red circles correspond to the overall Zr orbital character, in contrast to the Zr character of the topmost unit cell presented in Fig. 4.6. (b) Isosurfaces of the bands forming the nonsymmorphically protected point at $\overline{\text{X}}$. The cleavage plane (CP) does only affect the upper degeneracy with p_z orbital character. Figure from Ref. [3].

ZrSiS, it is a factor in heavier members of SG 129. If we consider the surface also breaking inversion symmetry, we would expect the surface states to be spin-split in compounds with stronger SOC due to the Rashba effect. This was observed in HfSiS [89, 90] and results in singly degenerate surface bands, which will be further discussed in Sec. 6.2.

4.3.3 Alternative explanations

It is interesting to note that there are alternative explanations for the surface states appearing in members of SG 129. There have been theories, attributing the surface state to dangling bonds of the Zr atoms, which are weakly bound to the sulfur atoms of the next-nearest S layer above the cleavage plane [91]. This theory was developed on the isostructural compound ZrSnTe, but at least in ZrSiS there are no signs of dangling bonds, since hydrogenation over time, due to residual hydrogen in the chamber and, more obviously, potassium evaporation shown in Fig. 4.6(f) do not lead to the saturation of the surface state [92, 93], but merely to its gapping. Furthermore, this modification of the connectivity stands in contrast to the robustness of an explanation due to topological origins, which is hinted at as well [83, 91]. Lastly, it was proposed that the cleaving of a ZrSnTe crystal could lift up the last layer of the crystal and decouple a freestanding monolayer from the bulk [91]. This is supported by monolayer DFT calculations showing states around the X point in the area of the surface state. Nevertheless, slab calculations show a far better agreement with the experimental data. It is worth mentioning here that a slab calculation and a free standing monolayer describe two different situations, when it comes to the symmetries they break and conserve. It was shown above that a slab breaks all nonsymmorphic symmetries, as well as inversion symmetry. A monolayer on the other hand preserves these symmetries, resulting in a still four-fold degenerate X point, as has been explicitly shown by Guan et al. [94] on a monolayer of HfGeTe (also isostructural to ZrSiS). The two situations therefore describe a very different situation around the X point, where the surface states are most prominent. The appearance of bands in the monolayer calculation, in an energy range not occupied by bulk bands, is expected from a change in the hopping potentials, in which a slab and a monolayer calculation are very similar. The better agreement with slab calculations is, however, a clear indication for an explanation not relying on a freestanding monolayer. Outside of theoretical evidence, at least in ZrSiS, the brittleness of the crystals give a clear chemical argument against a monolayer lift-off.

4.3.4 Conclusion

In principle there are three basic requirements that need to be fulfilled to observe a floating surface state in a crystalline solid. Firstly, the space group needs to contain nonsymmorphic symmetry elements. This, in itself, is easily given in many materials, since 157 of the 230 space groups are nonsymmorphic. Secondly, the surface needs to break this nonsymmorphic symmetry and reduce the space group accordingly. And lastly, the bulk bands at the nonsymmorphically protected points in the BZ need to show a real space density of state extending into the cleavage plane, or in other words, the orbital character of the bands in question need to be sensitive to the introduction of a surface.

These conditions are very general and at least in SG 129 easily fulfilled. It is, therefore, very likely that this kind of surface state has already been observed in isostructural compounds of ZrSiS, e.g. ZrSiTe, CeSbTe and HfSiS [2, 5, 89]. It should however be mentioned here that at least in ZrSiTe, the surface state landscape is far more complicated than it is in ZrSiS. This will be discussed further in Sec. 5.2.

CHAPTER 5

ZrSiTe - Tuning the Nonsymmorphic Point to the Fermi Level[1]

Change is the essential process of all existence.

– MR. SPOCK

In the wake of the success ZrSiS had when it comes to its extensive potential applications, it makes sense to extend our search towards the complete structure type. As it was shown in the previous chapter, many of the interesting features in ZrSiS can not easily be observed in transport measurements, since they are located too far away from the Fermi level. Graphene, for example, would not have nearly been as successful, if it had not been for its linear crossings at the Fermi level that show almost no gapping due to the small atomic mass, and therefore SOC, of carbon. In this context, especially the nonsymmorphically protected crossings of SG 129 show great potential, intrinsically resisting a gapping by SOC.

By relating a structural property of SG 129 with the energy position of the nonsymmorphic degeneracy, it was possible to locate the crossing at the Fermi level in ZrSiTe, which will be discussed in Sec. 5.1. Similarly to ZrSiS, ZrSiTe shows a rich surface state electronic structure interfering with the bulk band properties, we are interested in. In contrast to ZrSiS, however, the larger SOC gaps the crossing between bulk and surface bands more obviously. This allows us to distinguish different branches of surface states, of which some can be explained similarly to the floating surface states of Sec. 4.3. Others, however, have topological origin and will be discussed in the context of drumhead surface states in Sec. 5.2.

[1] This chapter is based on publication [2]

5.1 Chemical strain effect on the electronic structure

If we start with the electronic structure of ZrSiS again, there are several possible ways to move the nonsymmorphic crossings at the X point, of which one is located above and one below E_F, to the Fermi level. Doping the crystal itself during the growth process would result in more or less available valence electrons, which would shift the Fermi level. The disadvantage of this method lies in the introduction of additional scattering centers in the otherwise homogeneous crystal structure, which could counteract the very reason we are trying to move the nonsymmorphic point to the Fermi level. On the other hand, uniaxial strain could shift the Fermi level to the point we require it to be. Fig. 5.1(a) presents the crystal structure of ZrSiTe, which emphasizes a fundamental property of the unit cell of compounds of the ZrSiS-like family: The size of the unit cell along the a and b axis is mostly defined by the square-net atoms, while the c axis distance is susceptible to changes in the Rocksalt-type layers. Since Te lies two periods

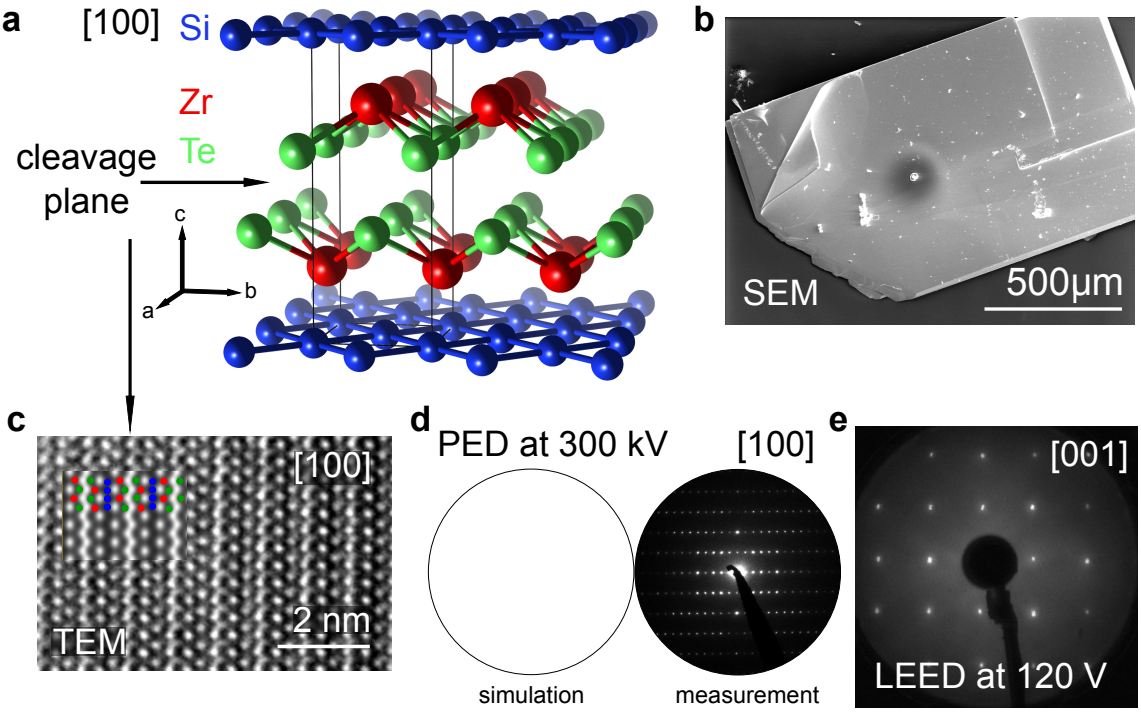

Figure 5.1: Crystal structure characterization of ZrSiTe. (a) Crystal structure with the cleavage plane marked by arrow between the Te layers. (b) SEM picture of a typical ZrSiTe crystal. (c) HRTEM graph showing the [100] direction. The focus plane is $\Delta f = -35$ nm. The inset shows the simulated image with the atoms marked in their corresponding colors. (d) PED patterns of the [100] direction. Simulation (white) and experiment (black) show a perfect agreement. (e) LEED pattern at 120 V showing the tretagonal lattice of the Γ points. Figure from Ref. [2].

higher in the periodic table than S, the unit cell is stretched along the c axis, while a and b stay relatively constant. Systematically replacing the sulfur atoms by elements of the same group has, therefore, physically the same effect as applying uniaxial strain to the ZrSiS unit cell. As can be seen in Fig. 5.1, such isostructural compounds grow relatively similar to ZrSiS, although it has to be noted here that ZrSiTe can already be cleaved by scotch tape, since the gap between the Te layers is also increased. For example, the SEM picture in Fig. 5.1(b) reveals an involuntary peeling of a thin layer just by the sample preparation procedure.

It is, therefore, not far-fetched to use the c/a ratio as a structural parameter to influence the position of the nonsymmorphically protected points. Finding such structural properties and relating them to the chemical or electronic properties of a material lies at the center of material science and has led to the understanding and prediction of many compounds [6, 48]. Fig. 5.2(a) shows the initial state energies of the two nonsymmorphic points for increasing uniaxial strain. While the gap is still very large for ZrSiS (# 8), it becomes smaller towards HfSiTe. The two lines connecting the points are a guide to the eye and do not indicate a fitting. For the c/a ratio of ZrSiTe, the upper nonsymmorphic degeneracy is accidentally located exactly at the Fermi level. For this reason, ZrSiTe became the second material studied during the course of this thesis. Fig. 5.2(b), (c) and (d) show the DFT calculations along Γ-X-M, getting more sophisticated starting without considering SOC, then considering SOC and ending with a slab calculation with SOC. Panel (b), where different irreducible representations are shown in different colors, clearly reveals the nodal line along Γ-X. As predicted, the upper nonsymmorphic point at X is accidentally located very close to the Fermi level. With SOC, shown in panel (c), the nodal line crossing is gapped, while the nonsymmorphic point at X stays protected and the degeneracy along X-M is again slightly lifted. The gap size in the nodal line is however considerably larger than it was in ZrSiS, which can be related to the larger atomic mass of Te. Lastly, the DFT slab calculation with SOC in panel (d) reveals surface-derived states that cross the bulk bands similarly to ZrSiS. Fig. 5.2(e) is showing the ARPES data measured along $\overline{\Gamma}$-$\overline{\mathrm{X}}$-$\overline{\mathrm{M}}$, which is a direct comparison to the slab calculations of panel (d). All the bands are perfectly resolved again, showing the surface bands with much higher intensity. It is prudent to note here that, while it was our goal to locate the nonsymmorphically protected degeneracy at the Fermi level, there are other bands, belonging to the nodal line or being part of the surface bands, crossing the Fermi level as well. This prevents the nonsymmorphic point from contributing considerably to transport measurements. One possibility to increase the 'cleanness' of the surrounding of the nonsymmorphic crossings will be presented in Sec. 6.2 and utilizes the gapping characteristic of SOC.

To identify the nonsymmorphic point and the course of the surface states better, panel (f) is showing the dispersion along $\overline{\Gamma}'$-$\overline{\mathrm{X}}$-$\overline{\Gamma}$. The bands leading to the nonsymmorphic points are superimposed with dashed lines and the upper bands meet slightly above the Fermi level, labeled 'NS'. This is most likely due to a slight hole doping of our sam-

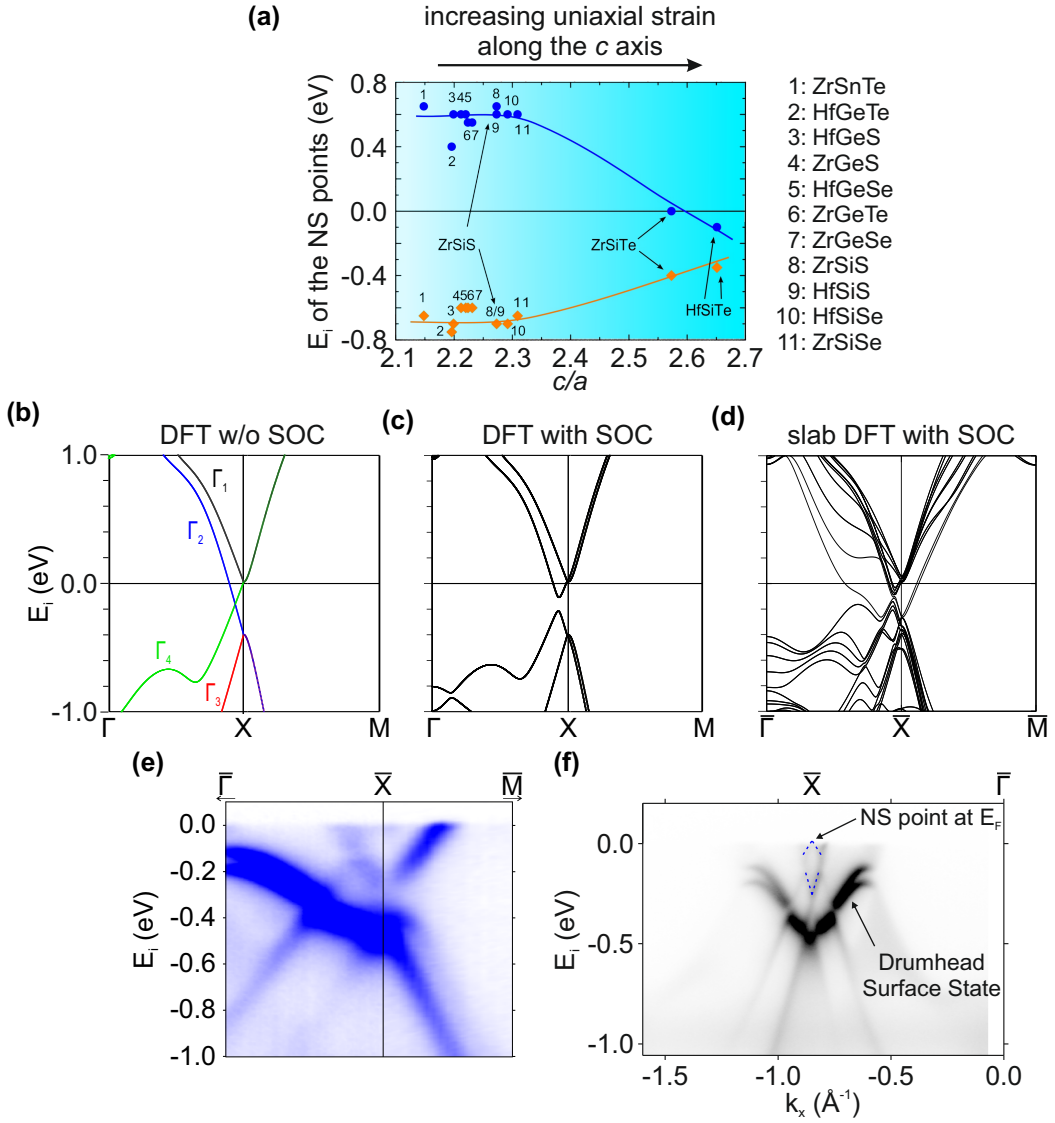

Figure 5.2: Band structure of ZrSiTe. (a) Inital state energies of the two nonsymmorphically protected degeneracies close to the Fermi level at the X point depending on the structural c/a ratio. For ZrSiTe, the c/a ratio is accidentially perfectly suited to locate the upper nonsymmorphic point at the Fermi level. (b) DFT calculation without considering SOC along Γ-X-M. Colors indicate different irreducible representations. (c) The same DFT calculation as in (b) but with SOC. The nodal line is gapped, while the nonsymmorphic point stays protected. (d) The same DFT calculation as in (c) but as a slab calculation. Additional surface-derived states appear alongside the bulk bands. (e) ARPES data along $\overline{\Gamma}$-$\overline{X}$-$\overline{M}$ taken with a photon energy of 30 eV. The slab calculation is reproduced perfectly with the surface states appearing as highly intense features. (f) ARPES data along $\overline{\Gamma}'$-$\overline{X}$-$\overline{\Gamma}$ taken with a photon energy of 39 eV. In the symmetrical representation, the upper nonsymmorphically protected point can be identified very close to the Fermi level. The outermost branch of the surface states is further labeled as 'drumhead surface state', further expanded in Sec. 5.2. Subfigures (a)-(e) are adapted from Ref. [2].

ple, since the effect was much stronger in earlier batches and continues to decrease with increasing sample quality. In this representation, it is also much more obvious that, due to the increase in SOC, the surface-derived states clearly gap where they cross the bulk bands. This allows us to identify three parts of the surface states around $\overline{\text{X}}$. In the following section, the outermost one, labeled 'drumhead surface state', will be further discussed.

Fig. 5.3 shows constant energy cuts of the dispersions shown in Fig. 5.2. Panels (a) and (b) were taken at $\hbar\omega$ = 100 eV and provide an overview over the first BZ, while panels (c) and (d) were taken at photon energies of 30 eV, resolving the band structure around the $\overline{\text{X}}$ point in more detail. The Fermi surface of panels (a) and (c) still show a slight extension of the bands at the $\overline{\text{X}}$ point, since the upper nonsymmorphic crossing point is located slightly above E_{F}, while the $\overline{\text{X}}$ point is clearly dot-like in the panels (b) and (d) showing the lower nonsymmorphic crossing point. Furthermore, the Fermi surface shows the two branches of the drumhead surface state (labeled in the panels (a) and (c)), which correspond to the surface state branch along the high-symmetry line identified in Fig. 5.2(f).

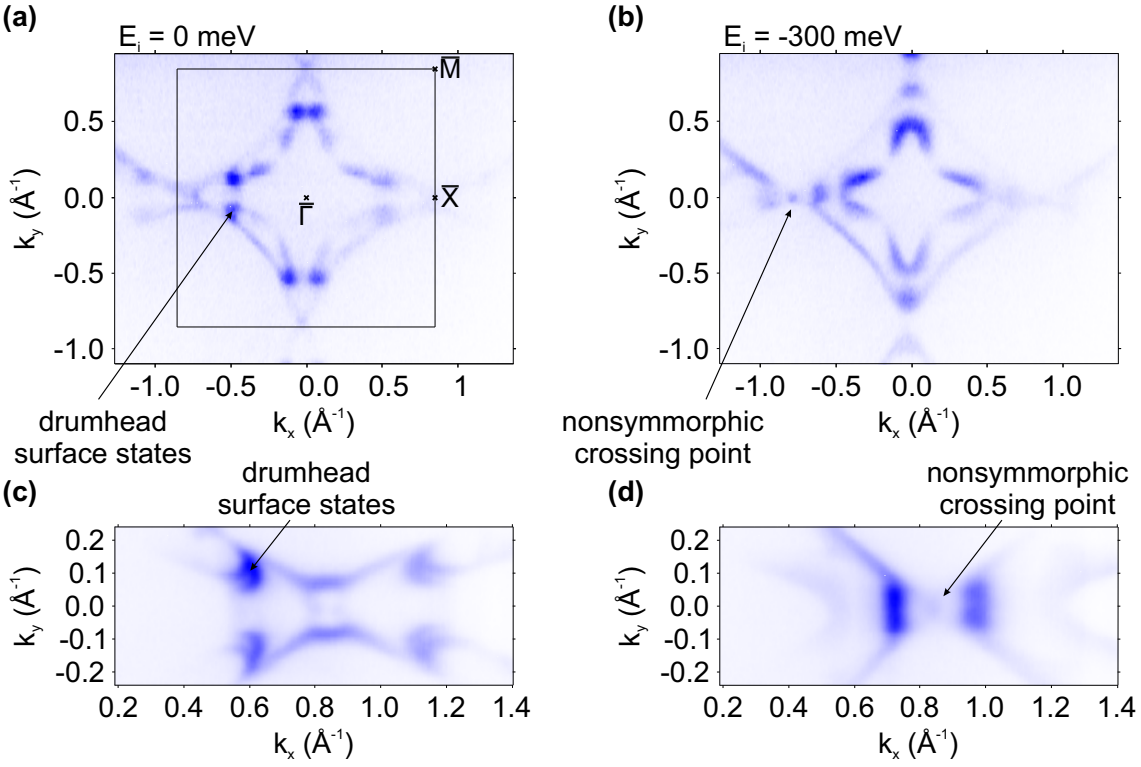

Figure 5.3: ARPES constant energy cuts of ZrSiTe. (a) and (b) were measured at $\hbar\omega$ = 100 eV and show and overview over the first BZ (black frame in (a)). (c) and (d) were measured at $\hbar\omega$ = 30 eV showing the surrounding of the $\overline{\text{X}}$ point. The lower nonsymmorphically protected degeneracy as well as the contribution of the drumhead surface states to the Fermi surface can be resolved and are labeled. Figure adapted from Ref. [2].

5.2 Drumhead surface states[2]

Based on the theoretical work of Chan et al. [46] and addressed in Sec. 2.1.5, a topological surface state is expected inside of the surface projection of a nodal line, if the crossing of the nodal line results in a change of the quantized Berry phase. In this case, the surface state is bound to the projection of the nodal line taking the form of a 2D drumhead and there is a direct connection between the stability of the nodal line and the surface state. As mentioned in the last section, we expect such a drumhead surface state to be present in ZrSiTe, which we consolidate by examining the surface projection of both the surface state and the nodal line and comparing the theoretically expected course of the surface state with the experimental ARPES data.

Fig. 5.4 illustrates the nodal line path through the BZ in ZrSiTe compared to ZrSiS. While the area enclosed by the nodal line in the $k_z = 0$ and $k_z = \pi$ plane is vastly different in ZrSiTe, they almost overlap in the surface projection of ZrSiS. It is however exactly in this overlap region, where the π Berry phase shift appears and the surface state should appear. This explains why we did not observe such a drumhead surface state in ZrSiS, since the overlap area is far too small compared to ZrSiTe. The Berry phase was calculated by the Wilson loop formalism enclosing the nodal line. Fig. 5.4 does however not consider the effect of SOC on the nodal line or the drumhead surface state. As we observed in Fig. 4.2(e) and 5.2(c), the nodal line is not protected against SOC and will gap; stronger in ZrSiTe due to the larger atomic mass of Te. The drumhead surface state is, in this case, expected to split into two branches, one connecting the lower part of the Dirac line node, and one connecting the upper one [46, 47].

It is fairly difficult to prove the expected origin of an observed surface state in practice. If the surface state is existing in the projected bulk band gap of an insulator, like in the case of the topological surface states of TIs, then they solely contribute to the transport properties of this material and allow for a distinction between bulk and surface characteristics. As we already saw in ZrSiS, this is not as easy, if we deal with a semimetal. From an ARPES point of view, there are certain properties and limitations we expect for a drumhead surface state. Fig. 5.5(a) shows the theoretical DFT surface projection of the surface-derived states between the Fermi level and -0.35 eV. The four cuts along and parallel to $\overline{\Gamma}$-$\overline{\mathrm{X}}$ are shown in panel (b), where cut 4 slices the outermost part of the drumhead contribution to the Fermi surface. The color code of the dispersion plot indicates the bulk band projection and surface character of the bands. The projection to the Fermi surface down to -0.35 meV in panel (a) was chosen, because the drumhead surface state (labeled 'DH') has its minimum there. Other surface-derived states are labeled as floating bands ('FB'), originating from the broken nonsymmorphic symmetry at the surface as presented in Sec. 4.3. Fig. 5.5(c) shows the corresponding ARPES

[2] This section is based on a publication soon to be submitted

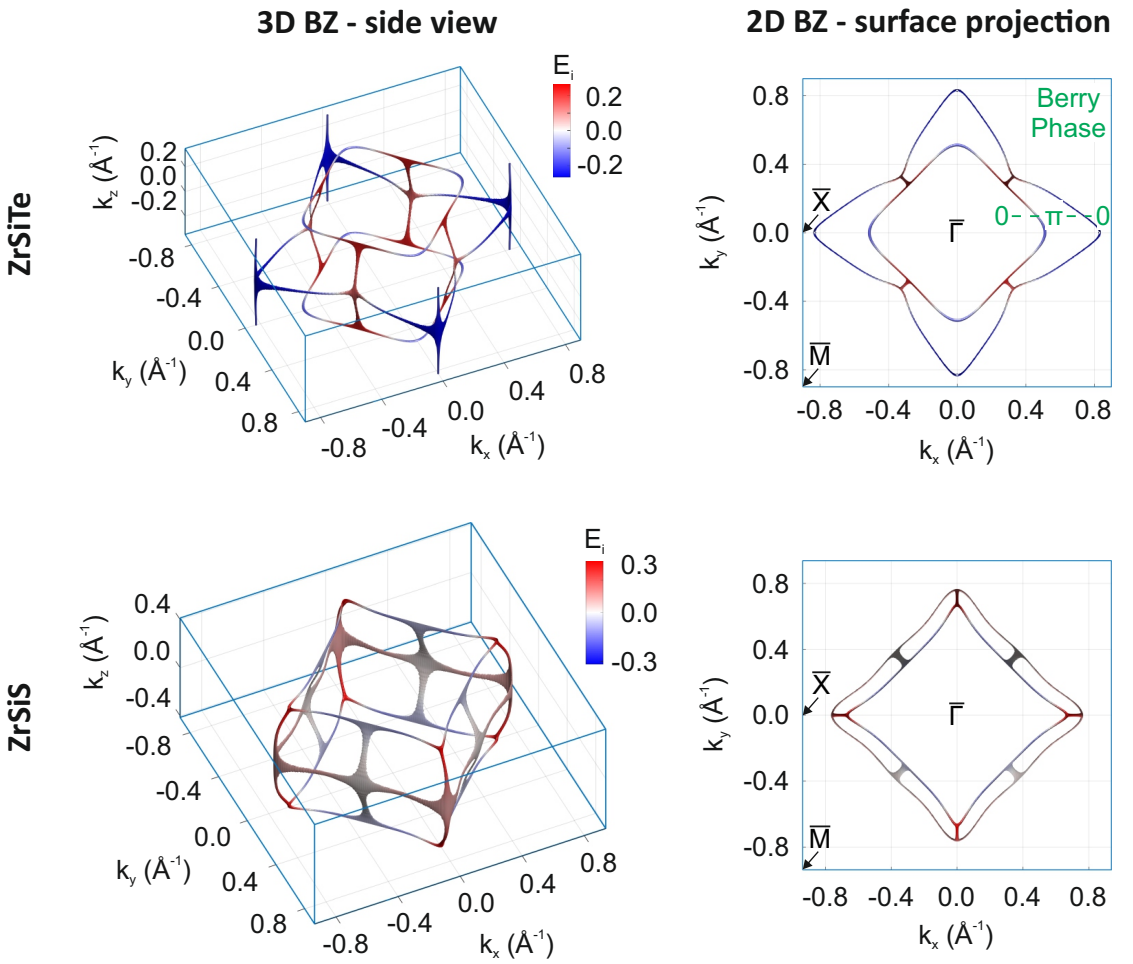

Figure 5.4: Nodal line comparison in ZrSiTe and ZrSiS without considering SOC. The nodal line is shown throughout the 3D BZ and in its 2D surface projection. The region enclosed by the $k_z = 0$ and $k_z = \pi$ plane nodal lines in the surface projection is characterized by a Berry phase shift of π, resulting in the occurrence of drumhead surface states in this area. This region is insignificant in ZrSiS.

Fermi surface. At a photon energy of 39 eV, only a small part of the BZ can be visualized at a time, wherefore the spectrum was centered around the $\overline{\text{X}}$ point. Panel (d) is showing the dispersion plots corresponding to the DFT band structures of (b). By changing the k_y values slowly from the high-symmetry line to negative values, we can observe the drumhead surface state dispersing monotonously between, and merging at its ends with, the surface projection of the nodal line. As described above, due to the significant SOC strength in ZrSiTe, the drumhead consists of two branches connecting the top and bottom part of the nodal line. The agreement in these surface bands, slowly dispersing up to the Fermi level and continuing above after cut 4, is remarkable. The floating bands, instead, show a very different behavior, dispersing much stronger in this area and disappearing above the Fermi level very rapidly.

The agreement is, however, not expected to be perfect. Since for a given photon en-

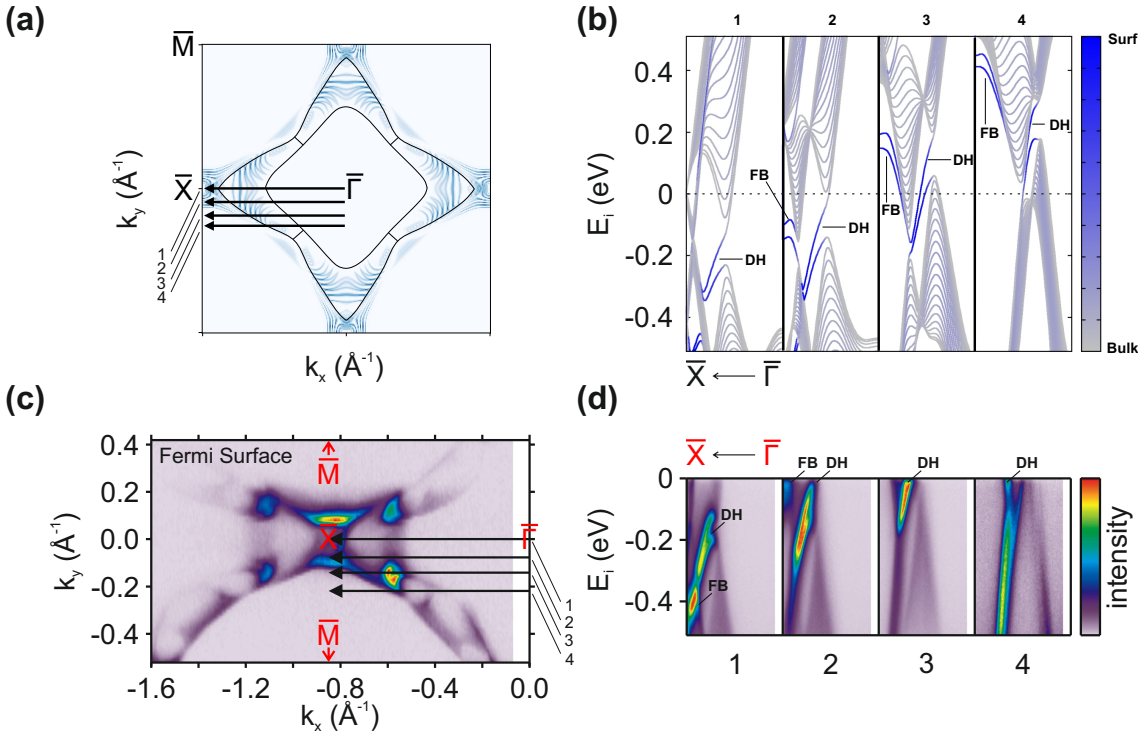

Figure 5.5: Dispersion of the drumhead surface state of ZrSiTe in DFT and ARPES. (a) Surface projection of a DFT slab calculation between 0 and −0.35 meV. The bulk nodal line projection is indicated in black. (b) Dispersion cuts along the arrows in (a). The drumhead surface states (DH) exists in between the nodal line projections, while other floating bands (FB) disperse much stronger. (c) ARPES Fermi surface measured at $\hbar\omega = 39$ eV. (d) Experimental dispersions corresponding to the arrows in (c). The unusual color scale was chosen to highlight the surface states, while simultaneously resolving the bulk band projections. This figure is part of a manuscript soon to be submitted.

ergy, the k_z value is fixed in the ARPES experiment, we do not observe the nodal line projection in as much detail in panel (d) as it is visible in (b). Furthermore, the cuts 1 to 4 show slightly different k_y values in the experiment, compared to the theoretical values: the theoretical values vary between 0 and $-0.2550\,\text{Å}^{-1}$, while they stay between 0 and $-0.2192\,\text{Å}^{-1}$ in the ARPES experiment. Again, this is not very surprising, since only very few materials show a perfect qualitative agreement with the slab calculations (in which ZrSiS was exceptional).

The most convincing argument for the topological drumhead nature of the surface states can be found in its surface projection of panel (a), since it exists exclusively in the theoretical projection of the nodal line (black line). In this projection it does not fill out the complete nodal line overlap area but only the area close to $\overline{\text{X}}$, which we attribute to the continued dispersion above the Fermi level, seen in panel (b). Of course, such a surface projection can not be seen in the experimental Fermi surface directly,

but would substantiate our presumption further.

For this reason, Fig. 5.6(a) shows the area the outermost surface state occupies for different constant energy cuts as well as the projection of these to the Fermi surface. Fig. 5.6(b) then compares the two projections of experimental data and theoretical data in black and green, respectively. They show qualitatively the same shape, down to the crescent-shape when the surface states continue above the Fermi level, and are both fully located inside of the nodal lines. Quantitatively, there is again an offset between the two projections, with the experimental data located closer to the $\overline{\text{X}}$ point and not extending as far into the BZ in k_y, as already observed in Fig. 5.5.

At the point of this thesis' submission, our analysis confirmed the theoretical prediction of drumhead surface states in ZrSiTe by ARPES experiments. To our knowledge, this is also the first time, such a topological drumhead surface state is limited by the interplay of two nodal lines with different k_z values and therefore existing only in the

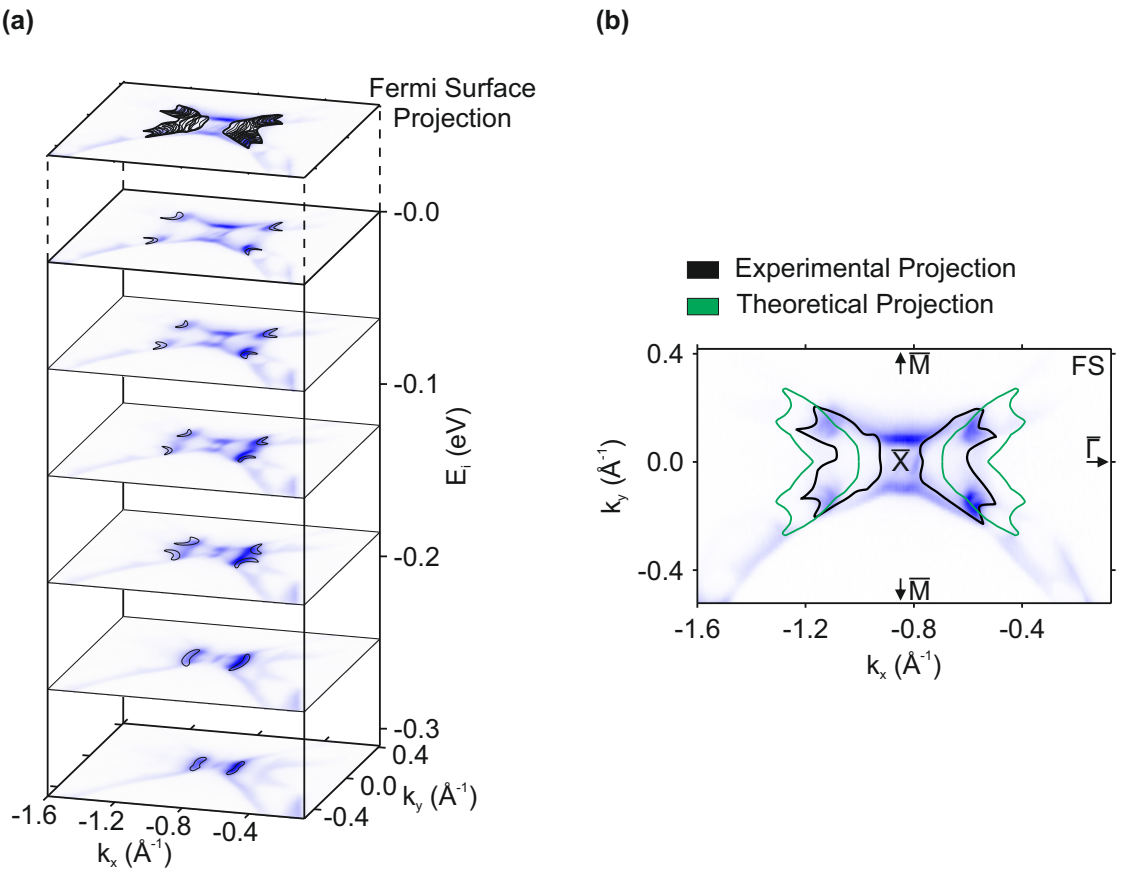

Figure 5.6: (a) Surface projections of the drumhead surface states in ZrSiTe for different constant energy cuts. (b) Comparison of the experimental and theoretical projection areas superimposed on the Fermi surface in black and green, respectively. While quantitatively differing, they qualitatively describe the same behavior inside of the nodal line. This figure is part of a manuscript soon to be submitted.

overlapping area.

CHAPTER 6

CeSbTe - Magnetic Order and Nonsymmorphic Symmetry[1]

There are four lights!

– CAPT. JEAN-LUC PICARD

We saw in the previous chapter that it is possible to tune the electronic properties of a material by selectively replacing elements, while keeping the space group symmetries. So far, we did not consider one fundamental property of the potential replacement atoms: their spin structure. By introducing f electron elements into the atomic structure of ZrSiS, we should in principle also be able to influence the magnetic properties of the system. In this chapter we consider the compound CeSbTe, with the lanthanide Ce carrying the magnetic moments. This allows for a multitude of magnetic phases ranging from the antiferromagnetic (AFM) ground state below the Néel temperature, over a fully polarized 'ferromagnetic' ('FM') phase for small magnetic fields, to a paramagnetic phase for high temperatures. As shown in Sec. 2.1.5, the breaking of time-reversal symmetry can lead to Weyl crossings with the corresponding Fermi arcs. But also the additional magnetic order of the AFM phase will influence the electronic structure. CeSbTe is therefore the first system that allows the tuning from a Dirac (paramagnetic phase), over a Weyl ('FM' phase), to a 'new Fermion' state (AFM phase) in combination with the nonsymmorphic symmetry of SG 129.

To this end, Sec. 6.1 introduces the measurements leading to the determination of the magnetic phase diagram. For the paramagnetic phase, ARPES measurements will be presented that underline the agreement between DFT and experiment. Since the

[1] This chapter is based on the publications [4, 5]

AFM phase is limited to very cold temperatures, Sec. 6.1.1 presents theoretical calculations of the electronic structure in this magnetic configuration that reveal a true eight-fold degeneracy displaying an exotic 'new Fermion' state [14]. Sec. 6.1.2 then describes the electronic structure of the 'FM' phase for magnetic fields above the transition field. Since magnetic fields would deflect any photoelectrons, this section is similarly limited to theoretical considerations. Lastly, Sec. 6.2 will deal with the effect of the greatly increased SOC in this compound compared to ZrSiS. Since the nonsymmorphic symmetry protects the crossings at high-symmetry points only when SOC is considered, and otherwise along complete high-symmetry planes, an increase in SOC can lead to a more isotropic, cone-like dispersion around the high-symmetry points.

6.1 Magnetic order in space group 129

Fig. 6.1 shows the refined neutron diffraction data of a CeSbTe powder sample at 5 K. The atomic structure for determining the red calculation, as well as a typical CeSbTe single crystal are shown as insets. This structure determination serves as a reference for the magnetic structure determination of the Figs. 6.2 and 6.3. Additional HRTEM images to underline the crystal structure, similarly to the ones for ZrSiS, can be found in the Supplementary Materials of Ref. [5].

By replacing Zr with Ce to allow for magnetic moments in the structure, we formally loose one electron in the valence bonding model, since the Ce $4f^1$ electron does not contribute to the hybridization and is only visible as a localized $4f$ band. It is for this reason that the square-net element Si is simultaneously replaced by an element of the fifth main group, Sb.

To identify the magnetic properties of CeSbTe, temperature-dependent magnetic susceptibility χ measurements were conducted for different strengths of the magnetizing field, H∥c, shown as different colors in Fig. 6.2(a). For a paramagnetic material, the susceptibility is expected to increase in a magnetic field with decreasing temperatures. For low fields, the susceptibility curve however shows a sharp cusp at the Néel temperature $T_N = 2.7$ K from where χ decreases to zero again. This is indicative for the formation of an AFM phase, compensating the spin polarization. For field strengths larger than 0.25 T, the cusp disappears again, which indicates the achievement of a fully polarized 'FM' phase, where the alignment field is strong enough to flip the anti-parallel spin layers. To figure out the easy axis, the magnetization can be plotted as a function of the magnetic field, which is shown in Fig. 6.2(b). The colors indicate varying temperatures, below and above the critical temperature T_N. For $T < T_N$ and a field H∥c, a critical field can be extracted with $\mu_0 H_c = 2.224$ T, where the magnetization shows a sharp increase. This signifies again the transition from AFM to 'FM'. In the case of

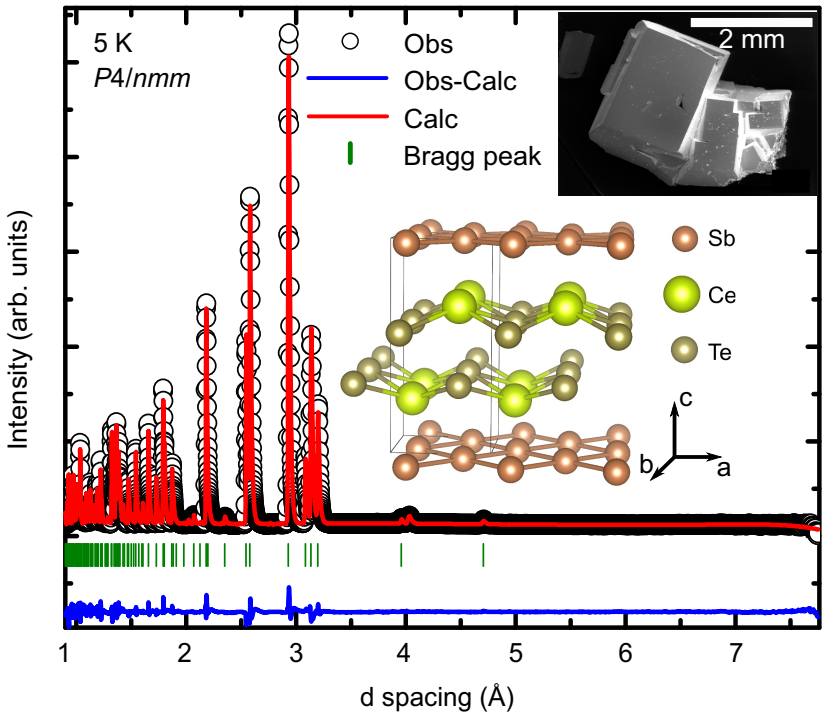

Figure 6.1: Refined neutron diffraction data fitted to the crystal structure of CeSbTe presented as inset next to a scanning electron microscopy image of a typical crystal. At 5 K the neutron data observe the paramagnetic case. Figure adapted from Ref. [5].

H⊥c, this field is far higher, roughly 1.75 T, which indicates that the spins prefer to align along the easy axis *c*. The transition perpendicular to *c* can then be explained by a spin-flop transition, while the far slower reached saturation moment indicates a strong magnetic anisotropy of the Ce moments. The specific heat measurements of Fig. 6.2(c) draw a similar picture, revealing a kink at $T_N = 2.7$ K in the temperature dependent specific heat that reduces with increasing field. The kink is furthermore shifted to slightly higher temperatures for fields above 1 T, which is reminiscent of ferromagnetic materials.

While it is quite obvious that in the fully polarized state, all spins align in parallel along the *c* axis, it is not definite what the AFM phase is composed of. Therefore, during this Ph.D. work, neutron powder diffraction measurements were performed on the low-field magnetic structure. Fig. 6.2(d) shows the AFM Bragg peaks at 1.5 K, below T_N, above its intensity difference to the paramagnetic reference at 5 K of Fig. 6.1. Most obviously, the experimental data show an additional peak marked by the arrow, which is visible as a strong peak in the difference plot. This is reminiscent of a doubling of the magnetic structure along the *c* axis. Hence, there are always two spins ordered in parallel before changing to two spins in antiparallel alignment to the *c* axis.

Implementing this spin structure, there are actually two possibilities for the parallel-

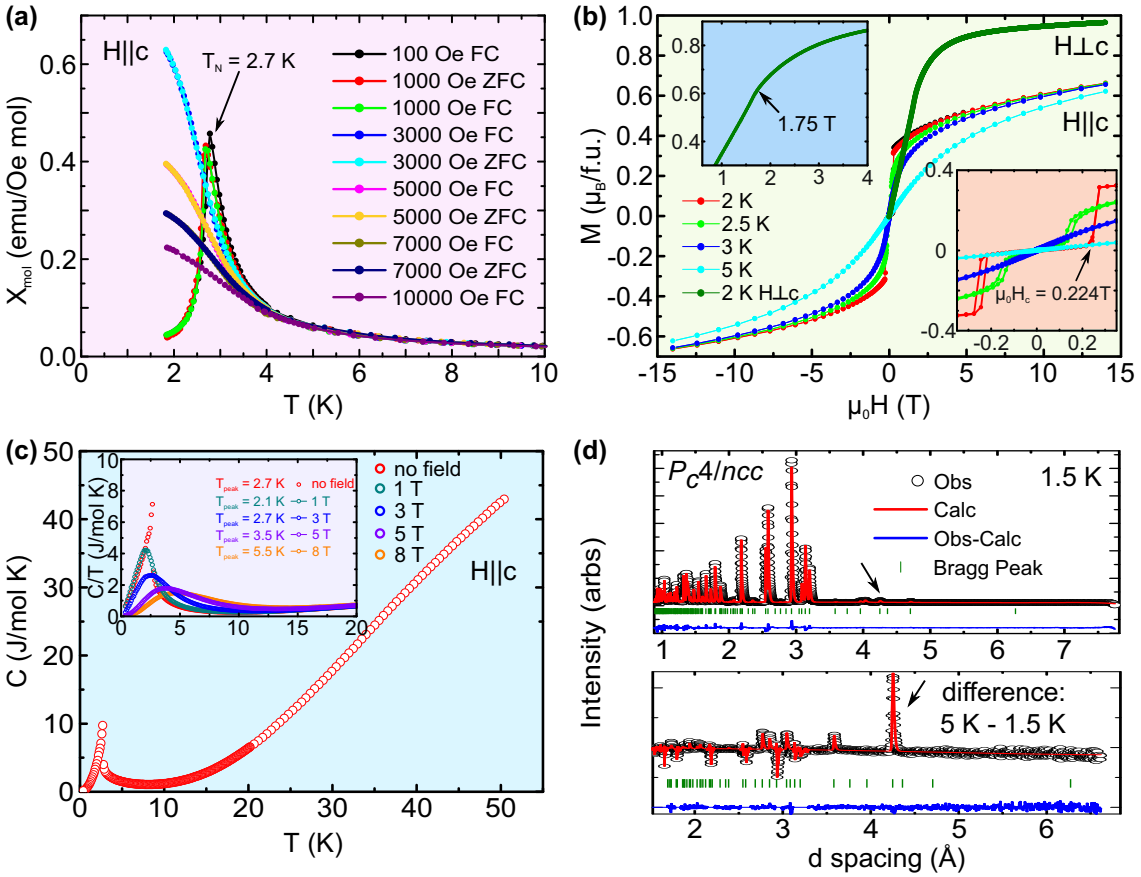

Figure 6.2: Magnetic property measurements of CeSbTe. (a) Temperature-dependent magnetic susceptibility measurements for different field strengths H (colors) applied along the c axis. (b) Field-dependent magnetization measurements for different temperatures and field directions (colors). Below T_N, CeSbTe undergoes a field-direction dependent phase transition. The saturation moment is reached faster for $H \parallel c$ than for $H \perp c$. (c) Temperature-dependent specific heat measurements for different fields $H \parallel c$ (colors). (d) Refined neutron diffraction data showing data at 1.5 K and the difference towards data from Fig. 6.1 at 5 K. Besides small changes in the unit cell parameters, which are responsible for the changes in the background, one main magnetic Bragg peak is visible (arrow) indicating a doubling of the unit cell along the easy c axis in the AFM phase. Figure adapted from Ref. [5].

antiparallel transition plane. Either the spins flip between the Te layers (the cleaving plane), or they flip at the Sb square net. Both situations are shown in Fig. 6.3(b) and (d), next to their best neutron data fits in (a) and (c). Both AFM structures belong to the magnetic space group P_c4/ncc (no. 130), but correspond to different irreducible representations when it comes to their origin (they differ by a shift of half a unit cell in c). From the fits to the neutron data, the structure could be solved to belong to mZ_1^+ with the origin at (000), which is the situation of a spin flip between the Te layers shown in Fig. 6.3(a) and (b). This red fit curve is also superimposed on the data of Fig. 6.2(d).

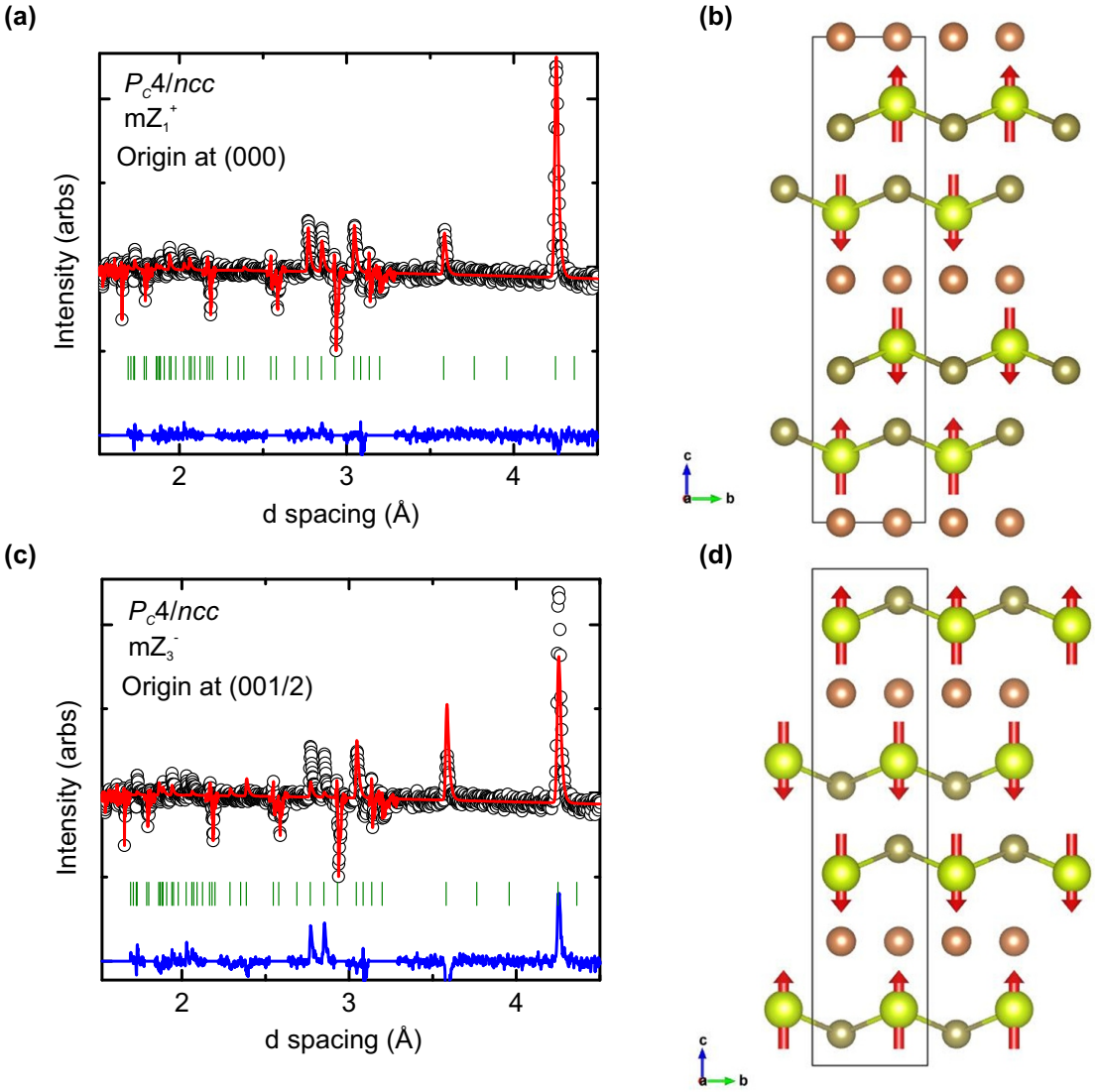

Figure 6.3: (a) Difference in the refined neutron diffraction data of 5 K and 1.5 K. The experimental data is fitted in red to the magnetic structure of (b) showing a doubling of the unit cell along *c* and a switching of the magnetic moments between the Te layers. (c) and (d) The same as (a) and (b) with a switching of the magnetic moments between the Sb square net. The refinement fitting shows a clear indication of the AFM structure of (b). Figure adapted from the SI of Ref. [5].

From the measurements of the magnetic properties of CeSbTe and the structure determination by neutron diffraction, we can derive the following magnetic phase diagram (Fig. 6.4). At temperatures higher than $T_N = 2.7$ K, CeSbTe is a paramagnetic material, with the magnetic moments of the Ce atoms ordered randomly. As expected, for a strong enough external field, the moments align along the field direction (with the easy axis being the *c* axis) and CeSbTe undergoes a transition into the fully polarized 'FM' phase. The ground state, for $T < T_N$ and small fields, however is the AFM phase with

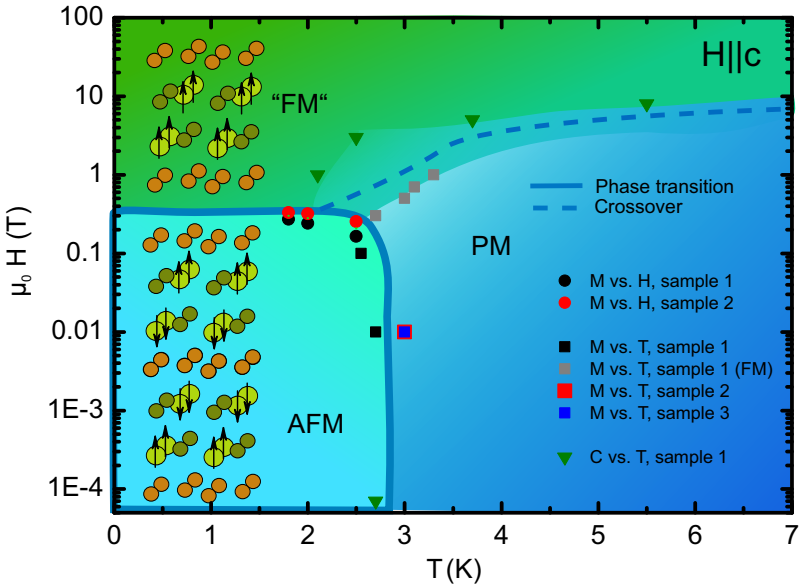

Figure 6.4: Magnetic phase diagram of CeSbTe, showing the measured edges of the phases as data points. The ground state consists of a AFM phase with a magnetic unit cell doubling along c. Above T_N, CeSbTe transitions into a paramagnetic (PM) phase, which can be polarized for relatively low field strengths $H \parallel c$ allowing for a crossover into the fully polarized ('FM') phase. Figure from Ref. [5].

a doubling of the unit cell along c. This makes CeSbTe a system able to realize many different exotic and even topological states, by influencing the addition and breaking of specific symmetries in one material through the many magnetic phases it exhibits (presented in the following Secs. 6.1.1 and 6.1.2).

While it is difficult to measure the AFM and 'FM' phases with ARPES due to the very cold temperatures and necessary magnetic fields, respectively, it is possible to measure the electronic structure of the paramagnetic phase and verify the theoretical predictions made by DFT. Fig. 6.5(a) shows the Fermi surface of CeSbTe at $\hbar\omega = 70$ eV measured at room temperature, which ensures that we are far away from the phase transition. It shows the typical diamond-shaped nodal-line feature, characteristic for SG 129. The k_z dispersion is here much more pronounced than it was the case for ZrSiS or ZrSiTe, which can be seen in the dispersion, for example, along $\overline{\text{X}}$-$\overline{\Gamma}$-$\overline{\text{X}}$ (purple line in panel (a)), shown in Fig. 6.5(b). The theoretical DFT $k_z = 0$ (Γ-X-Γ) and $k_z = \pi$ (Z-R-Z) dispersions along this direction draw a very different picture, which are opposed to the experimental data with a similar energy axis in Fig. 6.5(c). It would be preferably to extract the photon energy corresponding to a high-symmetry plane by performing a photon energy dependent study. In absence of such a time intensive study, we can instead use the nonsymmorphically protected point at X and R, which have very distinct initial state energies, to determine the approximate k_z value for the experimental ARPES spectra at the measured photon energy of $\hbar\omega = 70$ eV. Since identifying the exact

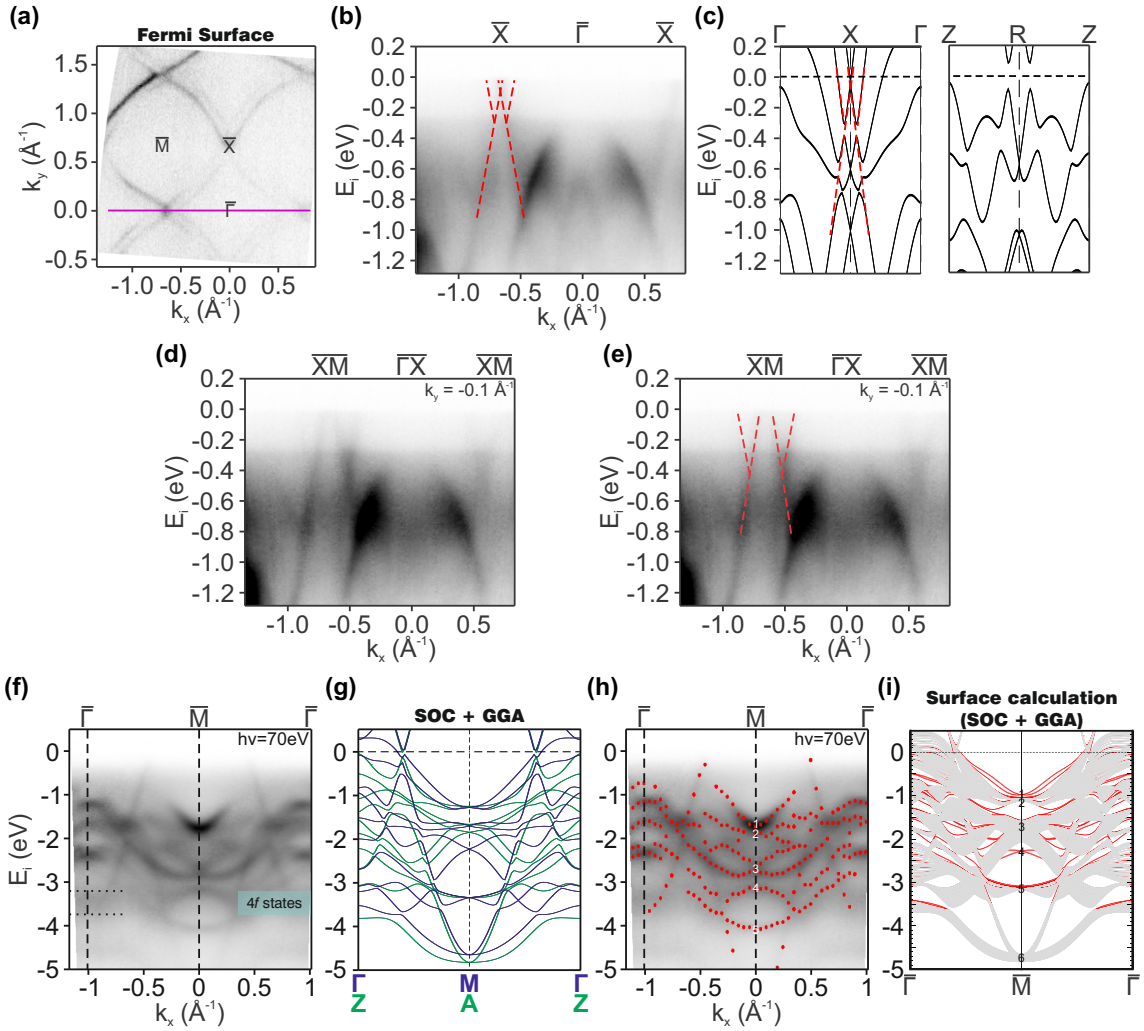

Figure 6.5: ARPES data taken at $\hbar\omega = 70\,\text{eV}$ and DFT calculations of CeSbTe. (a) Fermi surface showing the typical diamond-like feature surounding the $\overline{\Gamma}$ points. The high-symmetry points of the first BZ are labeled. (b) Dispersion along $\overline{\text{X}}$-$\overline{\Gamma}$-$\overline{\text{X}}$ (purple line in (a)). (c) Bulk DFT calculations along the same k vector of (b) for $k_z = 0$ and π. The position of the nonsymmorphically protected point close to the Fermi level at $\overline{\text{X}}$ is indicated by the red dashed lines in (b) and the $k_z = 0$ data of (c). (d), (e) Dispersion parallel to the path shown in (b), along $k_y = -0.1\,\text{Å}^{-1}$ revealing the bands leading to the nonsymmorphic crossings in (b). (f) Dispersion along $\overline{\Gamma}$-$\overline{\text{M}}$-$\overline{\Gamma}$, revealing the nondispersive Ce $4f^1$ band at $E_\text{i} = -3.1\,\text{eV}$. (g) Superposition of the $k_z = 0$ (blue) and $k_z = \pi$ (green) plane DFT bulk calculations along the k vector of (f). (h) Tracing of the visible experimental band structure of (f) shown by the red dots. Band crossings at $\overline{\text{M}}$ are enumerated. (i) DFT slab calculation along the same path. Except for a difference in the energy axis scaling, the experimental band structure is perfectly reproduced. Additional surface-dericed bands are shown in red. Figure adapted from Ref. [5] and its SI.

experimental band dispersion close to the Fermi level in Fig. 6.5(b) proved to be difficult, due to the special symmetry properties of the high-symmetry line and hence the great reduction in intensity due to matrix element effects, we instead follow the bands in the dispersion plot slightly off the high-symmetry line. Fig 6.5(d) and (e) show a parallel dispersion path to the purple line in (a), with $k_y = -0.1\,\text{Å}^{-1}$. The bands indicated by the dashed red lines in (e) are much more pronounced here, which allows us to follow them to the crossing point in Fig 6.5(b), marked in dashed red lines as well. Comparing the energy of this degeneracy to the DFT data in Fig. 6.5(c), only the X point reveals a linear dispersion leading to a crossing point close to the Fermi level (similarly indicated by the red dashed lines). We can, therefore, conclude that the $\hbar\omega = 70\,\text{eV}$ data is represented fairly well by the $k_z = 0$ plane.

Since slab calculations proved to be very reliable in the electronic structure determination of ZrSiS and ZrSiTe in the previous chapters, we will compare the ARPES dispersion along $\overline{\Gamma}$-$\overline{\text{M}}$-$\overline{\Gamma}$ in Fig. 6.5(f) with its theoretical slab counterpart. This has the further advantage of showing additional surface-derived states. To get an initial idea, about the slab calculation appearance, we can plot the superposition of the $k_z = 0$ (Γ-M-Γ) and the $k_z = \pi$ (Z-A-Z) direction, presented in Fig. 6.5(g). This reveals the k_z dispersion to be far less pronounced at the $\overline{\text{M}}$ point than it would be for a similar plot containing $\overline{\text{X}}$, apparent from panel (c). This makes it easier to compare the slab calculation with the ARPES data along a path that contains $\overline{\text{M}}$. For completeness purposes, the superposition and slab calculation along $\overline{\text{X}}$-$\overline{\text{M}}$-$\overline{\text{X}}$ can be seen in Fig. 6.8 of Sec. 6.2. Fig. 6.5(h) and (i) show the traced experimental band structure (red dots) next to the slab calculation along the same path and energy. Additional surface-derived bands, appearing in an area not confined by the bulk bands of Fig. 6.5(g), are shown in red and most likely result from the loss of nonsymmorphic symmetry at the surface (cf. the floating surface state theory of Sec. 4.3). The identified band crossings of surface and bulk bands at $\overline{\text{M}}$ are numbered. The agreement between ARPES and slab calculations is remarkable, showing only a consistent deviation in the energy axis for lower initial state energies. The lowest degenerate point (number 6) is, for example, clearly visible in the slab calculations, while the bands in ARPES will only meet below -5 eV, outside of the measured energy range. This can be attributed to the increasing inaccuracy of DFT far away from the Fermi level, which only allows for a qualitative agreement with ARPES here.

Furthermore, starting at around -3.1 eV initial state energy, we observe a flat, nondispersive band, which can be attributed to the localized Ce $4f^1$ band. These bands are treated like core states in the DFT of the paramagnetic material, but their exact position is important for the magnetic DFT calculations shown later. The energy position of the $4f$ band agrees with photoemission data on CeTe and CeBi [95] and is further supported by the magnetization data of Fig. 6.2(b), clearly indicating one localized f electron per Ce atom.

6.1.1 Antiferromagnetism and higher order crossings

After introducing the AFM ground state of CeSbTe, it is interesting to discuss its contribution to the realization of novel states of matter. While Dirac and Weyl phases were discussed in Sec. 2.1.5 already and attributed to their four- and two-fold band crossings, the additional magnetic symmetry of the AFM phase in combination with the nonsymmorphic symmetries allows for the realization of quasi-particles beyond Dirac and Weyl fermions [14].

The AFM phase formally breaks TRS, but simultaneously introduces a new symmetry to the Schrödinger Hamiltonian in the form of the AFM ordering, here a doubling of the unit cell along the c axis. In CeSbTe, the symmetry element $\{\bar{1}|(0,0,\frac{1}{2})\}$ squares to -1 and therefore maps k to $-k$, as would TRS do in space group no. 130. Hence, the AFM phase of CeSbTe, although crystallizing in SG 129, behaves as belonging to SG 130 with TRS. This has a profound influence on the band structure, since it causes the bands to still be four-fold degenerate at X, M and R, but allows for eight-fold degenerate points at A. Fig. 6.6 shows DFT calculations of the AFM phase in CeSbTe. Two different crossings at A are magnified and the lower one at $E_i = -4.6\,\text{eV}$ shows a true eight-fold crossing.

To experimentally observe this crossing now, it would be necessary to perform the experiment at very cold temperatures $T < 2.7\,\text{K}$, as for example possible in the 1^3 experiment at the BESSY 2 synchrotron. A careful photon energy dependent study around the $\overline{\text{M}}$ point could resolve the A point (since the M point does not show such a degeneracy), but since we are not able to count the bands at this point in ARPES, we would always be forced to rely on DFT to verify our observation of an eight-fold degeneracy.

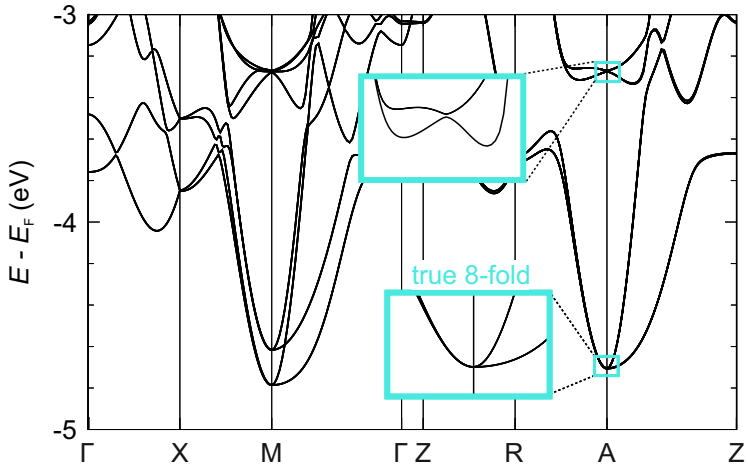

Figure 6.6: DFT calculations of the AFM phase in CeSbTe. At $E_i = -4.6\,\text{eV}$, a true eight-fold degenerate point can be realized at the A point. Figure adapted from Ref. [5].

6.1.2 'Ferromagnetism' and Weyl physics

If a strong enough field is applied, whose strength depends on the temperature and field orientation, the fully polarized 'FM' phase can be reached. While the combination of time-reversal symmetry $\mathcal{T}$ and spacial-inversion symmetry $\mathcal{I}$ enforced all bands to be at least two-fold spin degenerate in the paramagnetic phase, the breaking of $\mathcal{T}$ in the 'FM' phase removes this necessity. The direction of the magnetic field is, however, very important when it comes to, by other symmetries enforced, crossings in the band structure. Fig. 6.7(a) shows the DFT calculated bulk band structure of the paramagnetic phase as a reference. We will in the following consider two four-fold crossings in this phase and observe their change depending on the field direction. The green box marks the position of the nonsymmorphically protected degeneracy at the X point, which is additionally protected by the anti-unitary combination of $\mathcal{T}$ and the screw axis $\bar{C}_{2x}$. The orange box highlights a crossing along Γ-Z, which is protected by the four-fold rotation symmetry of SG 129. Together with $(\mathcal{TI})^2 = -1$ both these cases result in four-fold crossings, even with the addition of SOC.

If now a magnetic field is applied, time-reversal symmetry is no longer preserved. In

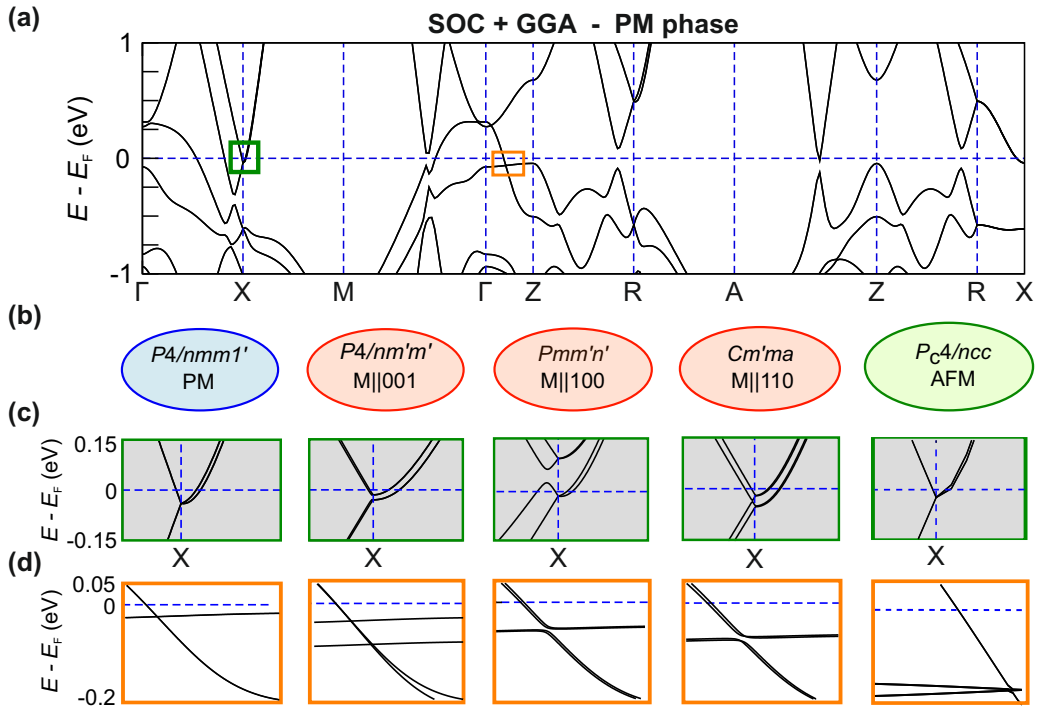

Figure 6.7: DFT calculations of the band structure for different magnetic phases of CeSbTe. (a) Paramagnetic bulk band DFT calculations with SOC. (b) Some of the magnetic phases possible in CeSbTe. (c) Nonsymmorphic crossing at X (green). (d) Crossing along Γ-Z, protected by the four-fold rotation symmetry (orange). The different cases belong to the labeles in (b). Figure adapted from Ref. [5].

the case of a temperature $T < 2.7\,\mathrm{K}$ and a field applied along the [001] direction with $\mu_0 H_c > 0.224\,\mathrm{T}$, this does lift the spin degeneracy of all bands involved. The combination of nonsymmorphic and TRS $\bar{C}_{2x}\mathcal{T}$ is, however, still enforcing a degeneracy at X and the rotational axis is still enforcing one along Γ-Z, which splits the four-fold degeneracy into two two-fold crossings. This is shown in Fig. 6.7(b), (c) and (d) in the $M \parallel 100$ case. In contrast, a field along [100], which is analogous to a field along [010] in a tetragonal space group, breaks the rotational symmetry and only leaves the nonsymmorphic degeneracy protected. An equivalent point can be made for a field direction along [110]. Note that a much larger field ($\mu_0 H > 2\,\mathrm{T}$) is required to align the spins in a direction perpendicular to the easy axis.

It is therefore possible to realize two-fold degenerate points in CeSbTe, which should in principle result in Fermi arcs expected from Weyl physics, even if it is not possible to measure ARPES in a magnetic fields.

6.2 The effect of spin-orbit coupling in space group 129

If we consider the evolution of the band structure, coming from ZrSiS in Chap. 4, continuing with ZrSiTe in Chap. 5 and ending with CeSbTe in this chapter, we notice a steady increase in the atomic mass of the involved elements and the strength of SOC, accordingly. Usually, SOC is related to the increase in gap sizes in bands with forbidden crossings. From this perspective, it is more of a disturbing force in the design of electronic properties sought to minimize, since it is related to the prevention of linear crossings and the increase in parabolic dispersion. As nonsymmorphic symmetries are protected against a gapping at the high-symmetry points, but SOC retains its full effect on the degeneracies along the high-symmetry lines, SOC can be used to create much more isotropic Dirac cones in SG 129.

To emphasize this point, Fig. 6.8 compares the electronic structures of ZrSiS, a material with negligible SOC, and CeSbTe, a compound of sizable SOC strength. If we consider a similarly linear dispersion of the bands, coming from $\overline{\Gamma}$ and forced to meet at $\overline{\mathrm{X}}$, but remember that along the border of the BZ, along $\overline{\mathrm{X}}$-$\overline{\mathrm{M}}$, the nonsymmorphic protection is only extended without SOC, we can observe two majorly different courses of the bands in the surface BZ (schematically shown and exaggerated in Fig. 6.8(a) and (e)). Only in CeSbTe, a real 2D Dirac cone is formed, while in ZrSiS this 'cone' is very anisotropic, only crossing linearly perpendicular to $\overline{\mathrm{X}}$-$\overline{\mathrm{M}}$. Since the second derivative of the band dispersion is linked to the mass of the quasi-particles, we favor the situation shown in (e), which is independent of the $k_\parallel$ vector direction. This counter-intuitive advantage of SOC in nonsymmorphic space groups is, of course, not as pronounced in the experimental spectra of the two materials, shown in Fig. 6.8(b) and (f). To evaluate the effect

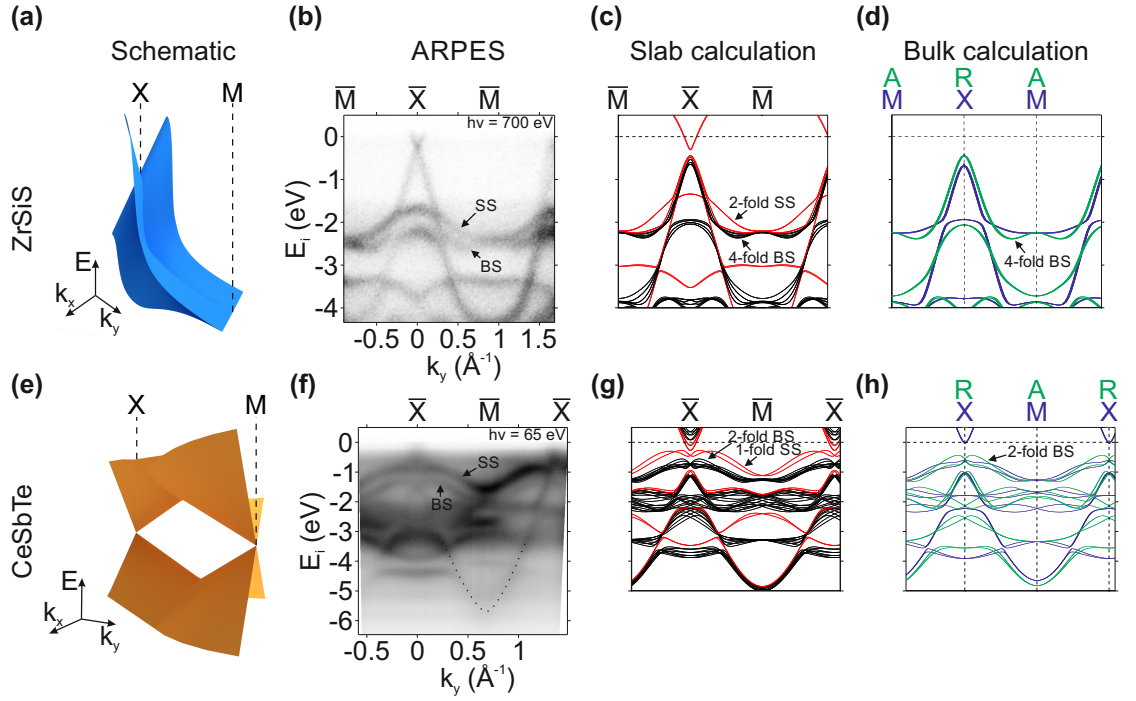

Figure 6.8: Comparison of the effect of SOC on ZrSiS and CeSbTe. (a) and (e) Schematics of the degree of anisotropy. (b) and (f) ARPES data measured along $\overline{\text{X}}$-$\overline{\text{M}}$ at $\hbar\omega = 700\,\text{eV}$ and 65 eV, respectively. (c) and (g) DFT slab calculations of the path shown in (b) and (f), respectively. The order of degeneracies is labeled in the bulk (BS) and surface states (SS). Surface-derived states are shown in red. (d) and (h) Bulk DFT calculations of the path shown in (b) and (f), respectively. The $k_z = 0$ (M-X-M) plane is shown in blue, while $k_z = \pi$ (A-R-A) is displayed in green. Figure adapted from Ref. [4].

of SOC in the bulk and surface bands, slab calculations along the same directions are shown in Fig. 6.8(c) and (g). The bands labeled 'BS' (bulk state) and 'SS' (surface state, shown in red) are identified by comparing the slab calculations with the bulk band calculations of (d) and (h), which show the $k_z = 0$ (M-X-M) and $k_z = \pi$ (A-R-A) plane in blue and green, respectively. The first distinction in the bulk bands can most easily be seen in ZrSiS (panel (d)), where we know all bands are four-fold degenerate at the high-symmetry points. Since the bands do neither split along X-M, nor R-A, we can conclude that they stay four-fold, since SOC is too weak to lift the degeneracy. In CeSbTe (in (h)) on the other hand, the bands split along X-M (R-A, respectively) and only meet at the high-symmetry points. The bulk bands are therefore only two-fold spin-degenerate. As described in Sec. 4.3, the surface does no longer preserve the nonsymmorphic symmetry, and the surface bands in Fig. 6.8(c) are therefore only two-fold degenerate at the high-symmetry points and lines, accordingly. Since the surface also breaks inversion symmetry and, together with a sizable SOC, the spin-splitting is lifted apart from the time-reversal invariant momenta, the CeSbTe surface bands in panel (g) are singly degenerate along $\overline{\text{X}}$-$\overline{\text{M}}$. The theoretical band dispersions are perfectly matched by the

ARPES data in Fig. 6.8(b) and (f), aside from the usual discrepancy in the energy axis, although, the ARPES data do not allow us to count the degree of degeneracy of each band observed. Furthermore, the splitting of the surface bands is still too weak to be reliably observed, although the surface band is clearly too broad to contain only a single band.

It is, therefore, in principle possible to decrease the anisotropy of the nonsymmorphically protected Dirac cones by increasing the SOC in the material. The increase in gap sizes at accidental, non-protected crossings, should in principle also allow for cleaner crossings at the high-symmetry points. While the effect is visible in CeSbTe, it is still not strong enough to significantly gap the bands. Hence, these results only indicate a possible direction to increase the electronic properties of nonsymmorphic materials, and SG 129 in particular.

CHAPTER 7

$LaCuSb_2$ - Space Group 129 and Superconductivity[1]

It took us 15 years and three supercomputers to MacGyver a system for the gate on Earth.

– CAPT. SAMANTHA CARTER

In the context of topology, there has been increased interest in topological quantum computing in recent years [10]. Quantum computers employ qubits nowadays, instead of the bit structure used in classical computers, to store information. Algorithms operating on qubits utilize the intrinsic quantum mechanical properties of these states, which allows quantum computers to be much more efficient at certain problems, like quantum simulations, or improve existing limitations of classical systems, like in the case of quantum-based cryptography. One of the biggest limitations in the field of quantum computing so far is the decoherence of the prepared quantum states that need to be carefully decoupled from their environment to allow for quantum gates to operate on them faster than their decoherence time. Though it is in principle possible to simulate ideal quantum circuits, by performing operations on imperfect ones as long as the error rate is below a certain threshold [96], the field of topological quantum computing approached this problem by implementing fault tolerance on a hardware level. The robustness of topologically protected states against localized imperfections plays a major role in the implementation of fault-tolerant Majorana fermions as anyons obeying non-Abelian statistics [97]. Such non-Abelian Majorana particles can be realized in vortices of topological superconductors, a state of matter, where superconductivity is induced in the topological phase via the proximity-effect. Such a

[1] This chapter is based on a publication soon to be submitted

topological superconducting phase can either be achieved by bringing a strong topological insulator very close to an *s*-wave superconductor [98], or by utilizing the bulk superconductivity of certain topological 3D semimetals directly, which is the way we aim to achieve here.

We already showed in previous chapters that some members of space group 129 show a non-trivial Berry phase and how this could lead to topological surface states, e.g. on the surface of ZrSiTe. So far, these semimetals were not analyzed in the context of their superconducting properties. Here, we focus on $LaCuSb_2$, another member of SG 129, which shares the square-net motive, but is not isostructural to ZrSiS. Its crystal structure and electronic properties are presented in Sec. 7.1, while Sec. 7.2 introduces its topological features and emphasizes the potential of $LaCuSb_2$ as a material at the interface between topology and superconductivity.

7.1 Electronic structure determination

As mentioned above, $LaCuSb_2$ is not isostructural to ZrSiS, but still belongs to the same space group *P*4/*nmm* (no. 129). This implies, it exhibits the same symmetries, but not necessarily the same atomic basis. Fig. 7.1(a) and (b) show a side and top view of the crystal structure of $LaCuSb_2$, respectively. The unit cell is shown in black. Since it features the same square net of Sb atoms as CeSbTe (cf. Fig. 6.1) and, as we showed earlier in Sec. 2.2, it is responsible for many of the properties leading to a Dirac semimetallic nature, we would expect a recognition of the electronic features in the band structure as well. This should, to first order, be independent of the additional Sb atoms, which each bond to four Cu atoms. The Cu atoms are each similarly bond to four Sb atoms in a tetrahedral fashion. Since Cu presents itself as a d_{10} system, we do not expect any magnetism or strong electron correlations in $LaCuSb_2$.

Fig. 7.1(c) shows the Fermi surface of $LaCuSb_2$, measured by ARPES at $\hbar\omega = 80\,\text{eV}$. The high-symmetry points of the first BZ are shown in red. As a comparison, a DFT calculation of the Fermi surface is shown in Fig. 7.1(d). Both, experimental and theoretical data reveal an absence of bands close to the Fermi level around $\overline{\text{M}}$ and a diamond-like structure around $\overline{\Gamma}$, almost, but not quite, connecting the $\overline{\text{X}}$ points. The internal structure around the $\overline{\Gamma}$ point is better visible in successive BZs, since matrix element effects reduce the intensity in the first BZ considerably. All these features are commonly found in SG 129 and are present here as well. It would now be interesting to see, if we can resolve any surface states close to the $\overline{\text{X}}$ point, which were present in, for example, ZrSiS (cf. Fig. 4.3(a) and (b)). An extension of the $\overline{\text{X}}$ point Fermi surface intensity along $\overline{\text{X}}$-$\overline{\text{M}}$ was a clear indication of a surface state there. For this, we evaluate the DFT bulk band calculations first. As shown in Fig. 7.1(e), the bands are again four-fold degenerate at X and M (R and A, respectively) due to the nonsymmorphic symmetry

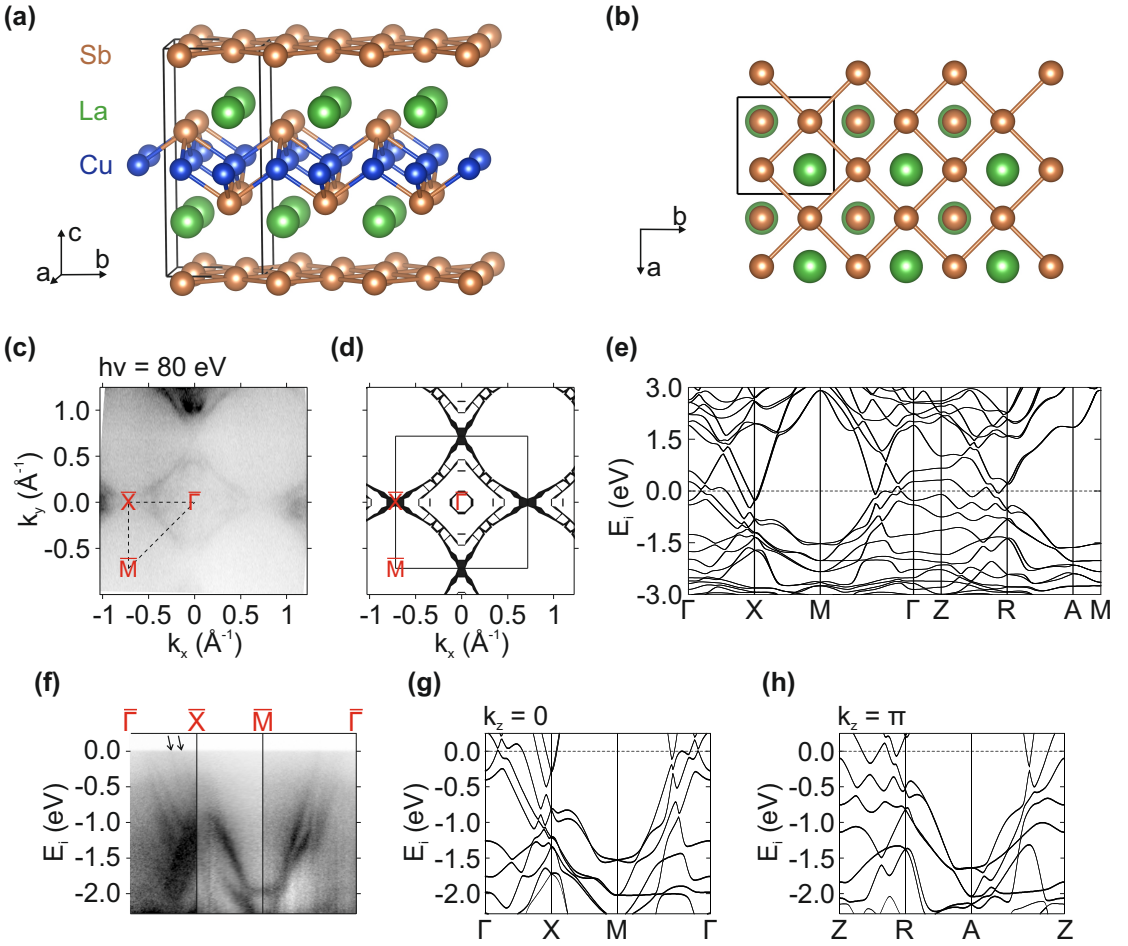

Figure 7.1: (a) and (b) Side and top view of the crystal structure of $LaCuSb_2$, respectively. The unit cell is indicated in black. (c) ARPES Fermi surface measured at $\hbar\omega = 80$ eV. The high-symmetry points of the first BZ are shown in red. (d) Corresponding Fermi surface DFT calculation. (e) DFT band structure calculations with SOC. (f) ARPES spectra along the path shown in dashed lines in (c). Bands with very weak intensity are indicated with arrows. (g) and (h) Corresponding $k_z = 0$ plane and $k_z = \pi$ plane of the dispersion in (f), revealing the better agreement of the ARPES data with the BZ center plane. The figure is part of a manuscript soon to be submitted.

present in the system. The X point further reveals some bands dispersing above the Fermi level along X-M, which was usually deserted of bulk bands and a good indication for surface bands. Since there is no direct indication for a predestined surface state area, we compare the dispersion measured in ARPES and theoretically predicted in DFT directly. Due to the significant k_z dispersion present in $LaCuSb_2$, we oppose the ARPES spectra in Fig. 7.1(f) with the $k_z = 0$ plane in (g) and the $k_z = \pi$ plane in (h). The easiest feature to identify the k_z plane in the DFT data is the number of linearly dispersing crossings of the Fermi level along $\overline{\Gamma}$-$\overline{X}$. The experimental data clearly resolve four bands, two of which are weak in intensity but indicated by arrows. This situation of extended linear dispersion is caught perfectly along Γ-X, while Z-R would

predict an area of several oscillating bands here. The following parabolic dispersion towards $\overline{\text{M}}$ along $\overline{\text{X}}$-$\overline{\text{M}}$ is nearly independent of k_z and present in (g) and (h). The only feature, remotely more accurately attributed to the $k_z = \pi$ plane, is visible in the energy gap between the first and second pair of bands along $\overline{\text{X}}$-$\overline{\text{M}}$ in panel (f). Shortly before the $\overline{\text{M}}$ point, these bands show a forbidden crossing that is gapped by SOC, but stronger gapped in the $k_z = 0$ plane. This big gap is absence in the $k_z = \pi$ plane and reproduces the experimental spectra better here. We, therefore, conclude that for a photon energy of 80 eV, the ARPES spectra are recorded close to, but slightly off, the BZ center plane. We were, however, not able to resolve any additional states in the ARPES data that we could relate to surface-derived states. It is possible that the surface states run in parallel and on top of the bulk bands in this energy range, which could be uncovered by performing slab calculations, which were not available at the time of this writing.

Our ARPES measurements did reveal, however, the presence of bands linearly dispersing along a large energy range of at least 0.5 eV, which could give rise to Dirac fermion physics at the crossing points of these bands, explaining many of the exotic properties, e.g. the large linear magnetoresistance, in $LaCuSb_2$. A manuscript on these measurements, as well as, on the here presented ARPES data, is in preparation.

7.2 Topology and superconductivity

To evaluate the topological properties present in $LaCuSb_2$, quantum Shubnikov-de Haas (SdH) oscillations were recorded. The resistivity was measured at high-magnetic fields, where periodic oscillations can be observed, if the separation of the Landau levels is large enough (usually fulfilled in Dirac materials) and the temperature is low enough for the carriers to populate the lower Landau levels. Fig. 7.2(a) shows the amplitude of the SdH quantum oscillations at $T = 0.27\,\text{K}$ as a function of inverse field. The four-point resistance measurements were performed on single-crystal structures prepared by focused ion beam lithography and measured in the setup shown in panel (b). Measurements of the c-axis resistivity used an excitation current of $150\,\mu\text{A}$ with magnetic fields up to 12 T applied along the c axis. The dominant SdH oscillation has a frequency of 49.6 T and can be observed up to 30 K, as shown in the FFT data of panel (c). It is possible to plot the inverse field positions of the oscillations against the n-th Landau level index (where maxima are integer and minima are half-integer indices) to fit a linear function to the data points and extract the index-axis crossing point γ. This crossing point is related to the Berry phase ϕ_B [99, 100]:

$$\gamma = \frac{1}{2} + \frac{\phi_\text{B}}{2\pi} \tag{7.1}$$

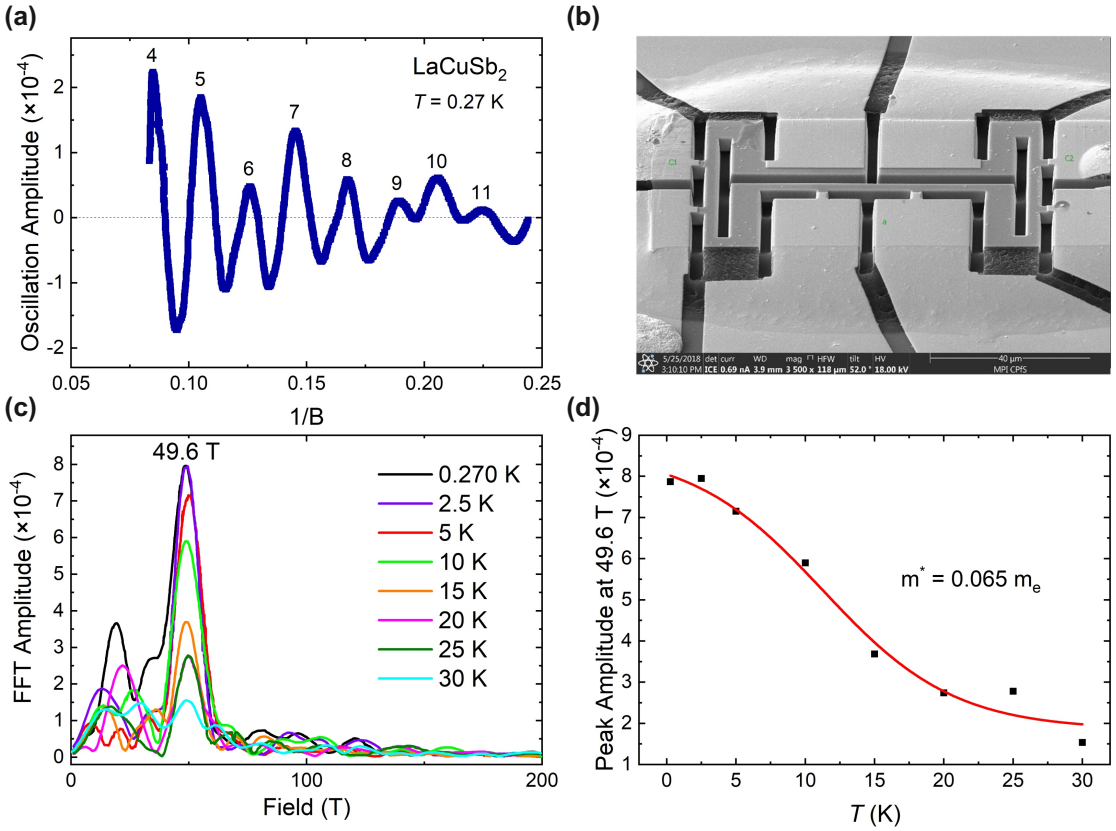

Figure 7.2: Quantum SdH oscillation measurements of $LaCuSb_2$. (a) Amplitude oscillations in the resistivity measurement at $T = 0.27\,\mathrm{K}$. (b) Sample setup of the four-point resistance measurements. (c) FFT amplitude of the measurement in (a) for various temperatures shown in different colors. The predominant frequency is identified as 49.6 T. (d) Temperature evolution of the FFT amplitude of the 49.6 T peak. Lifshitz-Kosevich theory allows for the determination of the effective electron mass as $m^* = 0.065\mathrm{m_e}$. The figure is part of a manuscript soon to be submitted.

And although this analysis results in a γ of -0.18(5) in $LaCuSb_2$, which would yield a ϕ_B of approximately π, if we consider Dirac fermions resulting in a $\gamma = -\frac{1}{8}$ factor [101], this finding is not robust without performing Hall measurements on the same sample as well to determine the absolute phase from the resistivity. At the writing of this thesis, these measurements are still pending.

It is, however, possible to plot the FFT amplitude of panel (c) against their temperatures, which allows us to obtain information about the effective carrier mass m^* and the Fermi momentum k_F according to the Lifshitz-Kosevich theory [102]. The values are extracted from the fit in Fig. 7.2(d) and are determined to be $m^* = 0.065\mathrm{m_e}$ and $k_\mathrm{F} = 3.88 \times 10^8\,\mathrm{m}^{-1}$, of which the ultra-low carrier mass indicates strongly the presence of Dirac fermions.

This evaluation of the topological nature is only a preliminary one right now and the

determination of the π Berry phase is not yet completed, it however shows the potential $LaCuSb_2$ has in this field. One the matter of superconductivity, there have been several claims in the literature that $LaCuSb_2$ turns superconductive below $T_c = 0.9\,K$ [15, 16], although, at the time of this writing, we were not able to confirm this phase transition. Should this last step be realized, $LaCuSb_2$ might provide an interesting model system on the interface between Dirac physics, topology and superconductivity.

CHAPTER 8

$GdTe_3$ - Towards Monolayer Antiferromagnetism[1]

'Out-of-the-box' is where I live.

– LT. KARA 'STARBUCK' THRACE

The previous chapters focused all on the many features and application possibilities of space group 129. There are however limitations to this family of compounds that prevent materials like ZrSiS from being utilized in certain fields of material science. One such limitation lies in its 2D scaling capability. The field of 2D materials does not only include physical properties like Dirac fermions [103], topological insulators [104] or Ising superconductivity [105], but did also recently get expanded by 'twistronic' devices [13]. Twistronic applications utilize the twist angle in 2D bilayer heterostacks to influence their electronic structure, of which superconducting graphene is a prominent example [106]. The idea to employ 2D materials in applications is not a new idea however, as they are used in spintronic devices already [107]. Very often, their magnetic properties are of primary importance in this context, which forced people to be content with the poor carrier mobilities these materials offered [108]. The introduction of a magnetic 2D material with high carrier mobility and a resulting large mean free path would open up a new way of device fabrication.

It is in this context that $GdTe_3$ could contribute to an advancement of the field, since it combines high carrier mobilities with an antiferromagnetic bulk and thin flake structure at low temperatures. In contrast to ZrSiS, this is possible due to the combination of a clear van der Waals gap in the crystal structure and the f electrons comprised in the Gd atoms. Rare-earth tritellurides (RTe_3, R = La-Nd, Sm and Gd-Tm) have already

[1] This chapter is based on a publication soon to be submitted

been shown in the past to exhibit an incommensurate charge density wave (CDW) [109, 110, 111, 112, 113, 114, 115, 116, 117] in combination with rich magnetic phases [118, 119] and even superconductivity at high pressures [120, 121]. Sec. 8.1 will introduce the electronic structure of $GdTe_3$ and show the emergence of the CDW, gapping almost all pockets at the Fermi level. Sec. 8.2 will then present its potential in the dimensional reduction by exfoliation and AFM order it demonstrates at low temperatures.

8.1 Nesting driven charge density wave

The crystal structure of $GdTe_3$ contains many elements familiar from SG 129. Without considering the CDW for now, it crystallizes in the orthorombic space group *Bmmb*, illustrated in Fig. 8.1(a). The two in-plane lattice parameters deviate however only slightly between $a = 4.320\,\text{Å}$ and $b = 4.330\,\text{Å}$, while the out-of-plane axis $c = 25.570\,\text{Å}$ is considerably longer. $GdTe_3$ features a double-layer of Te atoms forming a square-net structure intermittent by a double corrugated Gd-Te slab. While the square-net structure is again a good indication for linearly dispersing bands and the considerably large van der Waals gap, present between the Te sheets, allows for an exfoliation of the material, the Gd-Te slab will be responsible for the low-temperature AFM order.

The x-ray diffraction data of Fig. 8.1(b) attest the phase purity of the as-grown crystals (microscopy and SEM picture in insets). Below 377 K, $GdTe_3$ hosts a single CDW along the b axis [113], which is, for example, clearly resolved in the STM image of panel (c), taken at 72 K. It furthermore reveals a very low defect concentration of roughly one defect per 200 unit cells. The temperature-dependent magnetization data of Fig. 8.1(d), finally, confirm the AFM order arising below the Néel temperature $T_N = 12.0\,\text{K}$. Two additional magnetic transitions at $T_1 = 7.0\,\text{K}$ and $T_2 = 10.0\,\text{K}$ are visible in the low-temperature inset, which were not reported in the literature so far, but will not be the focus of this thesis.

The CDW of $GdTe_3$ results in a k-dependent gapping of the bands around the Fermi surface along k_y. This is clearly resolved in the ARPES data of Fig. 8.2(a), where there are no bands visible contributing to the Fermi surface along $\overline{\Gamma}$-$\overline{\text{Y}}$-$\overline{\Gamma}'$. The overall shape of the Fermi surface is shown in the theoretical picture of panel (a). It consists of two rectangles (a small and a big one centered around the $\overline{\Gamma}$ points), which can be explained by starting from a 2D picture of the p_x and p_y orbitals of the Te square net and successively adding the effects of p_x-p_y interactions and the doubling of the unit cell necessary in a and b, when the unit cell is expanded to 3D (again leading to a back-folding in k space) [122]. This also directly results in the dispersion shown in Fig. 8.2(b) along $\overline{\Gamma}$-$\overline{\text{X}}$, 45° off the high-symmetry line and $\overline{\text{X}}$-$\overline{\text{M}}$. The ARPES data

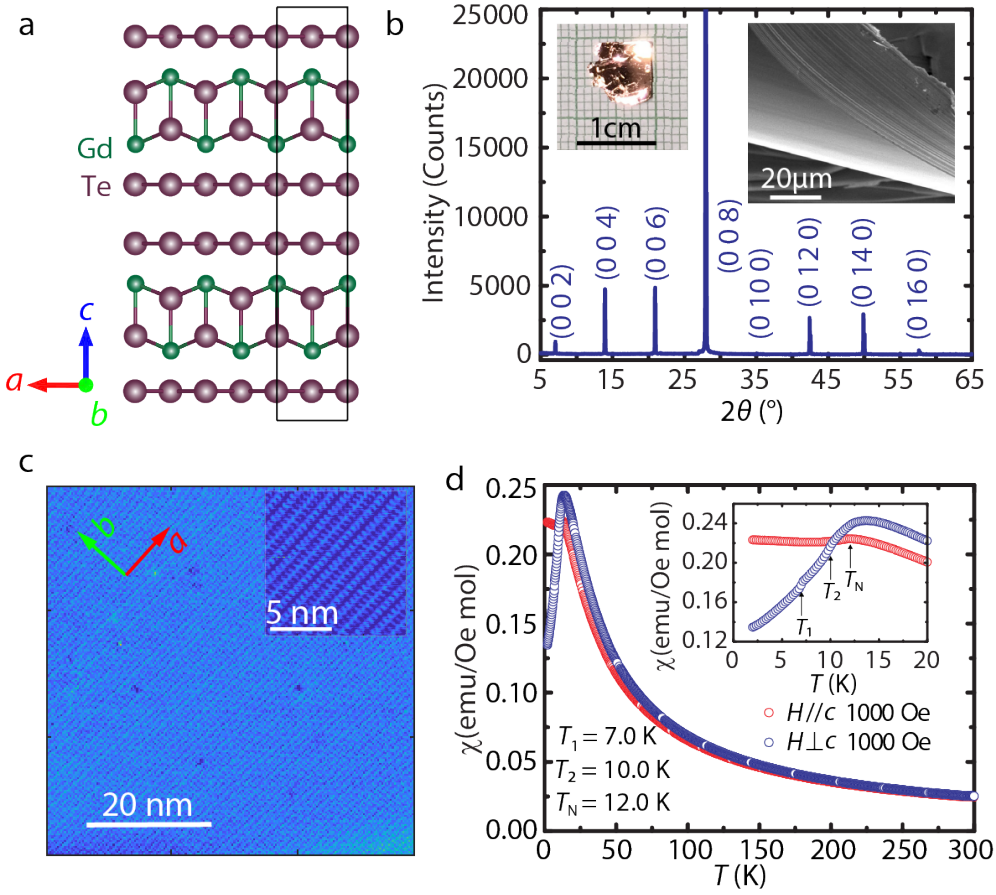

Figure 8.1: Structural characterization of $GdTe_3$. (a) Crystal structure containing a double van der Waals-gap layer of Te. The unit cell is indicated in black. (b) Powder x-ray diffraction pattern of a oriented single crystal showing only the $00l$ reflections. (c) STM image measured at 72 K at a bias of 0.2 V. The CDW vector is visible along b. (d) Temperature-dependent magnetization data for a field parallel (red) and perpendicular (blue) to the c axis. Phase transition temperatures are indicated by arrows. The figure is part of a manuscript soon to be submitted.

is shown without further processing and in its second derivative form in panel (b), both revealing certain parts of the band structure better than the other representation.

Special focus should be payed to the $\overline{\text{X}}$ point, being the only high-symmetry point not fully or partially gapped by the CDW. The bands contributing to the Fermi surface around this point can be traced and their dispersion is superimposed on the bands and explicitly shown in Fig. 8.2(c). Their Fermi level puncture points are also shown in panel (a) in the corresponding colors. Along the high-symmetry line, only two Fermi surface intersections can be identified, corresponding to the blue and red pocket along $\overline{\Gamma}$-$\overline{\text{X}}$ in the theory of panel (a). The two Fermi surface crossings, 45° off the high-symmetry line, however, allow us further to recognize that the red pocket around $\overline{\text{X}}$

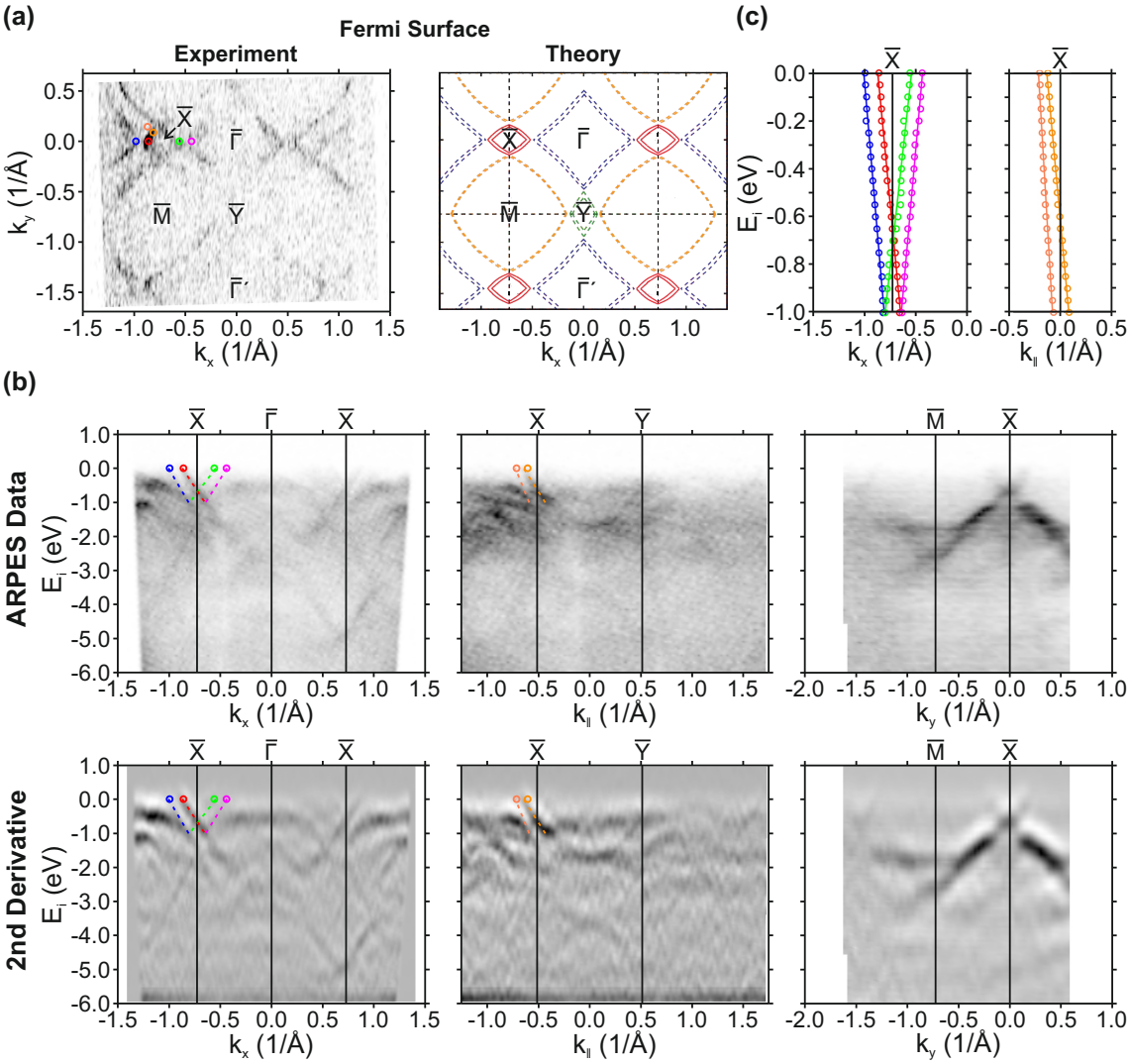

Figure 8.2: Electronic structure characterization of $GdTe_3$. (a) Fermi surface in ARPES experiment and theory. The pockets around the $\overline{\text{X}}$ point are the only ones contributing to the quantum oscillations due to the gapping along k_y by the CDW. The two pockets around $\overline{\text{X}}$ are further split by the k_z dispersion resulting in four Fermi surface pockets. (b) ARPES dispersions at $\hbar\omega = 500\,\text{eV}$ along $\overline{\Gamma}$-$\overline{\text{X}}$, 45° off the high-symmetry line, and $\overline{\text{X}}$-$\overline{\text{M}}$ in normal and second derivative representation. (c) Band contributing to the Fermi surface around $\overline{\text{X}}$. The double bands shown in red in the theory of panel (a) are only resolved 45° off the high-symmetry line due to the high photon energy used in this experiment. The theory of panel (a) is adapted from a manuscript soon to be submitted.

actually consists of two bands, although this is hardly visible in the ARPES Fermi surface of panel (a), but indicated in the theory plot. From this doubling, 45° off the high-symmetry line, we can conclude that we should actually observe four crossings along $\overline{\Gamma}$-$\overline{\text{X}}$, which is not resolvable due to the low resolution of the high photon energy data.

The bands tracked in Fig. 8.2(c) also reveal a fairly high Fermi velocity from the bands around the $\overline{\mathrm{X}}$ point. The results are presented in Tab. 8.1. The values for ZrSiS [1] and graphene [123] are given below, which are very much comparable to the velocities found in $GdTe_3$:

band	Fermi velocity (eV Å)
blue	5.05 ± 0.03
violet	4.86 ± 0.02
red	4.52 ± 0.03
green	3.9 ± 0.07
tomato	7.36 ± 0.06
orange	4.71 ± 0.01
ZrSiS	4.3
graphene	6.7

Table 8.1: Fermi velocities of the bands around $\overline{\mathrm{X}}$ in $GdTe_3$ evaluated along $\overline{\Gamma}$-$\overline{\mathrm{X}}$ and 45° off the high-symmetry line. As a comparison, the values for ZrSiS [1] and graphene [123] are provided.

These values follow the expected trend of higher Fermi velocities angled off the high-symmetry line, but are slightly lower than the average Fermi velocity of 10 ± 1 eV Å extracted for $R\mathrm{Te}_3$ compounds in Ref. [122]. Since their analysis however did not consider $GdTe_3$ itself and they found strong deviations from this average value, we can easily account for our lower values by considering the poor band resolution at such a high photon energy. Besides the large slope of the bands forming the Fermi surface, their linear dispersion further suggests that $GdTe_3$ is a material with fairly high carrier mobility. Indeed, magnetic field-dependent in-plane resistivity measurements at various temperatures were performed and reveal magnetoresistance data similar to some nonmagnetic semimetals (mobilities on the order of $10^4\,\mathrm{cm}^2/\mathrm{Vs}$). Furthermore, the Fourier analysis of the de Haas-van Alphen (dHvA) effect allow for an estimation of the Fermi surface pockets responsible for these oscillations. The four oscillation frequencies translate to 2.13 %, 2.28 %, 3.67 % and 3.83 % of the BZ area, which is in very good agreement with the two pockets around $\overline{\mathrm{X}}$, if we consider their further splitting due to k_z dispersion.

8.2 Monolayer antiferromagnet

The high mobility and AFM order in single crystals is only one of the features important for applications with $GdTe_3$. We further have to show that it is scalable to two dimensions, while keeping its magnetic and electronic properties.

Fig. 8.3(a) shows an optical image of an exfoliated $GdTe_3$ sheet on a Si wafer covered with SiO_2. The highlighted area is presented in an atomic force microscopy (AFM) picture in panel (b) and reveals different few-layer regions. Along various step edges, indicated by white lines, the height profiles are plotted in panel (c). At the moment of this thesis' submission, we were able to exfoliate the flake down to three layers, which corresponds to 1.5 unit cells. We are therefore quite confident that it is only a matter of time until a single monolayer (half a unit cell) is realized.

In this low-dimensional confirmation, we performed Raman spectroscopy on a 7.5 nm thin flake to ascertain its atomic structure and measured the temperature-dependent resistivity of a 22 nm thin flake affirming its magnetic structure. Fig. 8.3(d) features changes in the resistivity slope showing the development of the CDW at 385 K and the

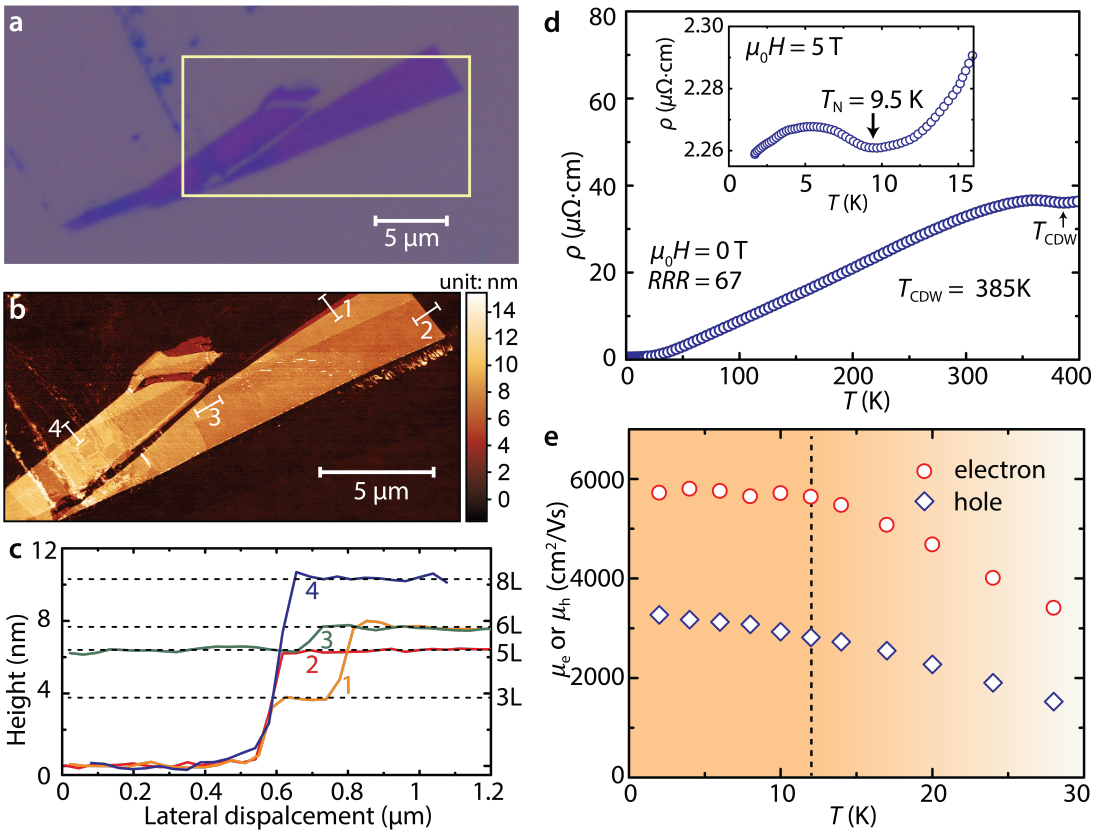

Figure 8.3: 2D scalability and carrier mobility of $GdTe_3$. (a) Optical microscopy of a thin flake. (b) AFM picture of the highlighted area in (a). (c) Height profile along the white lines in (b) revealing thin flakes down to three layers (1.5 unit cells). (d) Temperature-dependent resistivity measurements on a 22 nm thin flake. The inset shows the low temperature data under an applied field of 5 T. The CDW formation and the magnetic phase transition temperature are both retained for this low-dimensional confirmation. (e) Temperature-dependent electron and hole mobilities for the 22 nm thin flake. This figure is part of a manuscript soon to be submitted.

magnetic transition temperature at $T_N = 9.5\,K$. In this confirmation, $GdTe_3$ does not only retain its magnetic structure, but also shows very high mobility as apparent from Fig. 8.3(e), determined from the thin-flake transport measurements. These thicknesses are still preliminary, since thinner devices are theoretically possible but are very time intensive.

CHAPTER 9

$CuInTe_2$ - Towards Catalysis Applications[1]

Leeloo Dallas Multipass.

– LEELOOMINAÏ LEKATARIBA LAMINA-TCHAÏ EKBAT DE SEBAT

When we consider the possible areas of application for ARPES measurements, one would usually not name the field of photoelectrochemistry. The electrochemical conversion of solar energy into a storable and transportable fuel, like hydrogen in water splitting, does however pose some interesting questions on the electronic properties of the photoelectrodes. To evaluate the performance of a material as a potential photoelectrode, a good starting point are usually the thermodynamical requirements, like the band gap and position of the Fermi level. It is easy to forget that kinetic factors are of equal importance when it comes to practical applications [124]. While the sun light must excite electrons from the valence into the conduction band forming an electron-hole pair, the charge carriers must still separate afterwards to reach, for example, the adsorbed water molecules at the surface of the electrodes, forming O_2 and H_2, respectively. If this separation is not happening reasonable fast compared to the recombination rate, than the photoexcited charge carriers can never contribute to the electrochemical process. This separation process depends on the electrical properties and, therefore, the band structure. The charge transfer of majority charge carriers (holes) in the photocathode, for example, depends directly on the valence band structure, and more explicitly on the band velocity and the mobility of the quasi-particles [125].

[1] This chapter is based on publication [7]

This is an area where ARPES could contribute greatly to enhance the understanding of the intrinsic limitations of photoelectrodes. In most cases however, the band structure determination turns out to be rather difficult. Experimentally, due to the large band gaps, and theoretically due to the large influence SOC seems to have on these materials.

Here, we present ARPES data on $CuInTe_2$, which has its valence band maximum very close to the Fermi level and a rather small band gap, allowing for a characterization of the band structure via photoemission. As a first step, the surface BZ determination is presented in Sec. 9.1. Although $CuInTe_2$ belongs to a tetragonal space group, its reciprocal counter part showed only signs of a cubic BZ. Afterwards, we present the indications of a good catalytic performance in ARPES and in thermodynamical measurements in Sec. 9.2 and 9.3, respectively. We hope this proves not only the particular purpose of $CuInTe_2$, but also the importance of electronic measurements in general for the determination of the performance of good photoelectrocatalytic material.

9.1 Surface Brillouin zone determination

While ARPES measurements usually reveal the periodic order of reciprocal space quite accurately and is in accordance with the theoretical expectations from the unit cell calculations, in $CuInTe_2$ we found a discrepancy in this regard, which will be discussed here.

Fig. 9.1(a) shows the unit cell of tetragonal chalcopyrite $CuInTe_2$ and the primitive vectors in black. This theoretically results in the black BZ shown in the orthographic view of panel (b) and, with the natural cleavage plane located along the (112) plane, in the surface BZ side cuts shown in (c). From this, the projections of the Γ points should be distributed on a tetragonal lattice in the surface BZ, shown in panel (d) in black dots. The theoretical first BZ around $\overline{\Gamma}$ is shown as a black frame. This is, however, not what we observed in the constant energy cuts of the ARPES measurements in Fig. 9.2(a). The $\overline{\Gamma}$ points are clearly showing a hexagonal unit cell structure. We can superpose this hexagonal structure in blue on the tetragonal results in Fig. 9.1. If we follow the bigger, blue hexagonal BZ reversely, starting from panel (d), and keeping in mind that the cleaving plane in the reciprocal coordinate frame of the hexagonal BZ is the [111] direction, we end up with the blue unit cell vectors in panel (a). These clearly indicate the primitive vectors of the smaller, cubic zinc blende unit cell.

Already Pettenkofer et al. [126] reported on such a pseudo-cubic unit cell in $CuInSe_2$ and similar phenomena have also been reported in the orthorombic structure of the perovskite $CaTiO_3$ [127]. One driving factor for this phenomenon seems to be the lattice parameters of $CuInTe_2$. Since $c \approx 2a$, it is possible to derive the tetragonal unit

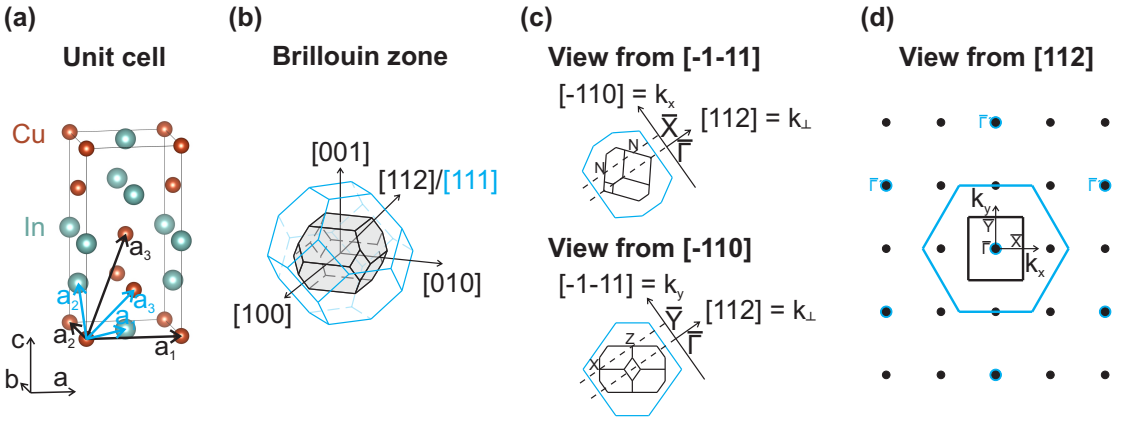

Figure 9.1: Unit cell determination of $CuInTe_2$. Items belonging to the tetragonal and cubic unit cell are shown in black and blue, respectively. (a) Crystal structure of the tetragonal unit cell. The primitive vectors are indicated with arrows. Te atoms are not plotted but are each tetrahedrally connected to two In and Cu atoms. (b) First BZ with the cleaving plane direction indicated along [112] or [111], respectively. (c) Side-views of the first BZ, with high-symmetry point projections towards the surface BZ. (d) $\overline{\Gamma}$ points of the surface BZ. The ARPES data of Fig. 9.2 match the hexagonal BZ belonging to the cubic unit cell. Figure adapted from Ref. [7].

cell by a "stacked" zinc blende structure of two cubic unit cells along c, with a lattice mismatch of only 0.1 %. Thus, the elemental difference between the tetragonal and the "stacked" cubic unit cell is only given by the difference in the two cation species Cu^{+1} and In^{3+}. This seems to be resolvable by diffraction, but invisible to our APRES measurements.

It is prudent to note here, that our DFT calculations are still based on the tetragonal structure, which requires us to compare the positions of high-symmetry points carefully. This was done in Fig. 9.1(c), where we identified the k_x direction with the DFT path along Γ-N. k_y can be identified either with Γ-Z or Γ-X, much stronger depending on the k_z value, which will further be discussed in the following section.

9.2 The indications of a good photocathode in ARPES

After having analyzed the theoretical surface BZ of $CuInTe_2$, we will now present the ARPES data measured at a photon energy of $\hbar\omega = 80\,\text{eV}$ in Fig. 9.2. Panel (a) shows two constant energy cuts, at the Fermi level ($E_\text{i} = 0\,\text{eV}$) and at $E_\text{i} = -0.87\,\text{eV}$. The Fermi surface reveals only weak intensity spots at the $\overline{\Gamma}$ and $\overline{\Gamma}'$ points, since they are simultaneously the valence band maxima in $CuInTe_2$. It shows, however, a clear hexagonal

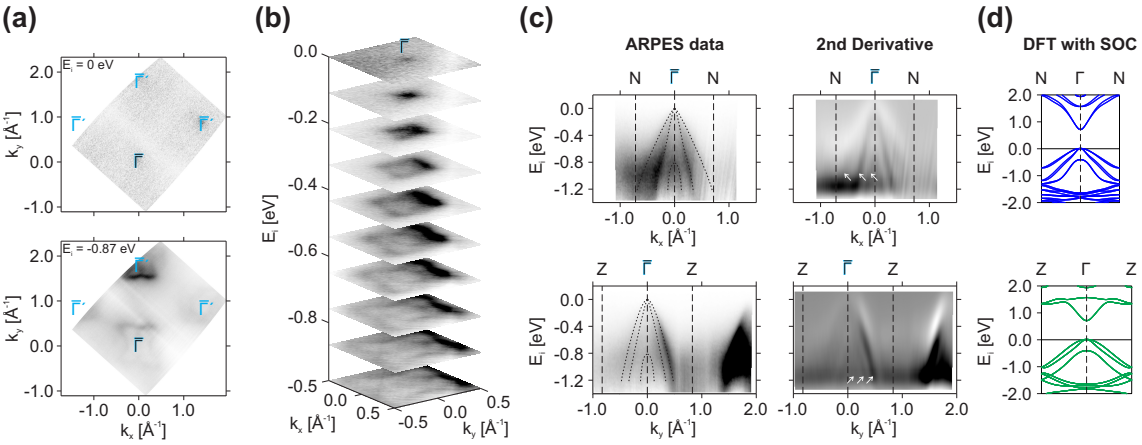

Figure 9.2: ARPES measurements of $CuInTe_2$. (a) Constant energy cuts at $E_i = 0$ and -0.87 eV. The $\overline{\Gamma}$ and $\overline{\Gamma}'$ points indicate a hexagonal BZ (the blue color indicates the influence of the cubic unit cell). (b) Evolution of the bands around the $\overline{\Gamma}$ point. (c) Shirley-background subtracted and secon derivative ARPES dispersions along $k_y = 0\text{Å}^{-1}$ and $k_x = 0\text{Å}^{-1}$, which represents the theoretical N-Γ-N and Z-Γ-Z direction in the tetragonal unit cell calculations, respectively. Band dispersions are indicated by dashed lines and white arrows. (d) DFT calculations with SOC for the dispersions in (c). Figure adapted from Ref. [7].

structure of the first BZ, which was the decisive factor in identifying the stacked cubic unit cell in Fig. 9.1. The distance between $\overline{\Gamma}$ and $\overline{\Gamma}'$ is experimentally determined at $1.66\,\text{Å}^{-1}$, matching the expected distance of the cubic BZ centers projected along its [111] direction perfectly. Fig. 9.2(b) shows the band evolution around $\overline{\Gamma}$, revealing an internal structure of several bands, leading to the clover-shaped feature surrounding $\overline{\Gamma}$. To evaluate this further, we analyzed the dispersion along $k_y = 0\text{Å}^{-1}$ (N-Γ-N) and $k_x = 0\text{Å}^{-1}$ (Z-Γ-Z) in the upper and lower row of panel (c), respectively. The corresponding bulk DFT calculations with SOC are shown in panel (d) and were identified according to Fig. 9.1(c). Along $k_x = 0\text{Å}^{-1}$, Γ-Z achieves a much better agreement with the experimental data, which makes us believe that the k_z plane is cutting the Z point for a photon energy of $\hbar\omega = 80\,\text{eV}$. Furthermore, the DFT band structure had to be stretched by a factor of 2, to accommodate for the changed distance between $\overline{\Gamma}$ and $\overline{\Gamma}'$ of the tetragonal and cubic unit cell. The dispersion plots of panel (c) show the Shirley background subtracted and second derivative ARPES spectra, revealing a pair of bands meeting very close to the Fermi level at $\overline{\Gamma}$. At $E_i \approx -0.8\,\text{eV}$, a third band, responsible for the internal clover shape in the constant energy cuts, crosses $\overline{\Gamma}$. All three bands are emphasized by dashed lines in the ARPES data and marked with white arrows in the second derivative data. These bands are qualitatively reproduced in the DFT data of panel (d), however, they are not as steeply dispersing as their experimental counterparts. To reach a quantitative agreement, the DFT energy axis needs to be stretched by a factor of 1.9, a trend opposite to the commonly found reduction in theoretical

band width calculations usually attributed to electron-electron correlations [128]. In fact, the experimentally determined band velocity slightly below the Fermi level already amounts to 2.5-5.4×10^5 m/s, about 25-50 % of the Fermi velocity in graphene [123]. We evaluated the band slope slightly below the Fermi level, since the parabolic dispersion very close to E_F of course decreases the band velocity quite considerably. Our evaluation is however justified due to the photo-absorbed excitement of electrons well below the Fermi level, which allows for a high initial band velocity of the created holes. This high band velocity is interesting in the context of photocatalysts, since in the case of halide perovskite materials, it has been shown theoretically that the high carrier velocities can be related to reduced recombination rates and high mobilities [125]. Additionally, the wide range of linearly dispersing bands, results in low effective masses (for perfectly linear dispersions, even zero effective mass), which results in high charge carrier mobilities. As a comparison, the experimentally determined mobility of the *p*-type charge carriers was estimated to be 870 $cm^2V^{-1}s^{-1}$, two orders of magnitude greater than for poly-crystalline samples of $CuInS_2$ and $CuInSe_2$ [129] and eight- (three-)times higher than those of other light-harvesting semiconductors like single-crystalline $CH_3NH_3PbI_3$ [130] ($BiVO_4$ [131]).

Lastly, we have to consider the effect of SOC on the electronic and catalytic properties. As can be seen in Fig. S4 of the SI of Ref. [7], the three experimentally observed bands showing their maximum at Γ can only be reproduced by DFT when considering SOC. Otherwise the third band is degenerate with one of the others along Z-Γ-Z and there is never a -0.8 eV shift of the third band to lower initial state energies. SOC can, however, also more indirectly influence the carrier lift time. It has been shown that a Rashba-type spin splitting, due to the effect of SOC on the surface of an inversion symmetric material, can result in spin-split indirect band gaps that reduce the recombination rate and therefore greatly enhance the carrier lift time [132, 133, 134]. While $CuInTe_2$ lacks spacial inversion symmetry to begin with, already the bulk bands show spin-splitting when considering the effect of SOC, due to a combination of bulk Rashba and Dresselhaus effects. To analyze the effect of therefore created spin-split indirect band gaps, we in principle need to calculate the spin distribution around the Γ point. This can be easily done along Γ-Z, where the C_{2v} symmetry distributes the spins in-plane, as it would be case for a pure Rashba-type splitting [135], but already along Γ-N, the situation is not as obviously clarifiable, since the valence and conduction band could be influenced individually. Since we, however, do not observe a strong Rashba-type splitting at the surface of $CuInTe_2$, this effect, if present, will only have a minor influence on the mobility in the context of the other effects discussed above.

9.3 Thermodynamical measurements

While there are, to our knowledge, no studies on the photoelectrochemical properties of $CuInTe_2$ and our own study is not concluded at the moment of this thesis' submission, we can at least confirm that this material is thermodynamically capable of photoelectrochemical water reduction.

To this end, we determined the flat band potential of the valence band by an AC impedance measurement for a Mott-Schottky (M-S) analysis and compared it to the results of a chopped-light linear sweep voltammetry (LSV) measurement. For a more detailed explanation of the two measurement methods, the reader is revered to Ref. [7]. Fig. 9.3(a) shows the results of the M-S plot of $CuInTe_2$. The measurement was performed at pH 9 in 0.6 M $Na_2SO_{4(aq)}$ for different AC frequencies. The common x-axis intercept of the linear approximations of the different frequency lines can be used to

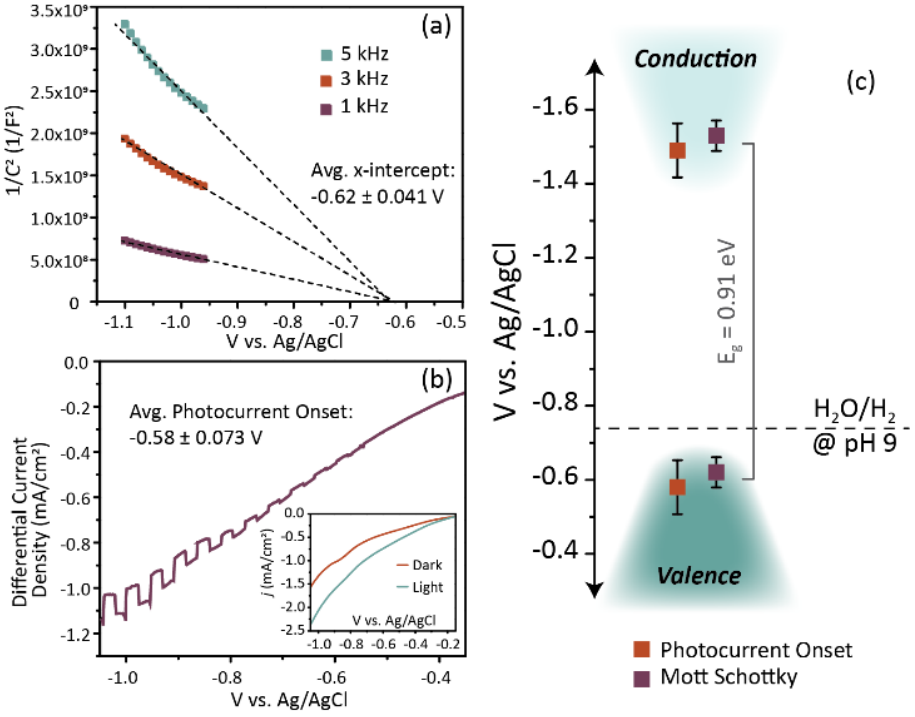

Figure 9.3: Thermodynamical measurements of $CuInTe_2$. (a) M-S plot at 1, 3 and 5 kHz under dark conditions. The common x-axis intercept is determined by linear approximation. (b) Chopped-light LSV curve. The dark current was subtracted from the light measurement (both shown in inset) to obtain the graph. The onset potential is determined by the growth from the baseline. (c) Schematic band edge diagram. The conduction band minimum was determined by the gap size. The black dashed line represents the water reduction potential at comparable conditions and is comprised in the gap. Figure taken from Ref. [7].

determine the flat band potential even if the semiconductor-electrolyte interface is never ideally capacitive [136, 137]. This M-S analysis results in a flat band potential of -0.62 ± 0.041 V vs. Ag/AgCl. Fig. 9.3(b) shows the chopped LSV plot. The j-V curve was obtained by subtracting the dark current from the illuminated curve, which are shown in the inset LSV scans. Here, the flat band potential can be identified as the potential at which the photocurrent starts to vary from its baseline, the onset potential. It is determined as -0.58 ± 0.073 V vs. Ag/AgCl at pH 9.

The two results within the error bars and schematically shown in Fig. 9.3(c). The conduction band minimum was approximated by the optically determined band gap of 0.91 eV [7]. Since the band edges comprise the H_2 evolution potential vs. Ag/AgCl at pH 9 (dotted line in panel (c)), we can confirm that $CuInTe_2$ is thermodynamically capable of photoelectrochemical water reduction.

CHAPTER 10

Conclusion & Outlook

In this work, we used ARPES to study the electronic properties of novel Dirac semimetals. Our aim was to advance the field of material science and physics by uncovering the band structure characteristics of new compounds. Since these materials were for the most part not characterized beforehand, we chose ARPES to simultaneously resolve the electronic surface and bulk band structure, while using DFT and tight-binding calculations to explain the origin of the observed features.

10.1 The many faces of space group 129

In the first part of this thesis, we focused on materials crystallizing in SG 129. The square-net motif incorporated in many of these compounds allows for the realization of linearly dispersing Dirac crossings close to the Fermi level, which is combined with the nonsymmorphically protected crossings enforced at certain high-symmetry points. In particular, ZrSiS and related compounds proved to be a rich play ground when it comes to the interplay of bulk and surface electronic structure. Here, we showed that ZrSiS is a Dirac nodal line material with the nodal line forming in a diamond-shape in the $k_z = 0$ and π plane, which are perpendicularly connected. This cage-like structure is only slightly dispersing close to the Fermi level. The nonsymmorphic symmetry in the bulk, furthermore, enforces degeneracies along X-R and M-A, which are resistant to gapping due to SOC. These bulk features were superimposed by surface-derived bands in the ARPES spectra, which do not fit any of the known surface state origins in the literature. We showed that they can be explained by the breaking of nonsymmorphic symmetry at the (001) surface and hence reduced surface symmetry, resulting in the formation of 'floating surface states'. Such surface states could be found in all analyzed compounds of this family, like ZrSiTe and CeSbTe, but should be a common feature of nonsymmorphic space groups in general. It is therefore one of the

main findings of this thesis. In addition, the isostructural compound ZrSiTe featured, in addition, the perfect ratio between *c* and *a* axes to ensure the energetic position of the nonsymmorphic bulk degeneracy at the X point to be located very close to the Fermi level. This marks the first step towards the characterization of nonsymmorphic symmetry in transport experiments. Compared to ZrSiS, ZrSiTe shows a much more complex surface band structure. One of these bands, occupying the projected overlap of the nodal lines, was identified as a representative of the topological 'drumhead surface states'. Furthermore, CeSbTe allowed for the combination of magnetism and nonsymmorphic symmetry. A neutron scattering experiment identified the anitferromagnetic ground state featuring a doubling of the *c* axis in the magnetic order, which complemented the magnetic phase diagram of CeSbTe. In this compound, it was theoretically shown that it should be possible to observe Weyl physics and degeneracies of higher order in the fully polarized and the antiferromagnetic state, respectively. Additionally, the increased SOC was shown to be advantageous in the formation of isotropic Dirac cones around the nonsymmorphically protected high-symmetry points. Lastly, $LaCuSb_2$ showed potential for combining the fields of topology with superconductivity in SG 129.

Many of these projects were only a proof of principle so far and can be extended with specific measurements. One example is the AFM phase of CeSbTe, which is not accessible due to the low-temperature restriction. If a low-temperature beamtime, e.g. at the 1^3 beamline at Bessy-II, could be conducted, it would be worthwhile to observe the AFM phase by means of ARPES. As we showed in the DFT calculations, this could lead to the observation of a true eight-fold degeneracy at the A point. The same low temperature argument can be made about $LaCuSb_2$, whose topological properties are so far only hinted at and whose low-temperature superconducting phase has not yet been observed by us. Furthermore, combining the results obtained by different compounds might be interesting in the future. For example, the correct structural ratio to move the nonsymmorphically protected Dirac point to the Fermi level, like in ZrSiTe, in combination with strong SOC (gapping most other crossings and resulting in an isotropic nonsymmorphic degeneracy), like shown in CeSbTe, could be very interesting to measure the nonsymmorphic properties of a material by transport experiments. Then again, the square-net materials of SG 129 are vastly uncharacterized concerning their electronic properties so far, and the interplay of the stabilizing *d* bands close to the Fermi level might be very interesting in the context of catalysis.

10.2 $GdTe_3$ and its magnetic structure

$GdTe_3$ was shown to be the first antiferromagnetic monolayer material with high mobility. In this context, ARPES observed the existence of the CDW in this material and

correlated the quantum oscillations from the dHvA effect with the size of the Fermi pockets around the $\overline{\text{X}}$ point. These are the only pockets not partially or fully gapped by the CDW. The Fermi velocities of bands crossing the Fermi surface there are slightly lower than in other rare-earth tritellurides, but still on the order of ZrSiS and graphene.

It would be desirable to resolve the exact AFM structure below T_N directly by means of neutron diffraction (as presented in the case of CeSbTe), but such experiments proved to be problematic because of the high neutron absorption coefficient of Gd. An inelastic x-ray scattering experiment might be able to resolve the structure and a beamtime is planned at the writing of this thesis.

10.3 $CuInTe_2$ applications in photoelectrochemistry

Using ARPES in the field of semiconductors is usually problematic due to the intrinsically large band gaps. In $CuInTe_2$ we used ARPES to resolve the valence band structure. This was possible due to the valence band maximum being located very close to the Fermi level. We resolved its pseudo-cubic BZ in the ARPES experiment and verified its potential for photoelectrochemistry by observing a wide range of linearly dispersing bands. With this in mind, the strong influence of SOC on the band structure is quite obvious, which demonstrates the importance of measurements to verify the DFT codes, which only consider SOC in a second variational procedure.

Since our experiments prove the thermodynamical possibility for water reduction, the next step would certainly be a complete photoelectrochemical study on the properties of $CuInTe_2$. Should this yield promising results, $CuInTe_2$ might be able to replace some of the, so far used, semiconducting materials in this field.

Bibliography

[1] Leslie M Schoop, Mazhar N Ali, Carola Straßer, Andreas Topp, Andrei Varykhalov, Dmitry Marchenko, Viola Duppel, Stuart SP Parkin, Bettina V Lotsch, and Christian R Ast. Dirac cone protected by non-symmorphic symmetry and three-dimensional Dirac line node in ZrSiS. *Nature Communications*, 7:11696, 2016.

[2] Andreas Topp, Judith M Lippmann, Andrei Varykhalov, Viola Duppel, Bettina V Lotsch, Christian R Ast, and Leslie M Schoop. Non-symmorphic band degeneracy at the Fermi level in ZrSiTe. *New Journal of Physics*, 18(12):125014, 2016.

[3] Andreas Topp, Raquel Queiroz, Andreas Grüneis, Lukas Müchler, Andreas W Rost, Andrei Varykhalov, Dmitry Marchenko, Maxim Krivenkov, Fanny Rodolakis, Jessica L McChesney, et al. Surface floating 2D bands in layered nonsymmorphic semimetals: ZrSiS and related compounds. *Physical Review X*, 7(4):041073, 2017.

[4] Andreas Topp, Maia G Vergniory, Maxim Krivenkov, Andrei Varykhalov, Fanny Rodolakis, Jessica L McChesney, Bettina V Lotsch, Christian R Ast, and Leslie M Schoop. The effect of spin-orbit coupling on nonsymmorphic square-net compounds. *Journal of Physics and Chemistry of Solids*, 2017.

[5] Leslie M Schoop, Andreas Topp, Judith Lippmann, Fabio Orlandi, Lukas Müchler, Maia G Vergniory, Yan Sun, Andreas W Rost, Viola Duppel, Maxim Krivenkov, et al. Tunable Weyl and Dirac states in the nonsymmorphic compound CeSbTe. *Science Advances*, 4(2):eaar2317, 2018.

[6] Leslie M Schoop and Andreas Topp. Topological Materials and Solid-State Chemistry - Finding and Characterizing New Topological Materials. In *Topological Matter*, pages 211–243. Springer, 2018.

[7] Jessica Frick, Andreas Topp, Sebastian Klemenz, Maxim Krivenkov, Andrei Varykhalov, Christian R Ast, Andrew B Bocarsly, and Leslie M Schoop. Single Crystal Growth and Characterization of the Chalcopyrite Semiconductor $CuInTe_2$ for Photoelectrochemical Solar Fuel Production. *The Journal of Physical Chemistry Letters*, 2018.

[8] Martin M Atalla, Eileen Tannenbaum, and EJ Scheibner. Stabilization of silicon surfaces by thermally grown oxides. *Bell System Technical Journal*, 38(3):749–783, 1959.

[9] Dawon Kahng. Silicon-silicon dioxide surface device. In *Semiconductor Devices: Pioneering Papers*, pages 583–596. World Scientific, 1991.

[10] Bernard Field and Tapio Simula. Introduction to topological quantum computation with non-Abelian anyons. *Quantum Science and Technology*, 2018.

[11] Charles Tahan. Graphene qubit motivates materials science. *Nature Nanotechnology*, 14(2):102, 2019.

[12] Libor Šmejkal, Tomáš Jungwirth, and Jairo Sinova. Route towards Dirac and Weyl antiferromagnetic spintronics. *physica status solidi (RRL)-Rapid Research Letters*, 2017.

[13] Stephen Carr, Daniel Massatt, Shiang Fang, Paul Cazeaux, Mitchell Luskin, and Efthimios Kaxiras. Twistronics: Manipulating the electronic properties of two-dimensional layered structures through their twist angle. *Physical Review B*, 95(7):075420, 2017.

[14] B Bradlyn, J Cano, Z Wang, MG Vergniory, C Felser, RJ Cava, and BA Bernevig. Beyond Dirac and Weyl fermions: Unconventional quasiparticles in conventional crystals. *Science*, 353(6299), 2016.

[15] Yuji Muro, Naoya Takeda, and Masayasu Ishikawa. Magnetic and transport properties of dense Kondo systems, $CeTSb_2$ (T= Ni, Cu, Pd and Ag). *Journal of Alloys and Compounds*, 257(1-2):23–29, 1997.

[16] Piotr Ruszała, Maciej J Winiarski, and Małgorzata Samsel-Czekała. Dirac-like band structure of $LaTESb_2$ (TE= Ni, Cu, and Pd) superconductors by DFT calculations. *Computational Materials Science*, 154:106–110, 2018.

[17] Sydney G Davison and Maria Stęślicka. *Basic theory of surface states*, volume 46. Oxford University Press, 1996.

[18] Carlos Fiolhais, Fernando Nogueira, and Miguel AL Marques. *A primer in density functional theory*, volume 620. Springer Science & Business Media, 2003.

[19] Pierre Hohenberg and Walter Kohn. Inhomogeneous electron gas. *Physical review*, 136(3B):B864, 1964.

[20] Walter Kohn and Lu Jeu Sham. Self-consistent equations including exchange and correlation effects. *Physical review*, 140(4A):A1133, 1965.

[21] Mel Levy. Universal variational functionals of electron densities, first-order density matrices, and natural spin-orbitals and solution of the v-representability problem. *Proceedings of the National Academy of Sciences*, 76(12):6062–6065, 1979.

[22] Neil W Ashcroft and David N Mermin. *Festkörperphysik*. Oldenbourg Verlag, 2012.

[23] John C Slater and George F Koster. Simplified LCAO method for the periodic potential problem. *Physical Review*, 94(6):1498, 1954.

[24] Leif Goodwin, AJ Skinner, and DG Pettifor. Generating transferable tight-binding parameters: application to silicon. *EPL (Europhysics Letters)*, 9(7):701, 1989.

[25] Adrian P Sutton, Mike W Finnis, David G Pettifor, and Y Ohta. The tight-binding bond model. *Journal of Physics C: Solid State Physics*, 21(1):35, 1988.

[26] Mike Finnis. *Interatomic forces in condensed matter*, volume 1. OUP Oxford, 2003.

[27] Anthony T Paxton et al. An introduction to the tight binding approximation–implementation by diagonalisation. *NIC Series*, 42:145–176, 2009.

[28] Bert Voigtländer. *Work Function, Contact Potential, and Kelvin Probe Scanning Force Microscopy*, pages 123–133. Springer Berlin Heidelberg, Berlin, Heidelberg, 2015.

[29] DP Woodruff, SL Hulbert, PD Johnson, and NV Smith. Unoccupied surface resonance on Cu (100) and the effect of vacuum-level pinning. *Physical Review B*, 31(6):4046, 1985.

[30] M Weinelt, M Kutschera, R Schmidt, Ch Orth, Th Fauster, and M Rohlfing. Electronic structure and electron dynamics at Si (100). *Applied Physics A*, 80(5):995–1003, 2005.

[31] D Pacilé, CR Ast, M Papagno, C Da Silva, L Moreschini, M Falub, Ari P Seitsonen, and M Grioni. Electronic structure of an ordered Pb/Ag(111) surface alloy: Theory and experiment. *Physical Review B*, 73(24):245429, 2006.

[32] Christian R Ast, Jürgen Henk, Arthur Ernst, Luca Moreschini, Mihaela C Falub, Daniela Pacilé, Patrick Bruno, Klaus Kern, and Marco Grioni. Giant spin splitting through surface alloying. *Physical Review Letters*, 98(18):186807, 2007.

[33] Rainer Fischer and Thomas Fauster. Coupling of image states to quantum-well states for au on pd (111). *Physical Review B*, 51(11):7112, 1995.

[34] Hadj M. Benia, Chengtian Lin, Klaus Kern, and Christian R. Ast. Reactive Chemical Doping of the Bi_2Se_3 Topological Insulator. *Physical Review Letters*, 107(17):177602, October 2011.

[35] William Shockley. On the surface states associated with a periodic potential. *Physical Review*, 56(4):317, 1939.

[36] Ig Tamm. Über eine mögliche Art der Elektronenbindung an Kristalloberflächen. *Zeitschrift für Physik*, 76(11-12):849–850, 1932.

[37] Binghai Yan, Benjamin Stadtmüller, Norman Haag, Sebastian Jakobs, Johannes Seidel, Dominik Jungkenn, Stefan Mathias, Mirko Cinchetti, Martin Aeschlimann, and Claudia Felser. Topological states on the gold surface. *Nature Communications*, 6:10167, 2015.

[38] Yoichi Ando. Topological insulator materials. *Journal of the Physical Society of Japan*, 82(10):102001, 2013.

[39] Liang Fu and Charles L Kane. Topological insulators with inversion symmetry. *Physical Review B*, 76(4):045302, 2007.

[40] Liang Fu, Charles L Kane, and Eugene J Mele. Topological insulators in three dimensions. *Physical Review Letters*, 98(10):106803, 2007.

[41] B Andrei Bernevig. It's been a Weyl coming. *Nature Physics*, 2015.

[42] Alexey A Soluyanov, Dominik Gresch, Zhijun Wang, QuanSheng Wu, Matthias Troyer, Xi Dai, and B Andrei Bernevig. Type-II Weyl semimetals. *Nature*, 527(7579):495–498, 2015.

[43] QD Gibson, LM Schoop, L Muechler, LS Xie, M Hirschberger, NP Ong, R Car, and RJ Cava. Three-dimensional Dirac semimetals: Design principles and predictions of new materials. *Physical Review B*, 91(20):205128, 2015.

[44] Frans R Klinkhamer and GE Volovik. Emergent CPT violation from the splitting of Fermi points. *International Journal of Modern Physics A*, 20(13):2795–2812, 2005.

[45] Youngkuk Kim, Benjamin J Wieder, CL Kane, and Andrew M Rappe. Dirac line nodes in inversion-symmetric crystals. *Physical Review Letters*, 115(3):036806, 2015.

[46] YH Chan, CK Chiu, MY Chou, and AP Schnyder. Ca_3P_2 and other topological semimetals with line nodes and drumhead surface states. *Physical Review B*, 93(20):205132, 2016.

[47] Ai Yamakage, Youichi Yamakawa, Yukio Tanaka, and Yoshihiko Okamoto. Line-Node Dirac Semimetal and Topological Insulating Phase in Noncentrosymmetric Pnictides CaAgX (X = P, As). *Journal of the Physical Society of Japan*, 85(1):013708, 2015.

[48] Sebastian Klemenz, Shiming Lei, and Leslie M Schoop. Topological Semimetals in Square-Net Materials. *arXiv preprint arXiv:1808.06619*, 2018.

[49] W Tremel and R Hoffmann. Square nets of main-group elements in solid-state materials. *Journal of the American Chemical Society*, 109(1):124–140, 1987.

[50] Harald Schäfer. *Chemical transport reactions*. Elsevier, 2016.

[51] CHL Goodman. *Crystal Growth*. Springer, 1974.

[52] Heinrich Hertz. Über einen Einfluss des ultravioletten Lichtes auf die electrische Entladung. *Annalen der Physik*, 267(8):983–1000, 1887.

[53] Albert Einstein. Über einen die Erzeugung und Verwandlung des Lichtes betreffenden heuristischen Gesichtspunkt. *Annalen der Physik*, 322(6):132–148, 1905.

[54] Wolfgang Schattke and Michel A Van Hove. *Solid-state photoemission and related methods: theory and experiment*. John Wiley & Sons, 2008.

[55] Oliver Hemmers, Peter Glans, David L Hansen, Honghong Wang, Scott B Whitfield, DW Llndle, Ralf Wehlitz, Jon C Levin, Ivan A Sellin, and Rupert CC Perera. Photoelectron spectroscopy and the dipole approximation. *Synchrotron Radiation News*, 9(6):40–45, 1996.

[56] Carl Neil Berglund and William Edward Spicer. Photoemission studies of copper and silver: theory. *Physical Review*, 136(4A):A1030, 1964.

[57] Peter J Feibelman and DE Eastman. Photoemission spectroscopy - correspondence between quantum theory and experimental phenomenology. *Physical Review B*, 10(12):4932, 1974.

[58] M Pl Seah and WA Dench. Quantitative electron spectroscopy of surfaces: A standard data base for electron inelastic mean free paths in solids. *Surface and Interface Analysis*, 1(1):2–11, 1979.

[59] Stefan Hüfner. *Photoelectron Spectroscopy*. Springer, Berlin, second edition edition, 1996.

[60] János Végh. The Shirley background revised. *Journal of Electron Spectroscopy and Related Phenomena*, 151(3):159–164, 2006.

[61] SL Dudarev, GA Botton, SY Savrasov, CJ Humphreys, and AP Sutton. Electron-energy-loss spectra and the structural stability of nickel oxide: An LSDA+ U study. *Physical Review B*, 57(3):1505, 1998.

[62] Laurent C Chapon, Pascal Manuel, Paolo G Radaelli, Chris Benson, Leigh Perrott, Stuart Ansell, Nigel J Rhodes, Davide Raspino, D Duxbury, E Spill, et al. Wish: the new powder and single crystal magnetic diffractometer on the second target station. *Neutron News*, 22(2):22–25, 2011.

[63] Václav Petříček, Michal Dušek, and Lukáš Palatinus. Crystallographic computing system JANA2006: general features. *Zeitschrift für Kristallographie-Crystalline Materials*, 229(5):345–352, 2014.

[64] Y Hancock. The 2010 Nobel Prize in physics - Ground-breaking experiments on graphene. *Journal of Physics D: Applied Physics*, 44(47):473001, 2011.

[65] Kirill I Bolotin, KJ Sikes, Zd Jiang, M Klima, G Fudenberg, J Hone, Ph Kim, and HL Stormer. Ultrahigh electron mobility in suspended graphene. *Solid State Communications*, 146(9-10):351–355, 2008.

[66] Matthew J Allen, Vincent C Tung, and Richard B Kaner. Honeycomb carbon: a review of graphene. *Chemical reviews*, 110(1):132–145, 2009.

[67] Jun Xiong, Satya Kushwaha, Jason Krizan, Tian Liang, RJ Cava, and NP Ong. Anomalous conductivity tensor in the Dirac semimetal Na_3Bi. *EPL (Europhysics Letters)*, 114(2):27002, 2016.

[68] T Liang, QD Gibson, MN Ali, M Liu, RJ Cava, and NP Ong. Ultrahigh mobility and giant magnetoresistance in the Dirac semimetal Cd_3As_2. *Nature Materials*, 14(3):280–284, 2015.

[69] Mazhar N Ali, Jun Xiong, Steven Flynn, Jing Tao, Quinn D Gibson, Leslie M Schoop, Tian Liang, Neel Haldolaarachchige, Max Hirschberger, NP Ong, et al. Large, non-saturating magnetoresistance in WTe_2. *Nature*, 514(7521):205–208, 2014.

[70] JianHua Du, HangDong Wang, Qin Chen, QianHui Mao, Rajwali Khan, BinJie Xu, YuXing Zhou, YanNan Zhang, JinHu Yang, Bin Chen, et al. Large unsaturated positive and negative magnetoresistance in Weyl semimetal TaP. *Science China Physics, Mechanics & Astronomy*, 59(5):1–6, 2016.

[71] Jürgen Nuss, Ulrich Wedig, and Martin Jansen. Geometric variations and electron localizations in intermetallics: PbFCl type compounds. *Zeitschrift für Kristallographie-Crystalline Materials*, 221(5-7):554–562, 2006.

[72] MB Schilling, LM Schoop, BV Lotsch, M Dressel, and AV Pronin. Flat optical conductivity in ZrSiS due to two-dimensional Dirac bands. *Physical Review Letters*, 119(18):187401, 2017.

[73] Mazhar N Ali, Leslie M Schoop, Chirag Garg, Judith M Lippmann, Erik Lara, Bettina Lotsch, and Stuart SP Parkin. Butterfly magnetoresistance, quasi-2D Dirac Fermi surface and topological phase transition in ZrSiS. *Science Advances*, 2(12):e1601742, 2016.

[74] Ratnadwip Singha, Arnab Kumar Pariari, Biswarup Satpati, and Prabhat Mandal. Large nonsaturating magnetoresistance and signature of nondegenerate Dirac

nodes in ZrSiS. *Proceedings of the National Academy of Sciences*, page 201618004, 2017.

[75] Yang-Yang Lv, Bin-Bin Zhang, Xiao Li, Shu-Hua Yao, YB Chen, Jian Zhou, Shan-Tao Zhang, Ming-Hui Lu, and Yan-Feng Chen. Extremely large and significantly anisotropic magnetoresistance in ZrSiS single crystals. *Applied Physics Letters*, 108(24):244101, 2016.

[76] Jin Hu, Zhijie Tang, Jinyu Liu, Yanglin Zhu, Jiang Wei, and Zhiqiang Mao. Nearly massless Dirac fermions and strong Zeeman splitting in the nodal-line semimetal ZrSiS probed by de Haas-van Alphen quantum oscillations. *Physical Review B*, 96(4):045127, 2017.

[77] S Pezzini, MR van Delft, LM Schoop, BV Lotsch, A Carrington, MI Katsnelson, NE Hussey, and S Wiedmann. Unconventional mass enhancement around the Dirac nodal loop in ZrSiS. *Nature Physics*, 14(2):178, 2018.

[78] R Matzdorf, G Meister, and A Goldmann. Influence of electron-phonon interactions on angle-resolved photoelectron spectra from metals. *Surface Science*, 296(2):241–250, 1993.

[79] AX Gray, C Papp, Shigenori Ueda, B Balke, Y Yamashita, L Plucinski, J Minár, J Braun, ER Ylvisaker, CM Schneider, et al. Probing bulk electronic structure with hard X-ray angle-resolved photoemission. *Nature Materials*, 10(10):759–764, 2011.

[80] Raman Sankar, G Peramaiyan, I Panneer Muthuselvam, Christopher J Butler, Klauss Dimitri, Madhab Neupane, G Narsinga Rao, M-T Lin, and FC Chou. Crystal growth of Dirac semimetal ZrSiS with high magnetoresistance and mobility. *Scientific reports*, 7:40603, 2017.

[81] Ph Hofmann, Ch Søndergaard, S Agergaard, SV Hoffmann, JE Gayone, G Zampieri, S Lizzit, and A Baraldi. Unexpected surface sensitivity at high energies in angle-resolved photoemission. *Physical Review B*, 66(24):245422, 2002.

[82] C Waldfried, DN McIlroy, Jiandi Zhang, PA Dowben, GA Katrich, and EW Plummer. Determination of the surface Debye temperature of Mo (112) using valence band photoemission. *Surface Science*, 363(1-3):296–302, 1996.

[83] Madhab Neupane, Ilya Belopolski, M Mofazzel Hosen, Daniel S Sanchez, Raman Sankar, Maria Szlawska, Su-Yang Xu, Klauss Dimitri, Nagendra Dhakal, Pablo Maldonado, et al. Observation of topological nodal fermion semimetal phase in ZrSiS. *Physical Review B*, 93(20):201104, 2016.

[84] Qiunan Xu, Zhida Song, Simin Nie, Hongming Weng, Zhong Fang, and Xi Dai. Two-dimensional oxide topological insulator with iron-pnictide superconductor LiFeAs structure. *Physical Review B*, 92(20):205310, 2015.

[85] see VASP manual: `www.vasp.at`.

[86] Yu A Bychkov and É I Rashba. Properties of a 2D electron gas with lifted spectral degeneracy. *JETP Letters*, 39(2):78, 1984.

[87] YX Zhao and Andreas P Schnyder. Nonsymmorphic symmetry-required band crossings in topological semimetals. *Physical Review B*, 94(19):195109, 2016.

[88] Raquel Queiroz and Andreas P Schnyder. Helical Majorana surface states of strongly disordered topological superconductors with time-reversal symmetry. *Physical Review B*, 91(1):014202, 2015.

[89] D Takane, Zhiwei Wang, S Souma, K Nakayama, CX Trang, T Sato, T Takahashi, and Yoichi Ando. Dirac-node arc in the topological line-node semimetal HfSiS. *Physical Review B*, 94(12):121108, 2016.

[90] C Chen, X Xu, J Jiang, S-C Wu, YP Qi, LX Yang, MX Wang, Y Sun, NBM Schröter, HF Yang, et al. Dirac line nodes and effect of spin-orbit coupling in the nonsymmorphic critical semimetals MSiS (M = Hf, Zr). *Physical Review B*, 95(12):125126, 2017.

[91] R Lou, J-Z Ma, Q-N Xu, B-B Fu, L-Y Kong, Y-G Shi, P Richard, H-M Weng, Z Fang, S-S Sun, et al. Emergence of topological bands on the surface of ZrSnTe crystal. *Physical Review B*, 93(24):241104, 2016.

[92] Yan Sun, Shu-Chun Wu, and Binghai Yan. Topological surface states and Fermi arcs of the noncentrosymmetric Weyl semimetals TaAs, TaP, NbAs, and NbP. *Physical Review B*, 92(11):115428, 2015.

[93] Meng Tao, Darshak Udeshi, Nasir Basit, Eduardo Maldonado, and Wiley P Kirk. Removal of dangling bonds and surface states on silicon (001) with a monolayer of selenium. *Applied Physics Letters*, 82(10):1559–1561, 2003.

[94] Shan Guan, Ying Liu, Zhi-Ming Yu, Shan-Shan Wang, Yugui Yao, and Shengyuan A Yang. Two-dimensional spin-orbit Dirac point in monolayer HfGeTe. *Physical Review Materials*, 1(5):054003, 2017.

[95] DW Lynch and JH Weaver. Photoemission of Ce and its compounds. *Handbook on the physics and chemistry of rare earths*, 10:231–300, 1987.

[96] Emanuel Knill, Raymond Laflamme, and Wojciech H Zurek. Resilient quantum computation. *Science*, 279(5349):342–345, 1998.

[97] A Yu Kitaev. Fault-tolerant quantum computation by anyons. *Annals of Physics*, 303(1):2–30, 2003.

[98] Liang Fu and Charles L Kane. Superconducting proximity effect and Majorana fermions at the surface of a topological insulator. *Physical Review Letters*, 100(9):096407, 2008.

[99] GP Mikitik and Yu V Sharlai. Manifestation of Berry's phase in metal physics. *Physical Review Letters*, 82(10):2147, 1999.

[100] Igor A Luk'yanchuk and Yakov Kopelevich. Dirac and normal fermions in graphite and graphene: Implications of the quantum Hall effect. *Physical review letters*, 97(25):256801, 2006.

[101] H Murakawa, MS Bahramy, M Tokunaga, Y Kohama, C Bell, Y Kaneko, N Nagaosa, HY Hwang, and Y Tokura. Detection of Berry's phase in a bulk Rashba semiconductor. *Science*, 342(6165):1490–1493, 2013.

[102] EM Lifshits and AM Kosevich. Theory of the Shubnikov-de Haas effect. *Journal of Physics and Chemistry of Solids*, 4(1-2):1–10, 1958.

[103] Kostya S Novoselov, Andre K Geim, SV Morozov, D Jiang, MI Katsnelson, IV Grigorieva, SV Dubonos, and AA Firsov. Two-dimensional gas of massless Dirac fermions in graphene. *Nature*, 438(7065):197, 2005.

[104] Markus König, Steffen Wiedmann, Christoph Brüne, Andreas Roth, Hartmut Buhmann, Laurens W Molenkamp, Xiao-Liang Qi, and Shou-Cheng Zhang. Quantum spin Hall insulator state in HgTe quantum wells. *Science*, 318(5851):766–770, 2007.

[105] JM Lu, O Zheliuk, Inge Leermakers, Noah FQ Yuan, Uli Zeitler, Kam Tuen Law, and JT Ye. Evidence for two-dimensional Ising superconductivity in gated MoS_2. *Science*, 350(6266):1353–1357, 2015.

[106] Yuan Cao, Valla Fatemi, Shiang Fang, Kenji Watanabe, Takashi Taniguchi, Efthimios Kaxiras, and Pablo Jarillo-Herrero. Unconventional superconductivity in magic-angle graphene superlattices. *Nature*, 556(7699):43, 2018.

[107] Ding Zhong, Kyle L Seyler, Xiayu Linpeng, Ran Cheng, Nikhil Sivadas, Bevin Huang, Emma Schmidgall, Takashi Taniguchi, Kenji Watanabe, Michael A McGuire, et al. Van der Waals engineering of ferromagnetic semiconductor heterostructures for spin and valleytronics. *Science Advances*, 3(5):e1603113, 2017.

[108] Kenneth S Burch, David Mandrus, and Je-Geun Park. Magnetism in two-dimensional van der Waals materials. *Nature*, 563(7729):47, 2018.

[109] E DiMasi, MC Aronson, JF Mansfield, B Foran, and S Lee. Chemical pressure and charge-density waves in rare-earth tritellurides. *Physical Review B*, 52(20):14516, 1995.

[110] G-H Gweon, JD Denlinger, JA Clack, JW Allen, CG Olson, E DiMasi, MC Aronson, B Foran, and S Lee. Direct observation of complete Fermi surface, imperfect nesting, and gap anisotropy in the high-temperature incommensurate charge-density-wave compound $SmTe_3$. *Physical Review Letters*, 81(4):886, 1998.

[111] V Brouet, WL Yang, XJ Zhou, Z Hussain, N Ru, KY Shin, IR Fisher, and ZX Shen. Fermi Surface Reconstruction in the CDW State of $CeTe_3$ Observed by Photoemission. *Physical Review Letters*, 93(12):126405, 2004.

[112] N Ru, RA Borzi, A Rost, AP Mackenzie, J Laverock, SB Dugdale, and IR Fisher. de Haas-van Alphen oscillations in the charge density wave compound lanthanum tritelluride $LaTe_3$. *Physical Review B*, 78(4):045123, 2008.

[113] N Ru, CL Condron, GY Margulis, KY Shin, J Laverock, SB Dugdale, MF Toney, and IR Fisher. Effect of chemical pressure on the charge density wave transition in rare-earth tritellurides RTe_3. *Physical Review B*, 77(3):035114, 2008.

[114] AA Sinchenko, PD Grigoriev, Pascal Lejay, and Pierre Monceau. Spontaneous breaking of isotropy observed in the electronic transport of rare-earth tritellurides. *Physical Review Letters*, 112(3):036601, 2014.

[115] Christos Malliakas, Simon JL Billinge, Hyun Jeong Kim, and Mercouri G Kanatzidis. Square nets of Tellurium: Rare-earth dependent variation in the charge-density wave of $RETe_3$ (RE = rare-earth element). *Journal of the American Chemical Society*, 127(18):6510–6511, 2005.

[116] HJ Kim, CD Malliakas, AT Tomić, SH Tessmer, MG Kanatzidis, and SJL Billinge. Local atomic structure and discommensurations in the charge density wave of $CeTe_3$. *Physical Review Letters*, 96(22):226401, 2006.

[117] Christos D Malliakas and Mercouri G Kanatzidis. Divergence in the Behavior of the Charge Density Wave in $RETe_3$ (RE = Rare-Earth Element) with Temperature and RE Element. *Journal of the American Chemical Society*, 128(39):12612–12613, 2006.

[118] Yuji Iyeiri, Teppei Okumura, Chishiro Michioka, and Kazuya Suzuki. Magnetic properties of rare-earth metal tritellurides RTe_3 (R = Ce, Pr, Nd, Gd, Dy). *Physical Review B*, 67(14):144417, 2003.

[119] N Ru, J-H Chu, and IR Fisher. Magnetic properties of the charge density wave compounds RTe_3 (R = Y, La, Ce, Pr, Nd, Sm, Gd, Tb, Dy, Ho, Er, and Tm). *Physical Review B*, 78(1):012410, 2008.

[120] JJ Hamlin, DA Zocco, TA Sayles, MB Maple, J-H Chu, and IR Fisher. Pressure-induced superconducting phase in the charge-density-wave compound terbium tritelluride. *Physical Review Letters*, 102(17):177002, 2009.

[121] DA Zocco, JJ Hamlin, K Grube, J-H Chu, H-H Kuo, IR Fisher, and MB Maple. Pressure dependence of the charge-density-wave and superconducting states in $GdTe_3$, $TbTe_3$, and $DyTe_3$. *Physical Review B*, 91(20):205114, 2015.

[122] Veronique Brouet, WL Yang, XJ Zhou, Zahid Hussain, RG Moore, R He, DH Lu, ZX Shen, J Laverock, SB Dugdale, et al. Angle-resolved photoemission study of the evolution of band structure and charge density wave properties in RTe_3 (R = Y, La, Ce, Sm, Gd, Tb, and Dy). *Physical Review B*, 77(23):235104, 2008.

[123] Isabella Gierz, Christian Riedl, Ulrich Starke, Christian R. Ast, and Klaus Kern. Atomic Hole Doping of Graphene. *Nano Letters*, 8(12):4603–4607, December 2008.

[124] Zhiliang Wang and Lianzhou Wang. Photoelectrode for water splitting: Materials, fabrication and characterization. *Science China Materials*, pages 1–16, 2018.

[125] Alessio Filippetti, A Mattoni, Claudia Caddeo, MI Saba, and P Delugas. Low electron-polar optical phonon scattering as a fundamental aspect of carrier mobility in methylammonium lead halide $CH_3NH_3PbI_3$ perovskites. *Physical Chemistry Chemical Physics*, 18(22):15352–15362, 2016.

[126] Andreas Hofmann and Christian Pettenkofer. Electronic band structure of epitaxial $CuInSe_2$ films. *Physical Review B*, 84(11):115109, 2011.

[127] Stefan Muff, Mauro Fanciulli, Andrew P Weber, Nicolas Pilet, Zoran Ristić, Zhiming Wang, Nicholas C Plumb, Milan Radović, and J Hugo Dil. Observation of a two-dimensional electron gas at $CaTiO_3$ film surfaces. *Applied Surface Science*, 432:41–45, 2018.

[128] Jayita Nayak, Kai Filsinger, Gerhard H Fecher, Stanislav Chadov, Ján Minár, Emile DL Rienks, Bernd Büchner, Stuart P Parkin, Jörg Fink, and Claudia Felser. Observation of a remarkable reduction of correlation effects in $BaCr_2As_2$ by ARPES. *Proceedings of the National Academy of Sciences*, 114(47):12425–12429, 2017.

[129] Jessica J Frick, Satya K Kushwaha, Robert J Cava, and Andrew B Bocarsly. Characterization of Primary Carrier Transport Properties of the Light-Harvesting Chalcopyrite Semiconductors CuIn $(S_{1-x}Se_x)_2$. *The Journal of Physical Chemistry C*, 121(32):17046–17052, 2017.

[130] Qingfeng Dong, Yanjun Fang, Yuchuan Shao, Padhraic Mulligan, Jie Qiu, Lei Cao, and Jinsong Huang. Electron-hole diffusion lengths > 175 μm in solution grown $CH_3NH_3PbI_3$ single crystals. *Science*, page aaa5760, 2015.

[131] Alexander JE Rettie, Heung Chan Lee, Luke G Marshall, Jung-Fu Lin, Cigdem Capan, Jeffrey Lindemuth, John S McCloy, Jianshi Zhou, Allen J Bard, and C Buddie Mullins. Combined charge carrier transport and photoelectrochemical characterization of $BiVO_4$ single crystals: intrinsic behavior of a complex metal oxide. *Journal of the American Chemical Society*, 135(30):11389–11396, 2013.

[132] Fan Zheng, Liang Z Tan, Shi Liu, and Andrew M Rappe. Rashba spin-orbit coupling enhanced carrier lifetime in $CH_3NH_3PbI_3$. *Nano letters*, 15(12):7794–7800, 2015.

[133] Thibaud Etienne, Edoardo Mosconi, and Filippo De Angelis. Dynamical origin of the rashba effect in organohalide lead perovskites: A key to suppressed carrier recombination in perovskite solar cells? *The Journal of Physical Chemistry Letters*, 7(9):1638–1645, 2016.

[134] Pooya Azarhoosh, Scott McKechnie, Jarvist M Frost, Aron Walsh, and Mark Van Schilfgaarde. Research Update: Relativistic origin of slow electron-hole recombination in hybrid halide perovskite solar cells. *APL Materials*, 4(9):091501, 2016.

[135] Mikaël Kepenekian, Roberto Robles, Claudine Katan, Daniel Sapori, Laurent Pedesseau, and Jacky Even. Rashba and Dresselhaus effects in hybrid organic-inorganic perovskites: From basics to devices. *ACS nano*, 9(12):11557–11567, 2015.

[136] Andrzej Lasia. *Electrochemical impedance spectroscopy and its applications*, volume 7. Springer, 2014.

[137] Gokul V Govindaraju, Garrett P Wheeler, Dongho Lee, and Kyoung-Shin Choi. Methods for electrochemical synthesis and photoelectrochemical characterization for photoelectrodes. *Chemistry of Materials*, 29(1):355–370, 2016.

Acknowledgments

This thesis would not have been possible without the help and cooperation of many people. Although, it will not be possible to name every last one of them here, I would like to take the opportunity to give my thanks to a few in particular:

Dr. habil. Christian Ast and **Asst. Prof. Leslie Schoop** for giving me the opportunity to work with them here at the Max Planck Institute in Stuttgart. Not only did they teach me what it means to be a scientist and facilitate collaborations, they also did it with such passion that finding motivation was never an issue. I am especially thankful to Christian for his ARPES expertise and the atmosphere I could be part of in his group, and to Leslie for her vision and the wonderful time in Princeton.

Prof. Klaus Kern and **Prof. Bettina Lotsch** for sharing me in both their departments and providing me with everything I could ever need for my scientific research. The work in their respective groups made me aware of the privileged conditions we are subject to at the Max Planck Institute for Solid State Research. It is here, where I have to thank **Sabine Birtel** and **Sigrid Fuhrmann** as well. Without their help in the jungle of bureaucracy at the institute, I would have surely been lost.

Dr. Lukas Müchler, **Dr. Raquel Queiroz**, **Dr. Maia Vergniory** and **Prof. Andreas Grüneis** for the insightful discussions about DFT, tight-binding, symmetry elements and topology, but also for the recreational evenings. It was their theoretical know-how that allowed us to determine the origin of the surface states we observed in ARPES.

Juan Chamorro, **Dr. Shiming Lei** and **Jessica Frick** for the opportunity to answer some electronic structure questions concerning their materials, which was $LaCuSb_2$, $GdTe_3$ and $CuInTe_2$, respectively. It was a lot of fun extending my knowledge beyond the ZrSiS-family.

Maxim Krivenkov, **Dr. Dmitry Marchenko** and **Dr. Andrei Varykhalov** from my Bessy II beamtimes and **Dr. Jessica McChesney** and **Dr. Fanny Rodolakis** from my APS beamtimes. It was every time a lot of fun taking a vacation from everything and only having to worry about measuring for a week. Without their help, the papers originating from this Ph.D. work would not have been possible and I would have probably fallen asleep a long time ago.

Wolfgang Stiepany, **Peter Andler** and **Marco Memmler** for their technical support. They were always able to devise a way for my conceptions to actually work out.

Dr. Hadj Benia and the **Ulrich Starke** group for their introduction to the 7B15 lab and the nice atmosphere they kept there.

Dr. Carola Straßer, my predecessor, for the knowledge she was able to pass on in such a short time. Although I never warmed up to Igor, I am thankful for the rudimentary knowledge I was able to acquire in this period, so I could analyze the data until I could implement everything in Matlab.

My colleagues from the MPI, that not only enriched the lunch and coffee breaks, but were also responsible for some legendary evenings at Ringberg, **Dr. Kelvin Anggara**, **Dr. Manish Garg**, **Abishek Grewal**, **Dr. Rico Gutzler**, **Dr. Bastian Kern**, **Lukas Krumbein**, **Dr. Christopher Leon**, **Shai Mangel**, **Dr. Soudabeh Mashhadi Sheikholharam**, **Tomasz Michnowicz**, **Hannah Ochner**, **Anna Roslowska**, **Alessio Scavuzzo** and **Sven Szilagyi**. My special thanks goes to **Shweta Sheoran** for allowing me to experience what it means to be a supervisor and **Dr. Douglas Fabini** and **Dr. Srinivasa Rao Lingampalli**, who come up with so many new ideas for projects that I almost feel sad my Ph.D. is already over.

Dr. Robert Drost, **Haonan Huang**, **Jason Peng**, **Dr. Jacob Senkpiel**, **Janis Siebrecht** and **Maximilian Uhl** for sharing the experience of a weekly Monday morning meeting. I could not have wished for a nicer subgroup.

My office mates **Patrick Alexa**, **Piotr Kot** and **Katharina Polyudov**. Not only did we discuss scientific problems but equally as often philosophical topics. I will never forget the Ping Pong breaks and the 2/3 of the Lord of the Rings.

Dr. Kai Filsinger and the **Schoop** group. They made my stay in Princeton unforgettable and I hope I will find the time to visit them again soon.

Dr. Sabine Abb and **Dr. Diana Hötger** for the sushi evenings we shared and their tireless attempts to teach me how to cook.

My **friends** for showing me the bigger picture outside of the utopian research-driven world. They made sure I did not loose myself and had the social basis in times of need. I would like to express my deepest gratitude to **Heiko Hütter**, **Oliver Naumann** and **Annegret Widmer**. Our pen-and-paper role-playing games, our philosophical recreational evenings and your advice made me a better person.

Last, but not least, I want to thank my parents **Horst** and **Sigrun Topp**, my brother **Thomas Topp**, my grandparents **Hermann** and **Rosa Queißner**, and **Gene Roddenberry**, who all had a formative influence on my life and always encouraged my love for physics. For everything you did to support me on my way and your never ending love, I can not thank you enough.